

BremHLR

Kompetenzzentrum für Höchstleistungsrechnen Bremen

Statusbericht 2022
des
Kompetenzzentrums
für
Höchstleistungsrechnen Bremen
–BremHLR–

Bremen, Juli 2023



Universität
Bremen



ALFRED-WEGENER-INSTITUT
HELMHOLTZ-ZENTRUM FÜR POLAR-
UND MEERESFORSCHUNG



HSB

Hochschule
Bremerhaven



Norddeutscher Verbund für Hoch- und Höchstleistungsrechnen

© 2003-2023 BremHLR – Kompetenzzentrum für Höchstleistungsrechnen Bremen

www.bremhlr.uni-bremen.de

Das Berichtsjahr 2022 in Stichpunkten

- Stabiler Betrieb des HLRN 4 im Endausbau
- Übergang der HLRN-Systeme in das Nationale Hochleistungsrechnen (NHR-Verbund)
- Weiter ansteigende Bremer Nutzung der Ressourcen des Norddeutschen Verbunds für Hoch- und Höchstleistungsrechnen (HLRN)

Inhaltsverzeichnis

1	BremHLR: Aufgaben und organisatorische Struktur	5
1.1	Aufgaben.....	5
1.2	Struktur.....	5
2	Tätigkeitsprofil des BremHLR im Berichtszeitraum.....	6
2.1	Unterstützung der HLRN-Nutzung im Land Bremen.....	6
2.2	Weitere Aktivitäten des BremHLR	6
3	Statistische Angaben zu den Bremer Höchstleistungsprojekten	6
4	Veranstaltungen mit Beteiligung des BremHLR	8
5	Weiterentwicklung des HLRN: Übergang zum nationalen Hochleistungsrechnen (NHR).....	10
6	Projektberichte	12
6.1	<i>hbb00001-3 and hbi000057: Biomolecular modeling (at interfaces) within the HMI group..</i>	12
6.2	<i>hbc00045: Rupturing materials in electric fields</i>	16
6.3	<i>hbc00056: Towards an atomic-level understanding of the interaction of probe molecules with acid sites in zeolites</i>	19
6.4	<i>hbc00057: Towards a molecular description of the conformational ensemble of miRNA.....</i>	23
6.5	<i>hbc00060: Creating a two-dimensional electron gas in a bulk crystal.....</i>	26
6.6	<i>hbc00061: Studying the Wet and Dry CO Oxidation on Nanoporous Gold Using Static DFT Computations and AIMD Simulations.....</i>	29
6.7	<i>hbc00062: Adsorption of pharmaceuticals and personal care products in zeolites studied with density functional theory calculations.....</i>	33
6.8	<i>hbi00036: Fluid Dynamics Investigation of the Stress Loading of Protein–Stabilized o/w– Interfaces in Premix Membrane Emulsification.....</i>	37
6.9	<i>hbi00037: Molekulardynamische Untersuchung der Stressbeanspruchungen auf Proteine an der Phasengrenzfläche beim Premix-Membranemulgieren</i>	41
6.10	<i>hbi00042: Drag reduction by air retaining surfaces – Long holes</i>	45
6.11	<i>hbi00053: Turbulent puff dynamics in pulsatile pipe flow.....</i>	49
6.12	<i>hbi00055: Validation and parametrisation of turbulence and transport models used in computational fluid dynamic studies of aerosol transport in indoor environments.....</i>	52
6.13	<i>hbi00056: Pipes - gliding on air? Turbulent pipe flow – drag reduction by superhydrophobic surfaces</i>	56
6.14	<i>hbk00059: Joint state-parameter estimation for the Last Glacial Maximum with CESM1.2 .</i>	60
6.15	<i>hbk00062: Retrieval of stratospheric ozone profiles from OMPS observations in limb geometry and long term trends.....</i>	64

6.16 <i>hbk00071</i> : Development of an Earth system model coupled with a sediment diagenesis model toward long-term paleoclimate simulations	67
6.17 <i>hbk00075</i> : Assessing the effect of environmental and biological conditions on Antarctic krill large-scale connectivity facilitated by ocean currents.....	71
6.18 <i>hbk00079</i> : Tipping points in Antarctic Bottom Water formation and Southern Ocean carbon sequestration.....	75
6.19 <i>hbk00083</i> : Tipping points in the ecosystem of the ‘new Arctic’ Ocean	79
6.20 <i>hbk00084</i> : Marine biogenic aerosol precursors in the Arctic Ocean	83
6.21 <i>hbk00085</i> : Modellierung des Einsetzens der letzten Eiszeit	86
6.22 <i>hbk00087</i> : Arctic Amplification in the Barents Sea: Evaluation of an Ice-Ocean-Atmosphere Feedback in a Coupled Climate Model	89
6.23 <i>hbk00090</i> : Paleoclimate Applications of Mixing Parameterizations in an Earth System Model	92
6.24 <i>hbk00094</i> : The effects of Ocean Alkalinity Enhancement on the anthropogenic CO ₂ concentrations in the 21 st century.....	96
6.25 <i>hbk00095</i> : Application of ensemble data assimilation for improved prediction of ocean ecosystem indicators	100
6.26 <i>hbp00041</i> : Multi-Messenger Signals from Compact Objects.....	103
6.27 <i>hbp00058</i> : Exploring the mechanistic process of vitamin B ₁₂ acquisition by human gut bacteria	107
6.28 <i>hbp00067</i> : Carrier Multiplication in Monolayer Transition Metal Dichalcogenides	111
6.29 <i>hbp00068</i> : Enhanced sampling methods for constructing free energy surfaces of antibiotic permeation through porins	115
6.30 <i>hbp00072</i> : Ozone Profile Retrieval from TROPOMI measurements in the UV spectral range	119
6.31 <i>nak0001</i> : Seamless sea ice prediction with AWI Climate Model	123

1 BremHLR: Aufgaben und organisatorische Struktur

1.1 Aufgaben

Das Land Bremen beteiligt sich am Norddeutschen Verbund für Hoch- und Höchstleistungsrechnen – HLRN – um an dem rasanten Fortschritt der Computer- und Softwaretechnologie Teil zu haben. Das Kompetenzzentrum für Höchstleistungsrechnen Bremen – BremHLR – unterstützt dazu Wissenschaftler im wissenschaftlichen Rechnen insbesondere im Land Bremen. Die Fachberater des BremHLR leisten Unterstützung für Projekte sowohl in der Konzeption, der Antragstellung als auch der Durchführung. Der Schwerpunkt der Unterstützung liegt hierbei auf Projekten auf dem HLRN-System. Seit 2005 wurde die Betreuung aber auch auf Rechenprojekte an den nationalen Höchstleistungsrechenzentren wie z. B. dem Jülich Supercomputing Centre (JSC) ausgeweitet.

Als Bestandteil im Kompetenznetzwerk des HLRN beteiligt sich BremHLR unter anderem an der fachspezifischen Nutzerberatung, der Pflege von Software-Paketen und der Veranstaltung überregionaler Nutzerworkshops. Die Geschäftsstelle des BremHLR ist an der Universität Bremen im Zentrum für Technomathematik angesiedelt.

Das BremHLR wurde am 1. Juli 2003 als Kooperation zwischen der Universität Bremen (UB), der Jacobs University Bremen (JUB) und dem Alfred-Wegener-Institut Helmholtz-Zentrum für Polar- und Meeresforschung (AWI) gegründet. Seit April 2008 ist die Hochschule Bremerhaven (HBHV) und seit Juli 2021 die Hochschule Bremen (HSHB) Kooperationspartner des BremHLR. Das Kompetenzzentrum wird von den beteiligten Kooperationspartnern sowie der Bremer Senatorin für Wissenschaft und Häfen (SWH) anteilig finanziell getragen. Seit Januar 2014 ist die JUB als ideales Mitglied beitragsfrei gestellt. Im Jahr 2021 konnte eine Weiterfinanzierung des BremHLR bis Ende 2024 sichergestellt werden.

1.2 Struktur

Dem Lenkungsausschuss des BremHLR als oberstes beschlussfassendes und steuerndes Gremium gehörten in der Berichtsperiode folgende Vertreter der kooperierenden Einrichtungen an. Im Einzelnen sind dies:

- Prof. Dr. Alfred Schmidt (UB/Zentrum für Technomathematik ZeTeM)
- Prof. Dr. Stephan Frickenhaus (AWI/Rechenzentrum, UB/FB3)
- Prof. Dr. Ulrich Kleinekathöfer (JUB)
- Prof. Dr. Henrik Lipskoch (HBHV)
- Prof. Dr. A. Baars (HSHB)
- Dr. Jörg Hofmann (SWH)

Die fachspezifische Betreuung der Projekte am Norddeutschen Verbund für Hoch- und Höchstleistungsrechnen (HLRN) sowie von Projekten an anderen nationalen Höchstleistungsrechenzentren wird von den Fachberatern des BremHLR geleistet, die ebenfalls den Einrichtungen der Kooperationspartner angehören. Im Berichtszeitraum waren folgende Fachberater tätig:

- Dr. Lars Nerger (AWI/Rechenzentrum, UB/ZeTeM, Leiter Geschäftsstelle)
- Thorsten Coordes (UB/ZARM)
- Dr. Achim Geleßus (JUB/CLAMV)
- Dr. Natalja Rakowsky (AWI/Rechenzentrum, bis September 2022)
- Dr. Sebastian Hinck (AWI/Rechenzentrum, seit Oktober 2022)

Die Geschäftsstelle ist verantwortlich für die Organisation der Workshops (siehe Abschnitt Veranstaltungen) und die Unterstützung der Nutzer, insbesondere im Antragsverfahren. Im April 2022 konnte das Sekretariat der Geschäftsstelle wieder dauerhaft besetzt werden mit Katharina Müller.

2 Tätigkeitsprofil des BremHLR im Berichtszeitraum

2.1 Unterstützung der HLRN-Nutzung im Land Bremen

Ein Schwerpunkt der Aktivitäten des BremHLR lag auch in diesem Berichtszeitraum in der Unterstützung der HLRN-Nutzung. Neben den Tätigkeiten von Prof. Dr. Stephan Frickenhaus als Mitglied der Technischen Kommission sowie Prof. Dr. Alfred Schmidt als Mitglied des Wissenschaftlichen Ausschusses bestand die Unterstützung des HLRN durch das BremHLR hauptsächlich in der Fachberatung für Bremer Projekte am HLRN von der Antragstellung bis zur Begleitung rechenintensiver Projekte während der gesamten Projektlaufzeit.

Eine wesentliche Aufgabe im Berichtsjahr war die weitere Unterstützung der Bremer Nutzer des HLRN bei der effizienten Nutzung der HLRN-Hochleistungsrechner-Systeme. Hierbei war ein Fokus den stabilen Fortschritt der Projekte zu unterstützen.

2.2 Weitere Aktivitäten des BremHLR

Nach zweijähriger Pause bedingt durch die Covid-19 Pandemie konnte im Jahr 2022 wieder der Workshop zur Einführung in die parallele Programmierung stattfinden. Mit 12 Teilnehmern war dieser Workshop wieder gut besucht.

Der Workshop wurde in der Zeit vom 19. bis 23. September 2023 an der Universität Bremen abgehalten. Als Referent konnte wie bereits bei bisherigen Workshops Dr. Hinnerk Stüben vom Regionalen Rechenzentrum der Universität Hamburg gewonnen werden, der den Workshop gemeinsam mit dem BremHLR-Fachberater Dr. Lars Nerger leitete.

Der sehr gute Zuspruch und der große Erfolg der Veranstaltungen zeigt deutlich den dringenden Bedarf zur Ausbildung im Hoch- und Höchstleistungsrechnen und gibt Anlass dazu solche Workshops auch weiterhin als regelmäßige Ausbildungs- und Schulungs-Maßnahme anzubieten.

Die Fachberater des BremHLR beteiligten sich an dem Fachberaterworkshop des HLRN-Kompetenznetzwerks der im Jahr 2022 wieder in Präsenz stattfinden konnte. Bei dem Workshop wurden unterschiedliche Themen des HLRN-Betriebs und der Nutzerbetreuung besprochen. Eine Übersicht über die Veranstaltungen ist in Abschnitt 4 zu finden.

Im Auftrag der Kanzlerin und des Konrektors der Uni Bremen starteten Stephan Frickenhaus und Torsten Coordes mit der Entwicklung eines Konzepts für einen nachhaltig betreibbaren und synergiestiftenden HPC-Cluster an der Uni-Bremen.

3 Statistische Angaben zu den Bremer Höchstleistungsprojekten

Auch im Jahr 2022 wurden die HLRN-Rechner intensiv durch Bremer Projekte genutzt. Über das Jahr wurde auf den HLRN-Systemen ein prozentualer Anteil von 8,7% an der gesamten genutzten Rechenleistung des HLRN erreicht. Dieses liegt deutlich über dem Finanzierungsanteil von etwa 7,87% des Landes Bremen am HLRN. Über die gesamte

Laufzeit der HLRN-IV Systeme wurde durch Bremer Projekte ein Anteil von 8,6% der verfügbaren Rechenzeit abgenommen.

Der stabile Betrieb der HLRN-IV Systeme ermöglicht eine stabile Nutzung. Diese zeichnet sich durch eine hohe Nutzung von ca. 31 Mio. core-h pro Quartal aus. Hiervon weicht nur das dritte Quartal, vermutlich bedingt durch die Sommerferien, ab. Insgesamt wurden im Jahr 2022 etwa 119,8 Mio. core-h¹ durch Bremer Projekte am HLRN abgenommen.

Abbildung 3.1 zeigt die quartalsweise Nutzung des HLRN durch die Bremer Projekte. Während der Umbauphase Ende 2019 und Anfang 2020 wurde die Nutzung nur unvollständig erfasst.

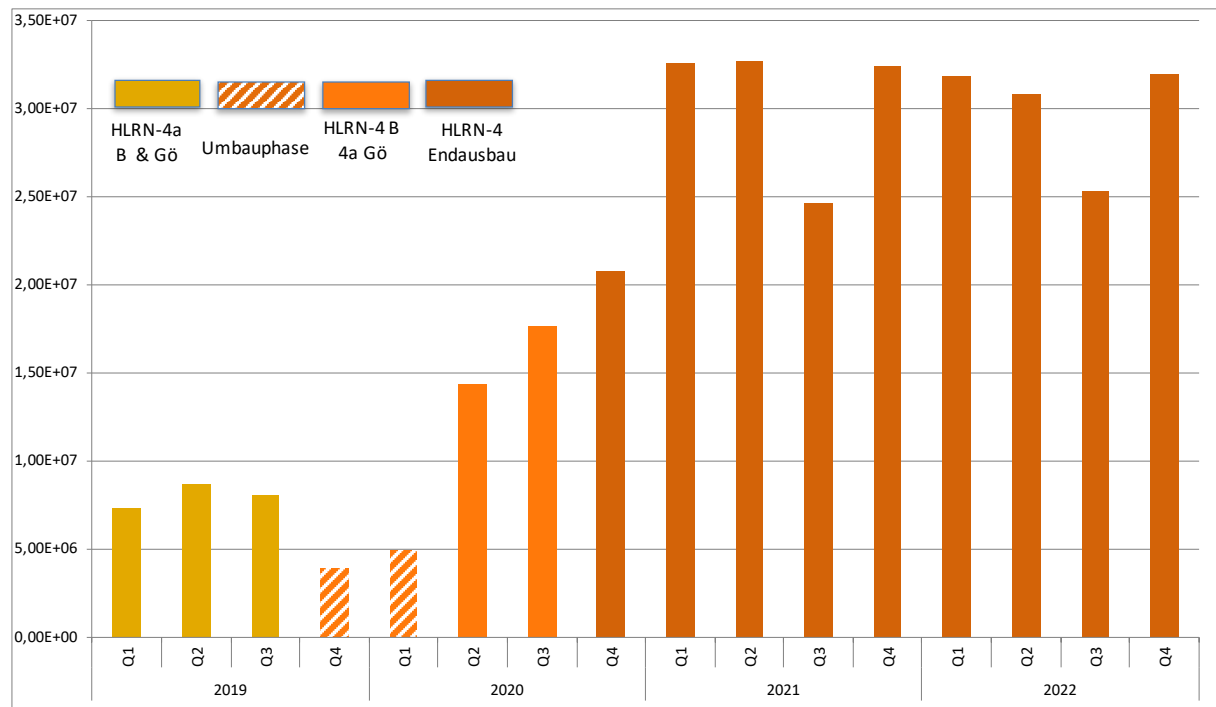


Abbildung 3.1: Quartalsweise Rechenzeitnutzung der Bremer HLRN-Großprojekte auf den HLRN-IV Systemen in der Einheit Prozessor-Stunden (core-h). Die Farben zeigen die Verfügbarkeit der unterschiedlichen Ausbaustufen des HLRN-Systems. Im vierten Quartal 2019 war der Betrieb durch die Umbaumaßnahmen beeinträchtigt und weitgehend nur das HLRN-IV System in Göttingen verfügbar. Im ersten Quartal 2020 waren die Nutzer vielfach mit Portierungsarbeiten befasst. Seit dem vierten Quartal 2020 befindet sich das HLRN-IV System im Endausbau.

Eine Übersicht zu allen vom BremHLR betreuten Projekten geben die Tabellen 3.1 und 3.2. Im Jahr 2022 wurden vom BremHLR 50 Projekte am HLRN betreut. 12 neue Projekte mit teilweise sehr großem Rechenzeitbedarf wurden im Jahr 2022 beantragt und vom Wissenschaftlichen Ausschuss des HLRN bewilligt. 18 Projekte wurden im Berichtsjahr beendet.

¹Seit dem vierten Quartal 2022 wird die Rechenleistung am HLRN in Prozessorkern-Stunden erfasst. Die Werte der früheren Quartale, die noch in der Norddeutschen Parallelrechner-Leistungseinheit erfasst wurden, wurden entsprechend dem Faktor $96/14=6,857$ umgerechnet.

4 Veranstaltungen mit Beteiligung des BremHLR

41. HLRN-Fachberater-Workshop

Veranstalter: GWDG

Datum: 3. Juni 2021

Ort: Göttingen

Teilnehmerzahl: 22

Teilnehmende Institutionen: BremHLR (AWI), GWDG/Uni Göttingen, IOW, MWK Niedersachsen, TU Hamburg, Uni Hamburg, Uni Kiel, Uni Potsdam, ZIB

15. BremHLR-Workshop *Einführung in die Programmierung mit MPI und OpenMP*

Veranstalter: BremHLR

Datum: 19. – 23. September 2022

Ort: Universität Bremen

Beschreibung: In dem Workshop wurden die Grundlagen der parallelen Programmierung vermittelt. Der Schwerpunkt lag auf den Programmiermodellen MPI und OpenMP. Praktische Übungen bildeten einen wesentlichen Teil des Workshops.

Referenten: Dr. Hinnerk Stüben (Regionales Rechenzentrum der Universität Hamburg) und Dr. Lars Nerger (BremHLR).

Teilnehmerzahl: 12

Teilnehmende Institutionen: AWI, Uni Bremen, RZ Uni Hamburg

Tabelle 3.1: Übersicht neu begonnener Bremer HPC-Projekte, die innerhalb des Berichtszeitraums vom BremHLR betreut wurden. Status: E = Erstantrag, X = Projektende in 2022; kcore-h: Kontingent im Jahr 2022 in tausend core-h.

Kennung	Projektleiter	Institut	Laufzeit	kcore-h	Status
hbb00002	Dr. S. Köppen	UB/BCCMS	III/22 – II/23	2744	E
hbb00003	Dr. S. Köppen	UB/BCCMS	IV/22 – III/23	625	E
hbc00062	Dr. M. Fischer	UB/Geo	I/22 – IV/22	2663	E
hbi00055	Dr. D. Feldmann	UB/ZARM	II/22 – I/23	4700	E
hbi00056	Prof. Dr. A. Baars	HSB	II/22 – I/23	6430	E
hbi00057	Dr. S. Köppen	UB/BCCMS	III/22 – II/23	1372	E
hbi00059	Prof. Dr. L. Colombi Ciacchi	UB/BCCMS	IV/22 – III/23	2250	E
hbk00090	Prof. Dr. M. Schulz	UB/MARUM	III/22 – II/23	5488	E
hbk00094	Prof. Dr. B. Rost	AWI & UB	III/22 – II/23	6722	E
hbk00095	Dr. L. Nerger	AWI	III/22 – III/23	6724	E
hbk00096	Prof. Dr. M. Schulz	UB/MARUM	IV/22 – III/23	1152	E
hbp00072	Dr. A. Rozanov	UB/IUP	I/22 – I/23	2881	E

Tabelle 3.2: Von BremHLR betreute fortgeführte Bremer HPC-Projekte. Status: F = Fortsetzung, X = Projektende in 2022; kcore-h: Kontingent im Jahr 2022 in tausend core-h.

Kennung	Projektleiter	Institut	Laufzeit	kcore-h	Status
hbb00001	Prof. Dr. L. Colombi Ciacchi	UB/BCCMS	III/20 – III/23	3789	F
hbc00045	Prof. Dr. T Neudecker	UB/Chemie	II/20 – III/23	3495	F
hbc00049	Dr. P. Guo	UB/BCCMS	I/21 – I/23	1381	F
hbc00051	Dr. Q. Duy Ho	UB/ZARM	I/21 – I/22	549	X
hbc00053	Prof. Dr. L. Colombi Ciacchi	UB/BCCMS	II/21 – II/22	1029	X
hbc00056	Dr. M. Fischer	UB/Geo	III/21 – III/23	1510	F
hbc00057	Dr. M. Delle Piane	UB/BCCMS	III/21 – II/22	2376	F
hbc00060	Dr. B. Aradi	UB/BCCMS	IV/21 – III/22	823	X
hbc00061	Dr. L. Moskaleva	UB/Chemie	IV/21 – III/22	3959	F
hbi00036	Prof. Dr. U. Fritsching	UB/FB4	II/17 – I/22	1338	F
hbi00037	Prof. Dr. U. Fritsching	UB/FB4	II/17 – I/22	1223	F
hbi00042	Prof. Dr. A. Baars	HS Bremen	IV/19 – III/22	11834	FX
hbi00045	Prof. Dr. C. Büskens	UB/ZeTeM	III/20 – II/22	96	FX
hbi00049	Prof. Dr. U. Fritsching	UB/IWT	IV/20 – I/22	1	FX
hbi00050	PD Dr. Y. Jin	UB/ZARM	I/21 – I/22	167	X
hbi00051	Prof Dr. R. Groll	UB/ZARM	III/21 – II/22	2634	X
hbi00053	Prof. Dr. M. Avila	UB/ZARM	IV/21 – III/22	2689	X
hbk00034	Prof. Dr. T.Kanzow	AWI & UB	III/13 – I/22	1	FX
hbk00059	Prof. Dr. M. Schulz	UB/MARUM	III/17 – III/23	11566	F
hbk00062	Dr. A. Rozanov	UB/IUP	IV/17 – III/23	4373	F
hbk00071	Prof. Dr. M. Schulz	UB/MARUM	I/19 – IV/22	17150	FX
hbk00075	Prof. Dr. D. Wolf-Gladrow	AWI & UB	IV/19 – IV/22	9261	FX
hbk00079	Prof. Dr. B. Rost	AWI & UB	II/20 – IV/22	4164	FX
hbk00080	Prof. Dr. M. Schulz	UB/MARUM	III/20 – I/22	2223	FX
hbk00083	Prof. Dr. B. Rost	AWI & UB	II/21 – III/23	11217	E
hbk00084	Prof Dr. A. Bracher	AWI & UB	IV/21 – III/23	4802	E
hbk00085	Prof. Dr. M. Schulz	UB/MARUM	IV/21 – I/23	13905	E
hbk00087	Prof. Dr. T. Kanzow	AWI & UB	IV/21 – III/22	14014	EX
hbp00041	Prof. Dr. C. Lämmerzahl, Prof. Dr. S. Rosswog	UB/ZARM	I/17 – I/23	1874	F
hbp00058	Prof. Dr. U. Kleinekathöfer	Jacobs U	II/20 – II/23	3032	F
hbp00067	Prof. Dr. T. Frauenheim	UB/BCCMS	IV/20 – III/23	3424	F
hbp00068	Prof. Dr. U. Kleinekathöfer	Jacobs U	IV/20 – IV/23	7603	F
hbp00070	Prof. Dr. T. Wehling	UB/Physik	II/21 – I/22	1029	EX
nak00001	Dr. H. Gößling	AWI	II/19 – II/22	2545	FX

5 Weiterentwicklung des HLRN: Übergang zum nationalen Hochleistungsrechnen (NHR)

Der Norddeutsche Verbund für Hoch- und Höchstleistungsrechnen (HLRN) wurde im Jahr 2001 als Verbund der sieben Bundesländer Berlin, Brandenburg, Bremen, Hamburg, Mecklenburg-Vorpommern, Niedersachsen und Schleswig-Holstein gegründet. Im Jahr 2012 ist noch das Land Brandenburg dem Verbund beigetreten. Im Rahmen des HLRN-Verbunds wurden seit dem Jahr 2002 an zwei Standorten Rechnersysteme betrieben und der Wissenschaftlichen Community der beteiligten Bundesländer diese Rechenleistung als sog. Tier-2 Systeme zur Verfügung gestellt.

In den letzten Jahren gab es eine Initiative auf Bundesebene um die Tier-2 Ebene des Hochleistungsrechnens neu zu strukturieren. Im Rahmen dieser Initiative wurde im August 2021 der NHR-Verbund (Verein für Nationales Hochleistungsrechnen – NHR-Verein e.V.) gegründet. Mitglieder des NHR-Vereins sind folgende neun Hochleistungsrechenzentren, unter anderem die beiden HLRN-Betreiberzentren:

- IT Center, RWTH Aachen
- Hochschulrechenzentrum, Technische Universität Darmstadt
- Zentrum für Nationales Hochleistungsrechnen Erlangen, Friedrich-Alexander-Universität Erlangen-Nürnberg
- GWDG, Universität Göttingen (HLRN-Standort)
- Steinbuch Centre for Computing (SCC), Karlsruher Institut für Technologie
- Zentrum für Informationsdienste und Hochleistungsrechnen, Technische Universität Dresden
- Zuse-Institut Berlin, Berlin University Alliance (HLRN-Standort)
- Paderborn Center für Parallel Computing, Universität Paderborn
- NHR Süd-West, Goethe-Universität Frankfurt, Technische Universität Kaiserslautern, Johannes Gutenberg-Universität Mainz, Universität des Saarlandes

Im Jahr 2022 wurde die eigentliche Strukturierung dieser neun Rechenzentren unter dem Dach des NHR-Verbunds umgesetzt. Während Nutzer weiterhin das Rechenzentrum für ihren jeweiligen Projektantrag auswählen wurden unter anderem die Antragsfristen vereinheitlicht. Außerdem wurden Prozesse geschaffen, um besonders große Projektanträge zentral zu begutachten. Ferner ist der Einsatz eines einheitlichen Online-Portals für die Antragstellung in Vorbereitung. Die beiden Betreiberzentren des HLRN agieren jetzt stärker unabhängig als NHR@ZIB und NHR@Göttingen.

Durch die Umstrukturierung kommt es auch zu Änderungen beim HLRN. Z.B. ist im Jahr 2022 der bisherige Wissenschaftliche Ausschuss zurückgetreten und es wurde ein Ausschuss mit neuen Mitgliedern berufen. Dieser Ausschuss wird weiterhin die Projektanträge für die beiden HLRN-Zentren begutachten. Auch die Rolle des HLRN-Verwaltungsrats sowie der Technischen Kommission des HLRN wird sich ändern. Diese Änderungen sind noch in der Entwicklung.

Die Fachberatung für die Nutzer der HLRN-Systeme wird weiterhin im Rahmen des Kompetenzzentrumsverbunds des HLRN organisiert und in Bremen betreut weiterhin das BremHLR die Nutzer.

Die Technische Kommission begann mit Strategieentwicklung für den Übergang in den NHR. Sowohl das Fachberater-Netzwerk als auch die Technische Kommission sollten als erfolgreich arbeitende Einrichtungen der sieben Länder weiterhin zusammenarbeiten und eine Perspektive über die erste NHR-Phase hinaus entwickeln. Dabei wird angestrebt, die Zentren mit Federführung in Anwendungsdisziplinen, z.B. KIT für Erdsystemwissenschaften, zur

Gründung von NHR-weiten Kompetenz-Clustern unter Mitwirkung von HPC-Ländernetzwerken und Fachberatern mit und ohne TIER-3-Anbindung einzubeziehen. Die Technische Kommission kann sich zu einem mit den Zentren Göttingen und Berlin technisch-strategisch beratenden Kreis weiterentwickeln, wobei weiterhin die leitenden IT-Experten von TIER-3-Einrichtungen zu den Mitgliedern zählen würden.

6 Projektberichte²

6.1 *hbb00001-3 and hbi000057: Biomolecular modeling (at interfaces) within the HMI group*

hbb00001: Exploring the conformational phase space of N-linked glycans using enhanced MD and sketch-map analysis

hbb00002: Influence of Huntington peptide length on its conformational ensemble and binding to DNAJB1

hbb00003: Identification of residues involved in homotrimeric stabilization and function of the HumanP2X4R receptor channel by molecular dynamic simulations

hbi00057: Waste water pollutant adsorption on amorphous TiO₂ surfaces

HLRN Project ID:	<i>hbb00001</i>	<i>hbb00002</i>
Run time:	III/2020 – II/2023	III/2022 – II/2024
Project Leader:	Prof. Lucio Colombi Ciacchi	Dr. Susan Köppen
Project Scientists:	Isabel Grothaus	Isabel Grothaus
		<i>hbb00003</i>
		IV/2022 – III/2023
		Aparna Sai Malisetty
		<i>hbi00057</i>
		III/2022 – II/2023
		Maria von Einem
Affiliation:	Hybrid Materials Interfaces Faculty of Production Engineering University of Bremen	Hybrid Materials Interfaces Faculty of Production Engineering University of Bremen

The Hybrid Materials Interfaces (HMI) Group at the Faculty of Production Engineering of the University of Bremen is an Endowed Chair of the Conrad Naber Foundation lead by Prof. Lucio Colombi Ciacchi. The focus of its research lies on the atomic-level studies of interfaces between technological materials and biological macromolecules with applications in the fields of biomedical implants, biosensors, pharmaceutical packaging, biocompatible adhesives, and many others. The activities of HMI comprise both experimental research into biomolecular

Hybrid Materials Interfaces Group  (I) structure – function correlation in biomolecules
 (II) transmembrane protein complexes
 (III) posttranslational modifications
 (IV) molecular adsorption at solid – liquid interfaces

² Für den Inhalt der Projektberichte sind ausschließlich die genannten Projektleiter bzw. die Projektbearbeiter verantwortlich.

In the recently started project entitled “Identification of residues involved in homotrimeric stabilization and function of the HumanP2X4R receptor channel by molecular dynamic simulations” a combination of molecular dynamic simulations with experimental methods aims to address the role of specific residues for either stabilization or functionalization of this class of multi chain transmembrane ion channels.

In recent simulations we could show that intermolecular contact groups are located either in the transmembrane region or in the ecto domain of the channel at the extracellular side. Especially mutations of the respective ecto domain residues reveal destabilization of the trimeric molecular transmembrane complex. In addition, mutation of these residues leads to a significant inactivation of the ion channels (Figure 2).

The simulations have so far been limited to closed channel models. In a lab rotation with Master students of Biochemistry, we have also modeled the active form of the transmembrane complex. In further simulations, we would like to analyze atomistically the influence of the key mutations identified so far on the actual ion transport.

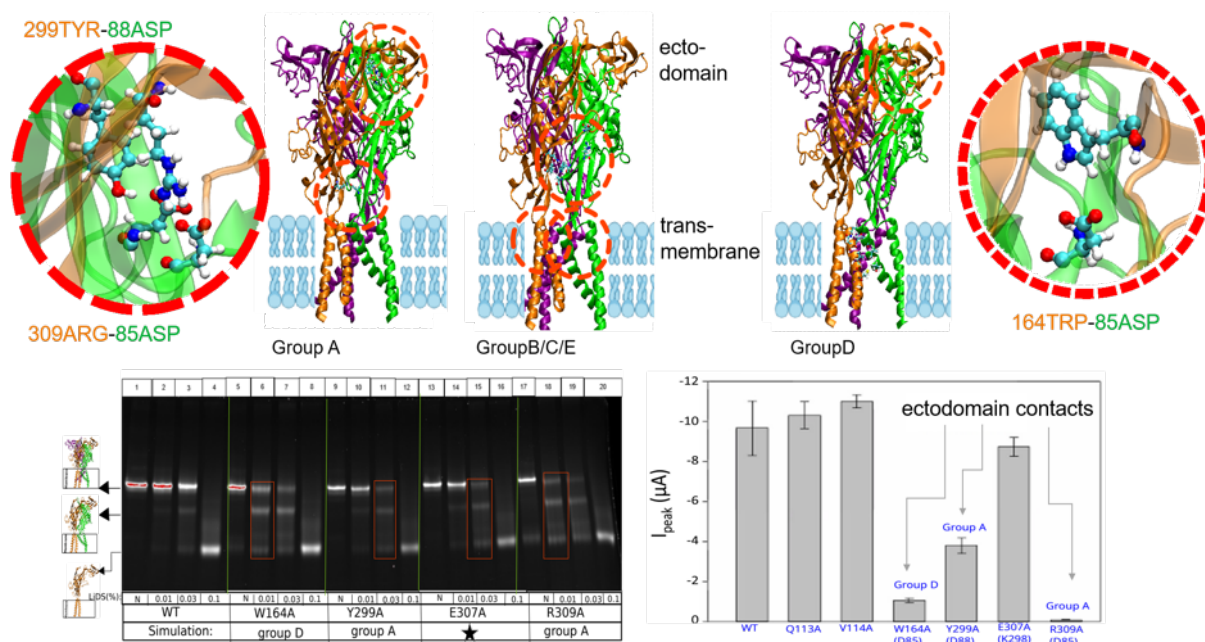


Figure 2: Molecular snapshots of the P2X4R closed state model. The location of identified interchain contact groups are highlighted with dashed red lines. SDS page and electrophysiological measurements show significant destabilization of the trimeric complex and reduction of the transport properties after mutation of key residues located at the ecto domain contact groups.

Postranslational modifications

The project entitled “Exploring the conformational phase space of using enhanced MD and sketch-map analysis” aims structure-property relationships in N-glycans.

Despite their fundamental biological relevance, posttranslational modifications in most of the protein simulations are fundamentally lacking. Especially for the glycosylation their highly multidimensional compositional and conformational phase-spaces remain largely unexplored. The torsional flexibility of the glycosidic linkages and the ring dynamics result in wide, rugged free-energy landscapes that are difficult to sample in molecular dynamics simulations. We

6.2 *hbc00045*: Rupturing materials in electric fields

HLRN Project ID:	hbc00045
Run time:	II/2020 – III/2023
Project Leader:	Prof. Dr. Tim Neudecker
Project Scientists:	M. Sc. Sourabh Kumar, M. Sc. Tarek Scheele
Affiliation:	University of Bremen Institute for Physical and Theoretical Chemistry Leobener Str. NW2 D-28359 Bremen

Overview

In mechanochemistry, forces are applied to initiate chemical reactions. This approach can be used in the production of mechanochromic materials, which change their color when a threshold stretching force is applied. In the case of a polymer, for example, a molecular subunit, the so-called mechanophore, is embedded in the polymer backbone. Upon application of stretching forces, the mechanophore changes its structure, e.g., via bond-rupture or cis-/trans-isomerization, which can be accompanied by color changes. The applications of this approach are immense, including optical strain detection in the construction industry, tamper-proof packaging, and self-healing materials.

Oriented external electric fields (OEEFs) have been used to catalyze a number of reactions by lowering the energy of a transition state if a zwitterionic resonance structure, which is favored in an OEEF, is present in the transition state (cf. Figure 1). Examples of reactions induced by OEEFs include enzymatic processes, isomerizations and Diels-Alder reactions. Moreover, it has been demonstrated that OEEFs reduce the bond dissociation energy of σ - and π -bonds and allow the switching of typically homolytic to heterolytic bond rupture processes.

In this project, mechanochemistry is coupled to the application of OEEFs in order to reduce the rupture forces of mechanophores in mechanochromic materials. While it is far from straightforward to conduct mechanochemical experiments in OEEFs due to the difficulty of controlling the relative orientation of the substrate and the electric field, computational chemistry offers the opportunity to rapidly screen a variety of mechanochemical reactions in OEEFs. The focus in this project lies on determining the rupture forces required to achieve the color switching process, using state-of-the-art computational methods.

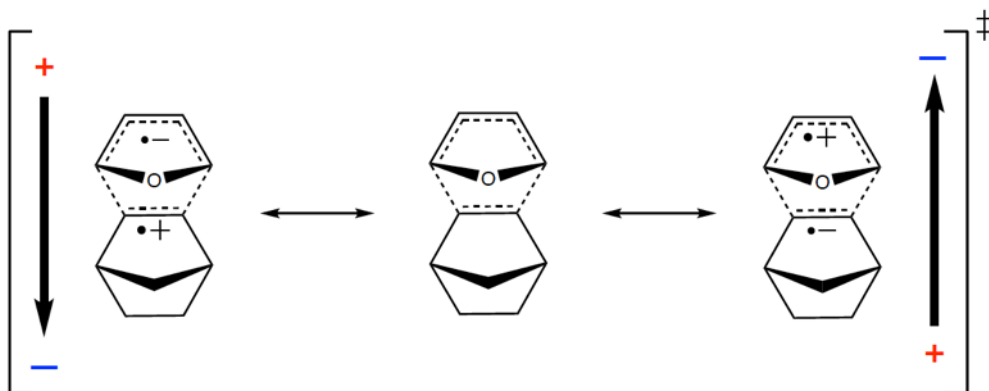


Figure 1: Schematic representation of the resonance structures in the transition state of a Diels-Alder reaction, which can be energetically favored in an oriented external electric field (OEEF).

Results

In the first phase of the project hbc00045, we conducted a thorough benchmark of density functionals that reproduce energetic and geometric changes of molecules induced by strong oriented external electric fields (OEEFs). High-level benchmark data was provided by CCSD[T]. We found that the rung of the density functional on Jacob's Ladder does not correlate with its reliability in predicting energetic and geometric properties of molecules in OEEFs, which was surprising, but, beneficially, provided us with proof that computationally inexpensive functionals can be used for conducting the rest of the calculations in hbc00045.

When writing the manuscript reporting on the results of the benchmark, we found several weaknesses of our data, which we could solve quickly with a moderate amount of computing power. We subsequently finished the manuscript, uploaded it to a preprint server[1] and submitted it to a journal. It was sent to two reviewers, who had critical – but ultimately helpful – comments that we are currently addressing by running additional calculations.

In our last follow-up proposal we also referred to our calculations on the mechanical properties of a model mechanophore in an OEEF. The full set of calculations on three mechanophores (spiropyran, benzocyclobutene and a model molecule featuring a disulfide bond) in a polymer chain are now finished and the relative orientation of the electric field w.r.t. the scissile bond has been tested (Figure 2), which, as expected, consumed most of the computational resources granted to us within the past year. The results agreed well with our hypothesis: OEEFs that are aligned with the scissile bond weaken the mechanophore and decrease the rupture force. The extent of the weakening correlates well with the alignment of the OEEF with the scissile bond. A manuscript detailing our findings will be published shortly.

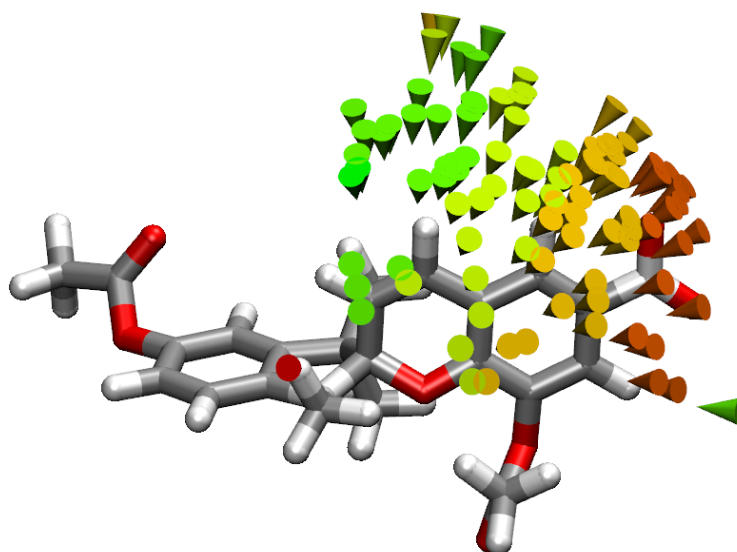


Figure 2: Dependence of the rupture force of the scissile bond in spiropyran on the orientation of the OEEF (strength: 0.01 a.u.). Colored cones represent directions of the OEEF. Red cones signify maximum weakening of the mechanophore, whereas green cones denote a small influence of the OEEF on the rupture force.

Outlook

Two of the goals of the previous project phases have not been attained yet: 1) The comparison between homolytic and heterolytic bond cleavage upon simultaneous application of mechanical force and an OEEF using multireference simulation approaches, and 2) a comparison between the influences of oriented internal electric fields (OIEFs) and OEEFs.

Within the next phase of the project, the first of these goals will be abandoned. The main reason for this is the appearance of a preprint that investigates homolytic bond cleavage in OEEFs in detail, thus reducing the novelty of our previous goal significantly. Moreover, since multireference methods such as CASPT2 are computationally very expensive, scale poorly with the number of nodes and cannot be restarted, it is very likely that a certain proportion of the calculations will not finish within the maximum walltime.

Instead, the focus will be placed on an in-depth comparison between OIEFs and OEEFs at the molecular level, with a scope that is significantly expanded as compared to the last follow-up proposal, as explained below. In addition, we acknowledge that at this point we have already conducted a large amount of calculations at the level of isolated molecules and are now ready for taking our simulations to a larger scale by simulating mechanophores in complex polymer environments under the simultaneous influence of strain and OEEFs.

In particular, three objectives shall be met within the next year:

- Objective 1: The effect of OIEFs and OEEFs on mechanical properties of molecules will be compared in great detail.
- Objective 2: Mechanophores shall be incorporated into a complex polymer environment and the effect of strain on their mechanical properties will be elucidated in a multiscale simulation setup.
- Objective 3: OEEFs will be applied to the system created in objective 2 and the influence of electric fields on the mechanical properties of mechanophores in complex polymer environments will be elucidated.

To achieve this goal, we have designed a comprehensive work program that is to be completed within the year 2023. The first part of the work program focuses on an in-depth comparison between OIEFs and OEEFs, for which we have designed a number of example molecules. A particular emphasis will be placed on comparisons of the mechanical properties of these molecules in the different electric field scenarios. Subsequently, complex polymer environments will be generated in the LAMMPS software package, which will include mechanophores. In a first step, different types of strain (elongation, compression, shear) will be applied in the absence of OEEFs. Subsequently, the same strain modes will be applied in the presence of OEEFs. This will enable much more realistic comparisons to experiments, since in experimental setups it is next to impossible to align a mechanophore with an OEEF perfectly.

Publications

1. T. Scheele, T. Neudecker, *How Accurate is Density Functional Theory for Molecules in Electric Fields?* ChemRxiv, DOI: 10.26434/chemrxiv-2022-db090 (2022)

Presentations

2. T. Scheele, *How Accurate is Density Functional Theory for Molecules in Electric Fields*, Symposium on Theoretical Chemistry, Heidelberg, September 2022

6.3 **hbc00056: Towards an atomic-level understanding of the interaction of probe molecules with acid sites in zeolites**

HLRN Project ID:	hbc00056
Run time:	III/2021 – II/2022 (1 st phase), III/2022 – II/2023 (2 nd phase)
Project Leader:	Dr. Michael Fischer
Project Scientists:	Dr. Michael Fischer, Carlos Bornes
Affiliations:	MF: Crystallography & Geomaterials Research Group, Faculty of Geosciences, University of Bremen; Bremen Center of Computational Materials Science, University of Bremen; MAPEX Center for Materials and Processes, University of Bremen, Bibliothekstraße 1, 28359 Bremen CB: CICECO, Aveiro Institute of Materials, Department of Chemistry, University of Aveiro, 3810-193 Aveiro, Portugal

Overview

The adsorption of probe molecules like ammonia, pyridine, or trimethylphosphine oxide is a common technique to characterize protonated zeolites, which are important solid acid catalysts. However, recent work has shown that the interpretation of experimental results is less straightforward than commonly assumed, because more than one probe molecule can interact with a single acid site. In this project, electronic structure calculations in the framework of density functional theory (DFT) and DFT-based molecular dynamics simulations are performed to shed light on the interaction between protonated zeolites and probe molecules. The calculations are carried out in close collaboration with experimental partners, who employ advanced nuclear magnetic resonance (NMR) experiments to investigate these systems.

Scientific Background

Zeolites are inorganic tetrahedral framework materials exhibiting an intrinsic porosity. In addition to applications in ion exchange and separation, they are used as solid acid catalysts in several large-scale industrial processes.[1,2] The economically most significant application is the fluid catalytic cracking of heavy hydrocarbons into lighter fractions, a key step in the production of fuels and feedstocks from crude oil. Highly siliceous zeolites, the most important zeolite catalysts, contain relatively small amounts of tetrahedrally coordinated aluminium atoms, the remainder of the tetrahedral sites being occupied by silicon. In protonated zeolites, the negative charge of the framework is balanced through protons bonded to framework oxygen atoms of the AlO_4 tetrahedra. The overall catalytic activity of zeolites strongly depends on the location, amount, and acid strength of these framework protons, which act as Brønsted acid sites. Hence, a comprehensive characterization of the acid site properties is pivotal to develop increasingly active and selective catalysts.[3,4]

Probe molecules like ammonia, pyridine, and trimethylphosphine oxide (TMPO) have been widely used to study the acid properties of zeolites, as they can provide information about acid-base interaction and accessibility of the acid sites. Studies employing probe molecules typically identified “fingerprint” vibrational modes (in vibrational spectroscopy) or distinct chemical shifts (in NMR spectroscopy), which are commonly assigned to probe molecules interacting with Brønsted acid sites having different acid strength.[3,4] However, computational studies have shown consistently that the deprotonation energy of zeolites, often considered as the “true” measure of acid strength, is homogeneous and largely independent of the acid site location and the zeolite framework.[5,6]

This project aims to enhance the atomic-level understanding of the interaction of protonated zeolites with ammonia, pyridine, and TMPO through DFT calculations. To study the impact of the local environment, two zeolites with channels of different size were included in the investigation (MFI and MOR, see **Figure 1**), and different positions of framework Al atoms and charge-balancing protons were considered for each of them. In the first project phase, DFT structure optimizations, which deliver equilibrium structures of adsorption complexes and adsorption energies in the absence of thermal motion, were complemented by DFT-based *ab initio* molecular dynamics (AIMD) simulations to include temperature effects. The second phase, which is ongoing, is aimed at a DFT-based prediction of NMR chemical shifts and vibrational modes and their comparison to experimental data. To this end, advanced NMR experiments are carried out by the collaboration partners at **CICECO, Aveiro Institute of Materials, Portugal** (Carlos Bornes, Dr. Luís Mafra, Prof. Dr. João Rocha).

Funding of the project scientists is provided through a DFG Heisenberg grant to Dr. Michael Fischer (Deutsche Forschungsgemeinschaft project no. 455871835, Fi1800/6-1), and through a PhD scholarship from the Portuguese Fundação para a Ciência e Tecnologia (FCT) to Carlos Bornes (ref. PD/BD/142849/2018).

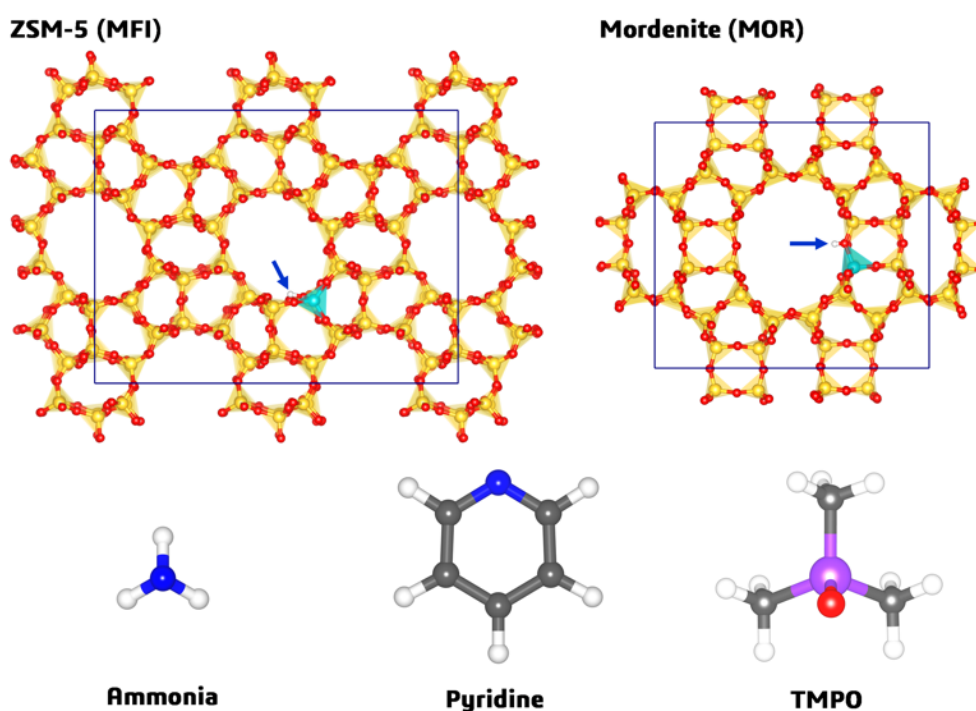


Figure 1: Zeolites and probe molecules considered in this investigation. **Top:** MFI (ZSM-5) contains a two-dimensional system of channels formed by ten-membered rings of TO_4 tetrahedra (10MRs), MOR (mordenite) contains a one-dimensional system of 12MR channels. Yellow = silicon, turquoise = aluminium, red = oxygen, white = hydrogen. Positions of the framework protons are emphasized by arrows. **Bottom:** Probe molecules. Blue = nitrogen, grey = carbon, purple = phosphorus. Note that probe molecules are not shown on the same scale as the zeolite crystal structures.

Project Results

After confirming the stability of the guest-free zeolite models through a combination of DFT structure optimizations and AIMD simulations, 1:1 complexes of ammonia, pyridine, and TMPO in the different models were constructed (1:1 complex = one probe molecule per acid site). DFT-optimized adsorption complexes were compared to structures that were subjected to a short AIMD simulation (~10 picoseconds, temperature: 150 °C) prior to optimization. For all

three probe molecules, the interaction with the acid site resulted in framework deprotonation, *i.e.*, an abstraction of the proton from the framework and formation of a cation in the pores. Whereas only limited movement away from the acid site was observed in AIMD simulations of pyridine- and TMPO-containing systems, the ammonium cation was found to diffuse through the structure. Calculations for 2:1 complexes showed larger differences between structures obtained from DFT optimizations and from AIMD simulations. The formation of probe molecule dimers, typically found to be energetically favored, was not always captured when using standard optimization routines. This indicates that the computationally more demanding AIMD simulations are crucial for a realistic modelling of dimer formation.

In the second project phase, a portfolio of DFT-based methods is used to predict ^{31}P and ^{15}N chemical shifts as well as vibrational modes of low-energy adsorption complexes, so far focusing on 1:1 complexes. Calculations of ^{31}P chemical shifts in TMPO-loaded MFI and MOR corroborated that the chemical shift is sensitive to the Brønsted acid site location. For MFI, calculations for models with three different locations of the acid site (sinusoidal channel, straight channel, channel intersection) delivered three distinct resonances at 66, 68, and 74 ppm, agreeing with the previously reported experimental results (64, 69, and 76 ppm). **[P1]** In most instances, similar ^{31}P chemical shifts were obtained for complexes obtained from structure optimizations and AIMD simulations. The rather large difference observed for a complex where TMPO is located in the sinusoidal channel of MFI can probably be attributed to a motion of TMPO towards the channel intersection. Computations for zeolites loaded with ammonia and pyridine also predicted an influence of the acid site location on the ^{15}N chemical shift. However, due to the low natural abundance of ^{15}N , the number of experimental NMR studies is very limited. One investigation of MFI loaded with ^{15}N -enriched pyridine suggested that a broad ^{15}N resonance at -176 ppm arises from the interaction with Brønsted acid sites.[7] This value agrees very well with our DFT value of -173 ppm, obtained for a model where the acid site is at the MFI channel intersection. Another study using ^{15}N -enriched ammonia loaded onto MFI reported ^{15}N resonances in the range of -360 to -368 ppm.[8] While DFT-computed values are similar (-365 to -373 ppm), they are more dependent on the inclusion/neglect of dynamics than on the location of the acid site.

In addition to NMR chemical shifts, vibrational modes of 1:1 complexes were also predicted using DFT calculations. **Figure 2** shows the displacement patterns of selected vibrational modes of pyridine, commonly used to study the acidity of zeolites,[9] together with the DFT results computed for pyridine in MFI models with different acid site locations. The frequencies of the fingerprint modes are distinctly shifted with respect to those of free pyridine (numerical values given in **Figure 2** [10]), corroborating that the interaction with the acid site affects the vibrational spectrum. Even though some differences in the frequencies obtained for different MFI models are visible, a preliminary analysis seems to suggest that vibrational spectroscopy is less well suited to distinguish different acid site locations than NMR spectroscopy.

Outlook

Future calculations of NMR chemical shifts and vibrational modes will expand the analysis to 2:1 complexes and to zeolite models containing more than one acid site per unit cell. On this basis, it will be analyzed how an adsorption of two probe molecules in proximity will affect experimentally observable quantities. Due to the lack of literature data for ^{15}N chemical shifts of pyridine or ammonia adsorbed in zeolites, the collaborators at CICECO will perform ^{15}N NMR measurements using ^{15}N -enriched probe molecules in order to allow for a comparison of the DFT results to experiment. Furthermore, a more comprehensive analysis of the DFT-computed vibrational spectra can be complemented by in-situ infrared spectroscopy.

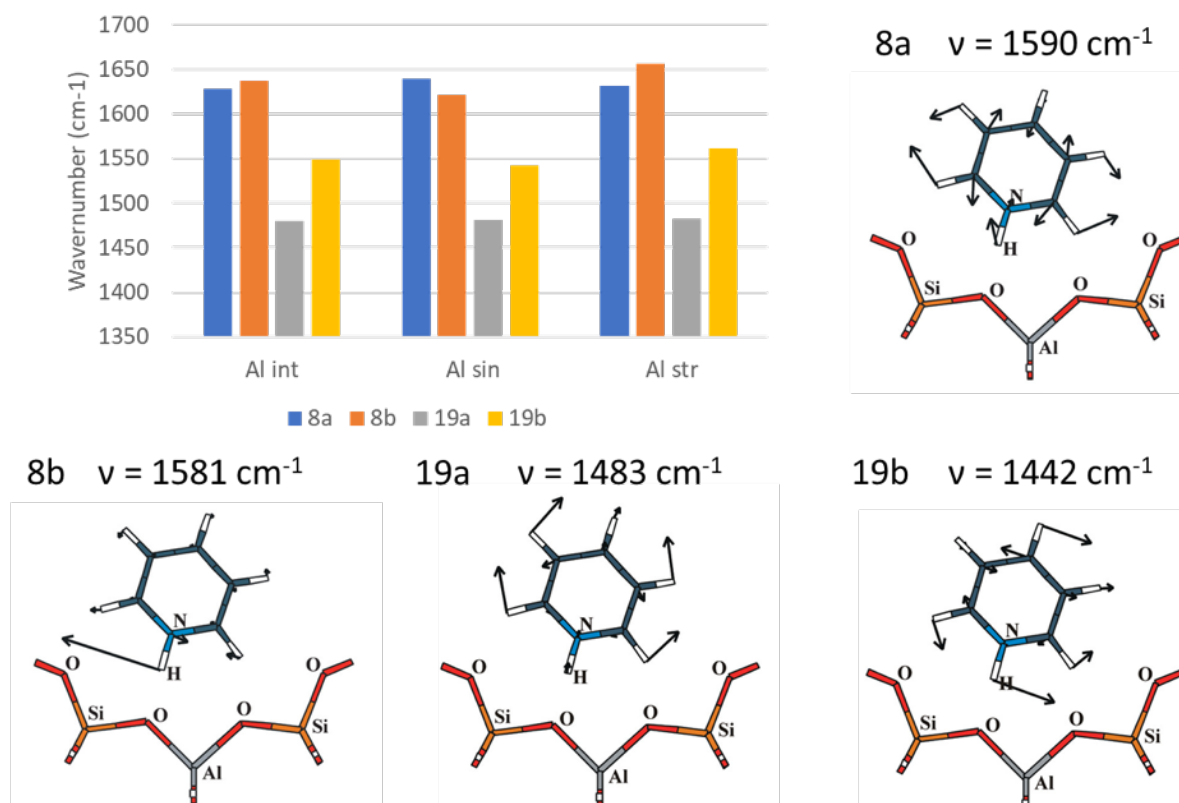


Figure 2: Calculated vibrational modes of pyridine adsorbed in three MFI models (Al int/sin/str = acid site at channel intersection/sinusoidal channel/straight channel). The schematic representation of the modes was adapted from reference [9]. Experimental frequencies of free pyridine are also given.[10]

Publications

- P1** C. Bornes, M. Fischer, J. A. Amelse, C. F. G. C. Geraldes, J. Rocha, L. Mafra, *What Is Being Measured with P-Bearing NMR Probe Molecules Adsorbed on Zeolites?*, *J. Am. Chem. Soc.* **143**, 13616–13623 (2021)

Presentations

- P2** C. Bornes, *Unravelling the mysteries of zeolites' acidity with solid-state and NMR and computational modelling*, Portuguese NMR meeting, Aveiro, November 2022

References

- [1] G. Busca, *Chem. Rev.* **107**, 5366–5410 (2007)
- [2] A. Primo, H. Garcia, *Chem. Soc Rev.* **43**, 7548–7561 (2014)
- [3] L. E. Sandoval-Diaz, J. A. González-Amaya, C. A. Trujillo, *Microporous Mesoporous Mater.* **215**, 229–243 (2015)
- [4] G. Busca, *Microporous Mesoporous Mater.* **254**, 3–16 (2017)
- [5] A. J. Jones, E. Iglesia, *ACS Catal.* **5**, 5741–5755 (2015)
- [6] P. Deshlera, E. Iglesia, *Chem. Commun.* **56**, 7371–7398 (2020)
- [7] T. Xu et al., *J. Am. Chem. Soc.* **119**, 12231–12239 (1997)
- [8] V.M. Mastikhin, S.V. Filimonova, *J. Chem. Soc., Faraday Trans.* **88**, 1473–1476 (1992)
- [9] M. Castellà-Ventura, Y. Akacem, E. Kassab, *J. Phys. Chem. C* **112**, 19045–19054 (2008)
- [10] T.D. Klots, *Spectrochimica Acta A: Mol. Biomol. Spectr.* **54**, 1481–1498 (1998)

6.4 *hbc00057*: Towards a molecular description of the conformational ensemble of miRNA

HLRN Project ID:	hbc00048
Run time:	III/2021 – II/2022
Project Leader:	Dr. Massimo Delle Piane
Project Scientists:	Dr. Monika Michaelis, Prof. Lucio Colombi Ciacchi
Affiliation:	Bremen Centre for Computational Materials Science (BCCMS) and Hybrid Materials Interfaces (HMI) group, Faculty of Production Engineering, University of Bremen

Overview

Errors in cell signaling, which cause an uncontrolled cell proliferation, can develop from misexpressions or dysfunctions of microRNA (miRNA). MicroRNAs are small endogenous RNAs, approximately 22 nucleotides in length, which regulate eukaryotic gene expression on the post-transcriptional level. They work as a guidance for mRNA, to prevent it from expressing the wrong proteins. Gene therapy is a kind of targeted therapy, that uses genetic material to modify the signaling pathways and thereby the gene expression within cells. The introduction of miRNAs into human cells could provide an efficacious therapeutic approach to inhibit tumour progression. The delivery of miRNAs has been tested with functionalized gold nanoparticles, combined with either the stem-loop or hairpin structure of a miRNA. More recently chitosan–miRNA (CS–miRNA) complexes have been proposed as delivery systems, and their structure–function relationship has been investigated.

MicroRNA 145 is known to be dysregulated in endometriosis. Delivered to the cells, it has been found to inhibit breast cancer and endometriotic cell invasiveness, marking this reagent as a potential candidate for novel antimetastatic therapeutic applications. To this purpose, the cell-relevant part of this miRNA is considered for delivery. One strand (hsa- miR-145-5p) is the one having medical effectiveness. To increase stability, it is delivered together with its stabilizing partner (hsa-miR-145-3p), forming a duplex. Determining the stability and structure of both the individual components and their duplex is therefore of paramount importance to advance the therapeutic applications of this miRNA.

The structure of RNA plays a crucial role for its functionality in biological systems as well as for the functionality of the cell-relevant components. Among solution-based methods, electronic Circular Dichroism (CD) spectroscopy is widely used for identifying and quantifying the secondary structures of solvated biomolecules, including nucleic acids. Interpretation is however not straightforward due to a lack of atomistic information on the conformational origin of the specific signals. Molecular dynamics (MD) simulations in principle provide a powerful tool to access RNA dynamics at virtually unlimited space and time resolution, and can be performed in an environment very similar to that used in CD. However, their result is often not satisfactory mostly due to the short accessible time-scales and the inaccuracy of the employed force fields. The former issue can be tackled using enhanced sampling methods.

In this project, due to its importance for the functionality of cancer treatment, hsa-miR-145, and its components will be analyzed in greater depth combining our Circular Dichroism spectroscopy experiments with enhanced sampling MD. The calculations of CD spectra from simulated ensembles, will be used to gain novel understanding on the origin of the spectral changes with increasing temperature for miRNA.

Particularly, the general question we aim at answering during the proposed project is: What is the underlying conformational variability of miRNAs structures and how does it impact the structural/CD spectra relationship?

Results

Starting from secondary-structure information available in the miRBase databank, we used the make-na web server to obtain an associated 3D model of the cell-relevant duplex of miRNA-145 and the Rosetta Online Server for the structural prediction of the individual 3p and 5p strands. We characterized these predicted models, by employing temperature ramping simulations, ranging from 300K to 700K, to characterize the thermal stability (Figure 1). We followed the denaturation, by following structural parameters, such as the number of base-base hydrogen bonds and the distribution of the backbone characteristic angles. The melting pattern of nucleic acids, and the corresponding characteristic melting temperature T_m , can give important information on their conformation and stability, and key features or properties of their folding landscape. Based on these results, we calculated the CD spectra with DichroCalc and compared the simulated CD spectra to our experimental data of melting. This acted both as validation of the model and as an atomistic understanding of the measured spectra.

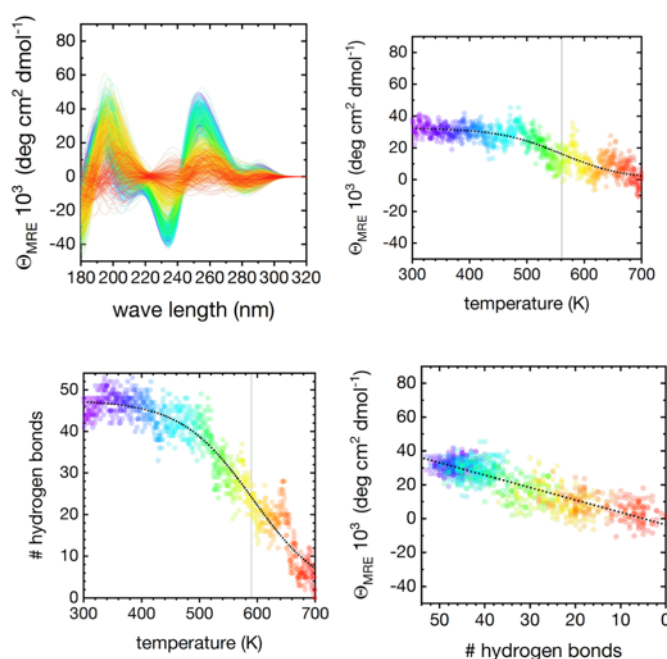


Figure 1: Simulation of the denaturation of the cell relevant component of miRNA-145 from 300 to 700 K. (top, left) Simulated CD spectra at different temperatures. (top, right) Variation with temperature of the CD intensity at 260 nm. (bottom, left) Variation with temperature of the number of inter-strand hydrogen bonds. (bottom, right) Correlation between CD intensity at 260 nm and number of inter-strand hydrogen bonds.

As a subsequent step, we probed the conformational landscape of hydrogen-bonded duplex resulting from the hybridization of the cell-relevant parts of miRNA 145, hsa-miR-145-5p and hsa-miR-145-3p. We used Replica Exchange with Solute Tempering (REST2) simulations to allow a sampling of the conformational phase space. With this approach, we did not explicitly bias specific conformational degrees of freedom, to gain a sampling as complete as possible with respect to structure. Aware that the size of the investigated strands is well above the current state of the art in RNA folding simulations, and that convergence could not be achieved

also with the simulation length made available by HLRN, these costly enhanced sampling simulations still provided a never before achieved qualitative overview of the conformational variability of these molecules. We studied structural variability by following metrics, such as base-base hydrogen bonds, RMSD, ϵ RMSD24, backbone torsional and pseudotorsional angles (Figure 2).

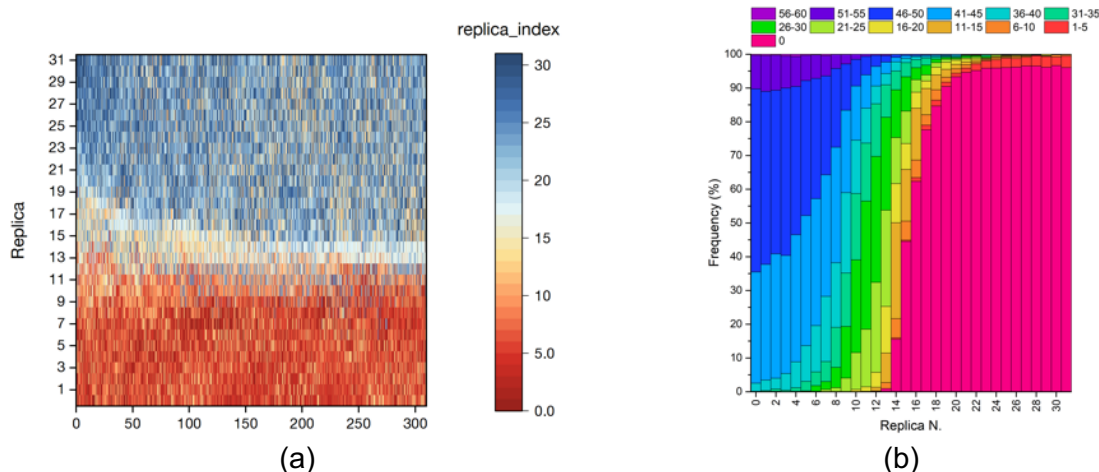


Figure 2: REST2 simulation of the conformational phase space of the miRNA 145 duplex (a) Temperature position of each replica as the REST simulation progresses. (b) Number of inter-strand hydrogen bonds across the temperature replicas, showing a denaturation pattern.

Outlook

We will calculate the CD spectra with DichroCalc on all structures in the simulated ensemble and compare the simulated CD results to our experimental CD spectra. By doing this we will be able to determine how the structural variability impacts the spectral variability and we will use this comparison to pinpoint the most probable conformations of the single strands in solution. Finally, we will also probe the conformational landscape of the cell-relevant parts of miRNA 145, namely hsa-miR-145-5p.

We believe that the obtained results, although obtained for a selected miRNA duplex and its single strands, will be of general interest within the larger cancer research and drug delivery communities, adding atomistic understanding to experimental results. This will provide essential information for the progress of miRNA-based therapeutics from laboratory research to further stages in pharmaceutical design and production.

6.5 *hbc00060: Creating a two-dimensional electron gas in a bulk crystal*

HLRN Project ID:	hbc00060
Run time:	IV/2021 – III/2022
Project Leader:	Dr. Bálint Aradi
Project Scientists:	Prof. Peter Deák
Affiliation:	University Bremen, Bremen Center for Computational Materials Science

Overview

High electron mobility transistors (HEMT), based on a 2D electron gas (2DEG), are by now commercially utilized in high-power and high-frequency electronic applications. In any known practical realization of 2DEG-based devices, an interface has to be constructed, and this limits the volatility of device design (horizontal vs. vertical). It has been shown that a high mobility 2DEG can be formed also at the (001) surface of anatase-TiO₂, whereas STM studies on the (101) surface of Nb-doped anatase revealed a 2D electronic state of finite spatial extent, extending into the bulk along a (001) plane. Therefore, the question arises whether such states could be created in a controlled manner to form a 2DEG in the bulk of anatase and in other similar materials.

Using sophisticated electronic structure calculations, we have found a state similar to the one observed in the STM measurements. In order to answer the question above, the following had to be clarified.

- Is the state we see really identical with the one observed in STM, i.e., does it have the same spatial extent and ionization energy?
- What is its relation to the dopant, i.e., is it a shallow donor state or a medium sized polaron bound by the ionized donor?
- Can this state be created anywhere in the bulk, and if yes, is it related to the large polaron observed in anatase by ARPES measurements?
- Since these states have a finite spatial extent, can they be arranged to give rise to a 2DEG
- Do these states occur in other materials as well?

Results

In our past projects, we have developed the methodology to deal with polaronic states. Here we applied a well validated parametrized method (DFT+U) to a big periodic (supercell) model of the anatase (101) surface (1920 atoms), and a highly accurate method (HSE hybrid functional) to bulk anatase and BaTiO₃.

Replacing a surface Ti atom with Nb (which introduces an extra electron w.r. to the former), we have been able to find the 2D state extending into the bulk along the (001) plane. Comparing the simulated STM image, as well as the calculated energy of the state (w.r. to the conduction band), to the actual picture seen in STM and the peak position measured by STS, respectively (Fig. 1), convincingly demonstrates that the state we calculate is identical with the one observed. The wave function of our 2D state is not centered on the Nb dopant but on a Ti atom in the next (001) layer. This means that this is not a shallow donor state but a medium sized polaron.

ARPES measurements describe a “large polaron” state in anatase with about the same energy, so it is conceivable that those are actually similar medium-sized 2D states far from the donors (in case of the ARPES measurements, oxygen vacancies). Indeed, as Fig. 2a shows,

we have been able to localize 2D states in bulk anatase supercells by adding an extra electron but no donor atom. We submitted our results for publication to *Physical Review Letters* [1], and we are now awaiting the decision on the revised manuscript. We also highlighted the consequences for photocatalysis in an invited talk at a CECAM Flagship Workshop [2].

We have investigated the possibility of lining up such medium size 2D polarons in one plane but found no substantial energy gain (but no loss either). Therefore, a spontaneous formation of 2DEG in macroscopic size cannot be expected. However, implanting dopants with a shallow depths profile is possible, and this way the 2DEG could be created. Unfortunately, macroscopic anatase single crystals cannot be grown (since rutile is the stable form of TiO_2), so some other material has to be found. BaTiO_3 single crystals are readily available, and implantation was already used to dope them. As shown in Fig.2.b, we have succeeded to localize a 2D polaron in the (001) plane of BaTiO_3 too. The reason for the 2D behaviour is the large anisotropy of the Bohr-radius and the electron-phonon coupling constant in both materials, so similar behaviour can be expected in other crystals with similar anisotropy.

Outlook

We suspect that the 2DEG observed in [001]-oriented anatase (capped with a LaAlO_3 layer) arises actually due to overlapping medium-sized 2D polarons, confined between the layer of vacancies, created by ion-irradiation, and the interface. This could be proven by calculating the lateral electron mobility in the plane of our 2D polaron in the bulk, since the periodic model ensures the overlap of these states. To do that at a sufficiently high level of theory, however, requires further development of our tool-kit for calculating transport properties. This is planned in the near future. Proving that the observed 2DEG in anatase arises this way, could pave the way for HEMT devices with a 2DEG created in the bulk in a controlled manner.

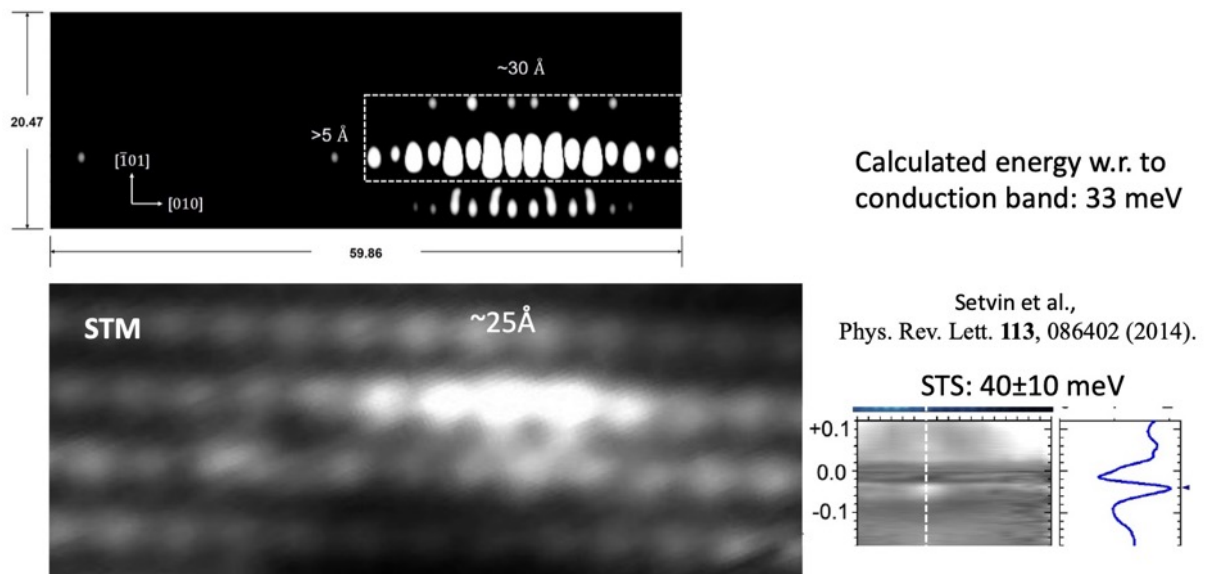


Figure 1: Comparison of the calculated results (top) to actual STM and STS measurements.

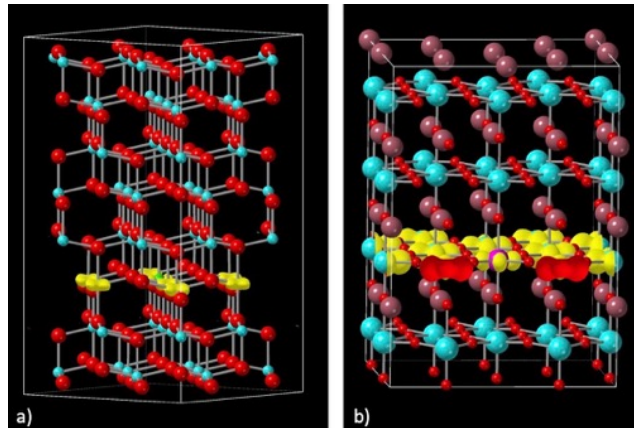


Figure 2: 2D polaron states (yellow lobes) in anatase-TiO₂ (a) and BaTiO₃ (b). Blue, brown and red spheres represent Ti, Ba, and O atoms, respectively.

Publications

1. T. Mou, V. K. Gupta, M. Farzalipour Tabriz, B. Aradi, T. Frauenheim, P. Deák *The size of electron polarons in anatase-TiO₂ and their role in photocatalysis.*, Phys. Rev. Lett., *submitted*

Presentations

1. P. Deák *Polaronic effects in TiO₂*, CEACM Flagship Workshop New Horizons in Photoelectrochemical Water-Splitting and Heterogeneous Catalysis: Bridging Theory, Simulation and Experiment, May 31, 2022

6.6 *hbc00061*: Studying the Wet and Dry CO Oxidation on Nanoporous Gold Using Static DFT Computations and AIMD Simulations

HLRN Project ID:	hbc00061
Run time:	IV/2021 – III/2022
Project Leader:	Dr Lyudmila Moskaleva
Project Scientists:	Shikun Li, Lenard Carroll
Affiliation:	Universität Bremen, Institut für Angewandte und Physikalische Chemie, Leobener Str. UFT, 28359, Bremen

Overview

Investigating the adsorption behavior and reactivity of catalytically relevant molecules on well-defined gold surfaces offers valuable insight into the catalytic activity of gold-based nanocatalysts, such as nanoporous gold (np-Au). In this project, we aim to provide a comprehensive understanding of surface reactivity, replacing an idealized picture of a perfect, clean, and rigid catalyst surface with one that is covered by adsorbates and dynamically changes during catalytic transformations.

This research seeks to gain further insights into the chemistry of np-Au through a combination between traditional (static) calculations based on density functional theory (DFT) and *ab initio* molecular dynamics (AIMD) simulations. The work of the DFG Research Unit NAGOCAT has already revealed that the surface chemistry of np-Au is more complex than initially expected. This complexity arises from the interactions between gold, chemisorbed O atoms generated and consumed during catalysis, and trace amounts of Ag impurities present in np-Au. In fact, adsorbed atomic O on its own can lead to rapid restructuring with metal diffusion happening at the same time. In particular, the presence of oxygen can cause admetal Ag segregation and the formation of quasi ordered Au-O-Au-O chains.

To gain a better understanding of these surface evolution processes, we are using AIMD simulations to study the surface reactivity. In particular, we aim to investigate the adsorption and oxidation of carbon monoxide (CO), which is a common prototypical reaction in heterogeneous catalysis.

Results

We have investigated the self-organization of oxygen atoms on Au(221) surfaces, as well as the process of restructuring of these surfaces. All simulations were run at 700 K (a high temperature is required to accelerate all processes). The results are illustrated in Figure 1. Initially, O atoms were randomly placed on the Au(221) surface, and the initial structure was pre-optimized. After 200 ps, the oxygen atoms self-organized into $-(\text{Au}-\text{O})-$ chains and after an additional 50 ps, these chains were further elongated. Throughout the simulation, the terraces were flattened and the temperature fluctuated regularly between 600 K and 750 K. Our simulation showed that, (i) oxygen atoms adsorbed on a stepped Au

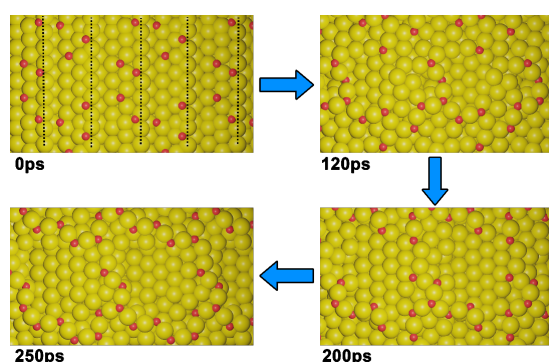


Figure 1: Snapshots of the Au(221) + 8O simulation. The gold and red spheres represent Au and O atoms, respectively.

surface can form chains spontaneously, and (ii) the process is accompanied by the restructuring of the surface, in which bare Au steps are flattened and wide flat terraces are formed, while the steps decorated by oxygen atom chains are stabilized. Furthermore, chains of Au adatoms on the surface linked by O atoms were created. Such Au adatoms may become active reactive centers once O atoms linking them are reacted away by CO.

Moreover, an AIMD simulation of multiple CO molecules adsorbed on a Au(221) structure was conducted in order to investigate the formation of AuCO complexes and restructuring of the Au(221) surface, Figure 2. Initially, CO molecules were randomly placed on the Au(221) surface, and the structure was pre-optimized. Results indicated that most CO molecules favoured adsorbing at step edges on top of Au atoms rather than occupying a bridge site. Furthermore, the formation of multiple AuCO complexes has been observed. Additionally, significant movement of the step Au atoms has been noted.

Similarly, we have found that AuCO complexes are important in simulations involving CO and O, as not only does this species form often throughout the simulations, but it is also more mobile, allowing for a faster CO₂ formation. The root mean square deviation (RMSD) calculations throughout the simulations demonstrates well the difference in mobility of AuCO versus CO, as depicted in Figure 3.

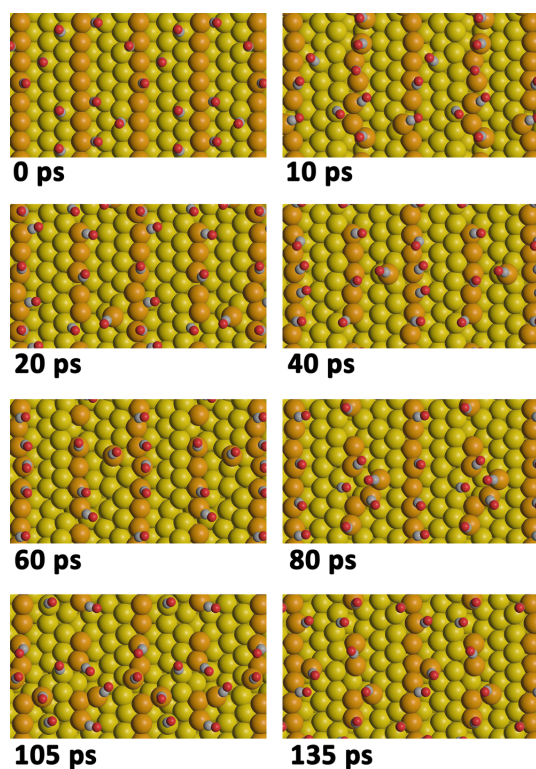


Figure 2: Snapshots from the AIMD simulation of CO molecules adsorbed on top of a regular Au (221) surface. Darker shade of gold indicates Au atoms at the step edge at the start of a simulation. O atoms are shown in red, C atoms in gray.

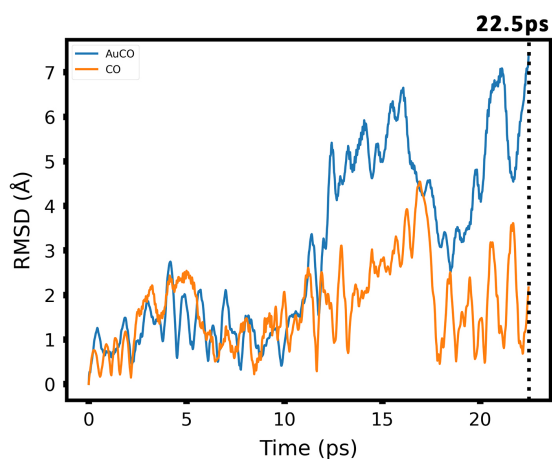


Figure 3: RMSD of CO and AuCO (geometrical center) in the x-direction over 22 ps of simulation time.

We investigated the reactivity of a one-dimensional chain of oxygen atoms along a step on an Au(221) surface with oxygen vacancies, serving as a prototype for a 1D surface gold oxide. Upon comparing the adsorption of CO and O₂ on the oxygen chain with that of an oxygen-free Au(221) surface, our results indicated that O₂ adsorbs more strongly on the O chain (at a double oxygen vacancy site), resulting in a nearly 1 eV lowering of the the reaction barrier for O₂ dissociation, as shown in Figure 4 a, b.

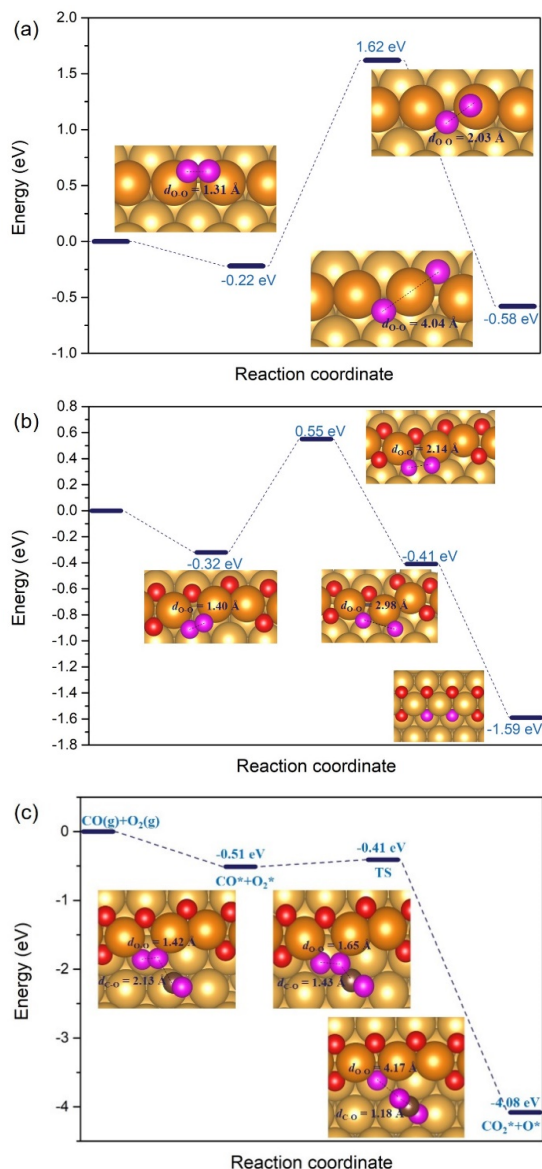


Figure 4: The reaction energy diagram for the dissociation of O₂ adsorbed on (a) the regular Au (221) surface, and (b) the double chain with two adjacent vacancies on the Au (221) surface, as well as (c) the reaction profile of the reaction between the co-adsorbed CO and O₂ on the two adjacent vacancies. O atoms of the chain structure are shown in red, while the O atoms of the O₂ molecule are shown in pink. C atoms are shown in black.

When it comes to the reaction of CO and O₂, two mechanisms are possible, a dissociative and an associative mechanism. For the associative mechanism, when the two molecules react, an OCOO intermediate is formed which eventually breaks down into an adsorbed oxygen atom and a CO₂ molecule. In some cases, it can even proceed as a concerted process without forming an OCOO intermediate. For the dissociative mechanism, the oxygen molecule first dissociates into two adsorbed oxygen atoms, with one of these oxygen atoms reacting with CO to form CO₂ in a subsequent step.

The rate-limiting step in the dissociative mechanism corresponds to the dissociation of O₂, with an energy barrier of 1.84 eV on the regular Au(221) (Figure 4a). This is considerably higher than the energy barrier (0.87 eV) on a double oxygen chain with two adjacent vacancies (Figure 4b).

For the associative mechanism, where CO initially adsorbs at the terrace site and O₂ adsorbs at the vacancy site, the energy barrier of the rate-limiting step is significantly reduced to 0.1 eV, corresponding to the direct formation of CO₂ and healing of an O vacancy (Figure 4c). Moreover, the reaction is exothermic, releasing 3.57 eV relative to the initial co-adsorption state of CO and O₂. This shows that the associative mechanism is energetically preferred over the dissociative one.

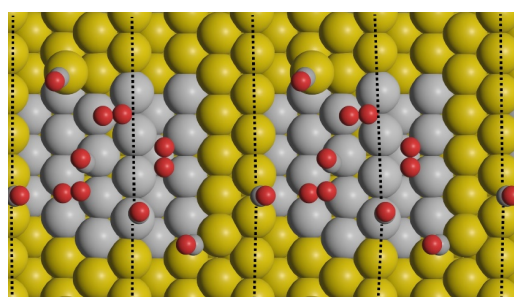


Figure 5: Snapshot of an AIMD simulation of CO and O₂ molecules adsorbed on top of a bimetallic AuAg(221) surface. Vertical lines highlight step edges. Large yellow and gray spheres represent Au and Ag, respectively; small red and gray spheres denote O and C, respectively.

Additionally, AIMD simulations were used to investigate the reaction between CO and O₂ molecules on a bimetallic AuAg(221) surface. The results indicated an associative mechanism occurred, where an OCOO intermediate was formed which then dissociated into an O atom and a CO₂ molecule. Subsequently, the dissociated O atoms were found to be able to react with additional CO molecules to produce more CO₂ molecules. The simulation also revealed that the surface experienced minor restructuring during this reaction.

Outlook

In the next phase of the project we would like to compare the results on the Au surface - particularly its CO oxidation rate and surface restructuring - to other metal surfaces, such as Ag(221). Specifically, we will investigate whether O atoms also self-organize into chains on these surfaces of Ag and what the diffusion rates of O atoms and surface metal atoms are in comparison to O on Au(221). Furthermore, we plan to conduct further AIMD simulations of CO on Au(221) and O₂ and CO molecules on the bimetallic AuAg(221) surface. In the latter simulations, we will arrange the Ag atoms randomly on the surface, as opposed to the previous "island" formation as depicted in Figure 5. This will provide us with further insight into the effects of surface composition on the dynamic CO oxidation mechanism.

Publications

1. S. Li, O. Olaniyan, L. Carroll, L. V. Moskaleva, M. Bäumer, *Catalytic activity of 1D chains of gold oxide on a stepped gold surface from density functional theory*, Phys. Chem. Chem. Phys., 24, 28853-28863 (2022)

Presentations

2. L. V. Moskaleva, *Computational Studies of oxidation catalysis on nanoporous gold*, Symposium of the Research Unit NAGOCAT, Soderstorf, Germany, January 9, May 30-June 1, 2022
3. L. Carroll, L. V. Moskaleva, *Computational modelling of catalysis on nanoporous gold: Self-organisation and reactivity of surface oxygen using AIMD simulations*, Psi-k 2022 Conference, Lausanne, Switzerland, August 22-25, 2022
4. L. Carroll, L. V. Moskaleva, *Investigating the self-organization of oxygen atoms on top of nanoporous gold surfaces with and without the effect of additional adsorbates*, SACI National Convention 2023, Stellenbosch, South Africa, January 9-13, 2023

6.7 **hbc00062: Adsorption of pharmaceuticals and personal care products in zeolites studied with density functional theory calculations**

HLRN Project ID:	hbc00062
Run time:	I/2022 – IV/2022 (1 st phase), I/2023 – IV/2023 (2 nd phase)
Project Leader:	Dr. Michael Fischer
Project Scientists:	Dr. Michael Fischer, Lobna Saeed, Jakob Brauer
Affiliations:	Crystallography & Geomaterials Research Group, Faculty of Geosciences, University of Bremen; Bremen Center of Computational Materials Science, University of Bremen; MAPEX Center for Materials and Processes, University of Bremen, Bibliothekstraße 1, 28359 Bremen

Overview

Electronic structure calculations in the framework of density functional theory (DFT) are used to investigate the interaction of selected pharmaceuticals and personal care products with zeolites. In one part, two species that are of particular relevance as environmental contaminants are investigated, the anticonvulsant carbamazepine and the disinfectant triclosan. Emphasis is placed on a comparison of the adsorption in different zeolite structures and on an elucidation of the dominant interactions. In addition, the adsorption of two organic UV filters (UVfs) is investigated, as it has been proposed to use zeolites as carrier materials for these functional organic molecules. These DFT calculations are carried out in close collaboration with experimental partners, who have developed zeolite-UVf composites and are investigating them with a portfolio of experimental techniques.

Scientific background

Zeolites are inorganic crystalline materials whose structures are formed by frameworks of corner-sharing TO_4 tetrahedra (where $T = Si, Al, \dots$). The presence of cavities or channels that are accessible to guest species is another distinctive feature of zeolite structures. This intrinsic porosity is pivotal for large-scale industrial applications of zeolites, which encompass catalysis, ion exchange, and the separation of gaseous or liquid mixtures. Looking beyond these established uses, they could also be employed in applications involving the adsorption of functional organic molecules. On the one hand, zeolites could be used as adsorbents for the removal of emerging organic contaminants from wastewaters. In this context, the active ingredients of pharmaceuticals and personal care products (often abbreviated PPCPs in this context) have been identified as pollutants of particular concern.[1] On the other hand, zeolites could also be used as host materials for the encapsulation of drugs or other active compounds, such as organic UVfs that are used in sunscreen lotions.

With regard to the potential use in PPCP removal, highly siliceous zeolites appear as the most promising zeolite-based adsorbents, as their hydrophobicity limits the co-adsorption of water.[2,3,4] In this project, the adsorption of two PPCP contaminants of particular concern, the anticonvulsant carbamazepine (CBZ) and the disinfectant triclosan (TCS), in different zeolites was studied using dispersion-corrected DFT calculations. DFT structure optimizations were used to predict adsorption energies and to gain insights into the structure of energetically favorable adsorption complexes. In addition, DFT-based *ab initio* molecular dynamics (AIMD) simulations were carried out for selected systems to study the influence of temperature. The role of guest-guest interactions between co-adsorbed organic molecules (for CBZ) and between the organic species and water (for TCS) was also investigated.

Further DFT calculations were employed to study the adsorption of two UVfs, octinoxate (OMC) and avobenzone (AVO), in FAU-type zeolites (zeolite framework types are usually abridged using three-letter codes [5]). This investigation is carried out in collaboration with experimental partners from the **University of Modena and Reggio Emilia, Italy** (Dr. Riccardo Fantini, Prof. Dr. Rossella Arletti) and the **University of Turin, Italy** (Prof. Dr. Lorenzo Mino). The group in Modena has recently reported the successful incorporation of OMC and AVO in different zeolites, which enhances their stability while retaining the UV absorption properties.[6] The group in Turin is responsible for the characterization of the zeolite-UVf composites using advanced vibrational spectroscopy. In this part of the project, DFT structure optimizations of adsorption complexes were followed by DFT-based predictions of the vibrational spectra.

Funding is provided through a DFG Heisenberg grant to Dr. Michael Fischer (Deutsche Forschungsgemeinschaft project no. 455871835, Fi1800/6-1). The associated PhD students are funded by the DFG (Jakob Brauer, DFG project no. 492604837) and by the Central Research Development Funds of the University of Bremen (Lobna Saeed).

Project results

For the study of CBZ adsorption, a total of eleven all-silica zeolites were considered. Since experimental observations indicate that CBZ cannot pass through smaller pore openings,[3] only frameworks having pore apertures formed by 12- or 14-membered rings of SiO₄ tetrahedra (12MRs/14MRs) were included. Despite the identical framework composition, the DFT adsorption energies showed a considerable variation from -120 to -172 kJ/mol, highlighting the important influence of pore size and pore shape. The strongest interaction was predicted for IFR, a zeolite with one-dimensional zig-zag channels where CBZ fits perfectly into the pore (Figure 1, middle panel). In some other systems, like MOR (Figure 1, right panel), the incorporation of CBZ required a significant deformation of guest molecule and framework, resulting in distinctly weaker interaction. Altogether, it was found that descriptors like the pore size are not well correlated with the affinity towards CBZ, precluding the use of such simplified descriptors for an initial identification of promising zeolites for CBZ removal. In order to study the role of guest-guest interactions, DFT optimizations were carried out for zeolite structures with two CBZ molecules adsorbed in close proximity. A significant contribution of guest-guest interactions was observed only for zeolites with relatively large pores, where the CBZ molecules can arrange in a way that attractive intermolecular interactions are maximized. Finally, AIMD simulations for CBZ in three frameworks confirmed the overall trends identified in the DFT optimizations, which do not include any thermal motion.[P1]

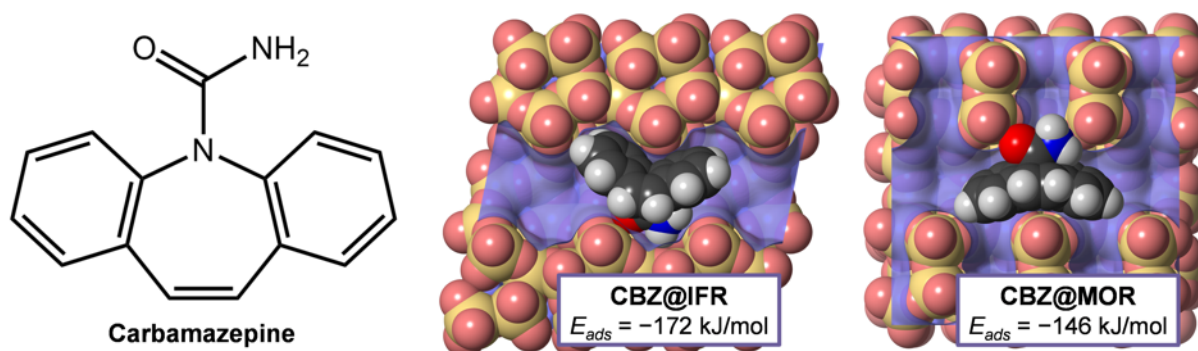


Figure 1: Left: Molecular structure of carbamazepine. Middle and right: Space-fill representation of low-energy adsorption complexes of CBZ in zeolites IFR and MOR.

The investigation of TCS adsorption considered six all-silica zeolite frameworks and two highly siliceous aluminosilicate zeolites, where extra-framework protons balance the framework charge. For the all-silica zeolites, the DFT adsorption energies for five out of six systems fell into a relatively narrow range (between -150 and -160 kJ/mol), despite differences in pore shape. This indicates that TCS, unlike the more rigid CBZ molecule, can adjust to different pore environments through rotation of the phenyl rings with respect to each other. A weaker interaction was predicted for FAU, which has much larger cages than all other zeolites. In the protonated zeolites H-FAU and H-MOR, the DFT adsorption energies were approximately 30 kJ/mol more negative than in the all-silica counterparts due to a formation of a hydrogen bond from the framework proton to the hydroxyl group of TCS. AIMD simulations confirmed the stability of these hydrogen bonds at room temperature in the absence of water. However, when co-adsorbed water molecules were included in the simulations, the interaction of water with the framework proton resulted in framework deprotonation and formation of a hydronium ion in the pores. Concurrently, the adsorbed TCS molecule moved away from the vicinity of the framework Al atom (Figure 2). These results highlight that a decrease in hydrophobicity will incur a more significant competitive adsorption of water, weakening the interaction with TCS. Altogether, it was inferred that zeolite adsorbents combining a suitable pore size (pore diameter < 10 Å) with a high hydrophobicity should be best suited to maximize TCS removal efficiency. A “fine-tuning” of the affinity through use of a zeolite adsorbent having a particular pore shape appears promising for the more rigid CBZ molecule, but not for TCS.

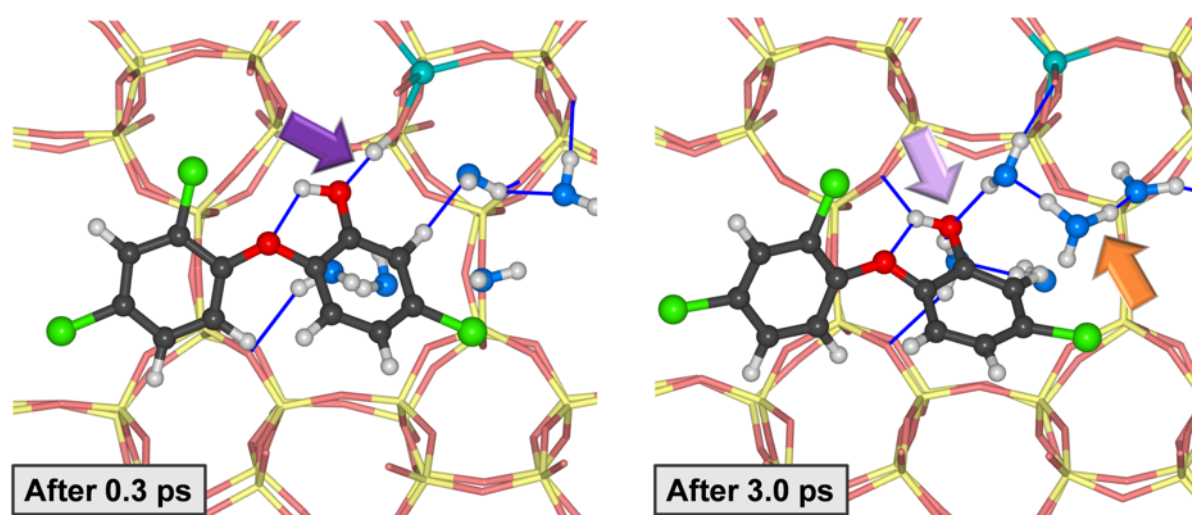


Figure 2: Snapshots from AIMD simulations of H-MOR with co-adsorbed of TCS and water. Initially, TCS is hydrogen-bonded to the zeolite framework proton (**left**, purple arrow). After a few picoseconds, TCS has moved away from its initial position (**right**, bright purple arrow) and the framework has been deprotonated by a cluster of H₂O molecules, resulting in the formation of a hydronium ion (orange arrow).

Adsorption complexes of the UVfs OMC and AVO were generated and DFT-optimized for an all-silica FAU model and for zeolite 13X, a cationic FAU-type zeolite with unit cell composition Na₉₆[Al₉₆Si₉₆O₃₈₄]. For both molecules, a much stronger interaction was predicted for 13X as compared to all-silica FAU, in line with the experimental observation of a superior efficiency of UVf incorporation in 13X.[6] This qualitative difference can be straightforwardly attributed to electrostatic interactions between oxygen atoms of the organic UVfs and the sodium cations of 13X. These also lead to some clearly detectable shifts of certain vibrational modes in the DFT-computed infrared (IR) spectra, for example, of the C=O stretching vibration of OMC. Such frequency shifts are prominently visible in experimental IR spectra of the UVf-zeolite composites.[6]

Outlook

In the second project, emphasis will be on “multi-site” interactions of pharmaceuticals and other functional organic molecules with protonated zeolites, in other words, cases where different parts of one guest molecule can interact with different framework protons. Such “multi-site” interactions could allow for a fine-tuning of the affinity that might be especially relevant for drug delivery applications. Regarding the zeolite-UVf composites, the DFT results will contribute to an interpretation of the experimentally measured IR spectra, allowing detailed insights into the interactions governing UVf adsorption. Since both UVfs can occur in different isomers (*cis/trans* isomerism of OMC, keto-enol tautomerism of AVO), which differ in their efficiency of UV absorption, a crucial point will be the identification of the dominant isomers in the adsorbed state. Further calculations are planned to study the adsorption of PPCPs at the external surfaces of clinoptilolite, a natural zeolite.

Publications

P1 M. Fischer, *Adsorption of Carbamazepine in All-Silica Zeolites Studied with Density Functional Theory Calculations*, ChemPhysChem (Early View), e202300022 (2023)

Presentations

P2 M. Fischer, *All-silica zeolites for carbamazepine removal: Predicting and analysing promising adsorbents with density functional theory calculations*, International Zeolite Conference (IZC-23), Valencia (Spain), 3rd to 8th July 2022 (*poster*)

P3 R. Fantini, G. Vezzalini, G. Confalonieri, F. Di Renzo, L. Mino, R. Cavalli, M. Argenziano, M. Fischer, R. Arletti, *Microporous Minerals Catching Sun: UV filters encapsulation in Zeolites*, Geosciences for a sustainable future - SGI-SIMP2022, Turin (Italy), 19th to 21st September 2022 (*oral*)

P4 R. Fantini, L. Mino, M. Sisti, M. Fischer, *Structural and Computational Study of Zeolite-Encapsulated UV Filters*, Workshop on Zeolites Science and Technology – Italian Zeolite Day 2022, Turin (Italy), 24th to 25th November 2022 (*poster*)

References

- [1] M. Patel et al., Chem. Rev. 119, 3510–3673 (2019)
- [2] A. Martucci et al., Microporous Mesoporous Mater. 148, 174–183 (2012)
- [3] D. J. de Ridder et al., Separ. Purif. Technol. 89, 71–77 (2012)
- [4] N. Jiang, R. Shang, S. G. J. Heijman, L. C. Rietveld, Water Res. 144, 145–161 (2018)
- [5] C. Baerlocher, L.B. McCusker, Database of Zeolite Structures (fully revised 2017); <http://www.iza-structure.org/databases>
- [6] R. Fantini et al., Microporous Mesoporous Mater. 328, 111478 (2021)

6.8 **hbi00036: Fluid Dynamics Investigation of the Stress Loading of Protein–Stabilized o/w–Interfaces in Premix Membrane Emulsification.**

HLRN Project ID:	hbi00036
Run time:	II/2021 – I/2023
Project Leader:	Prof. Dr. Udo Fritsching
Project Scientists:	A. Kyrloglou, P. Giefer
Affiliation:	Process Engineering, University of Bremen

Overview

In process engineering, dispersions, i.e. liquid/liquid systems, are widely used. Emulsions play a decisive role in the processing of food and pharmaceutical applications. Premix membrane emulsification is a process in which coarsely dispersed pre-emulsions are converted into a fine emulsion or dispersion by dispersion through a porous membrane. A key parameter of emulsion quality is droplet size distribution, which is significantly influenced by stress residence time behaviour. When incorporating shear-sensitive media, in this case proteins, the exact characterization is of relevance and requires scientific clarification.

In order to gain an accurate insight into the breakup phenomenon, the research project focuses on the description of multiphase flow in porous and idealized structures. To analyze the shear and elongation forces at the phase interfaces, a model was developed and implemented in the open-source software OpenFOAM. Since the proteins involved in the process adsorb at the phase boundaries, this is of particular interest. The aim of the project is to quantify the criteria for droplet deformation and breakup based on these stresses.

Such protein stabilised solutions have been observed to exhibit non-Newtonian behaviour when under stress. Ergo, understanding the non-Newtonian fluid behaviour, i.e., the adapting of a fluid's viscosity based on the exerted on it stress, is a critical factor in obtaining the required product emulsion.

Along with process parameters, such as the flow rate, the physical properties of the fluids as well as those of the membrane itself play a significant role in membrane emulsification. Membrane parameters such as the porosity and pore size distribution, in addition to surface wettability and/or charge, directly affect the stresses arising within the emulsification process and therefore can alter the behaviour and resulting emulsion droplet size distribution of industry relevant fluids.

The aims of this project are to develop a method and the tools going with it to accurately predict the pressure drop as well as the droplet size distribution of membrane produced emulsions of Newtonian as well as non-Newtonian fluids.

Results

Idealised Porous System

The idealised case chosen as a simplified model to a real complex membrane structure was the multipore geometry as depicted in Figure 1a. This geometry consists of multiple equally sized channels connecting the inlet and the outlet chambers allowing the flow to develop around a droplet moving towards the central pore and prevent any suction effects making the Laplace pressure the characteristic factor for droplet breakthrough.

As illustrated by Figure 1b, four distinct breakthrough regimes were identified, namely no breakthrough, i.e., the droplet clogging the pore, partial breakthrough, i.e., again clogging of the pore but with part of the droplet detaching and entering the pore, polymer breakthrough, i.e., the droplet entering and dispersing through the pore, and water breakthrough, i.e., once again initial clogging of the pore but with the inlet flow applying sufficient pressure to create a fingering instability through the droplet for the continuous water phase to pierce through it.

These regimes were then mapped for multiple simulations on a phase diagram as seen in Figure 1c based on the Weber and Weissenberg dimensionless numbers, by varying the simulation's inlet velocity and the droplet's physical properties and more specifically the viscoelastic relaxation time. It can be observed that for the highly viscoelastic droplets the polymer breakthrough regime was always reached. On the other hand, for less viscoelastic droplets the other three regimes are prominent based on the inlet chamber's pressure controlled by the variation in the inlet velocity. Starting at low velocities the no breakthrough regime is most prominent, moving to the partial breakthrough regime as the velocity increases, and finally reaching the water breakthrough regime at higher velocities.

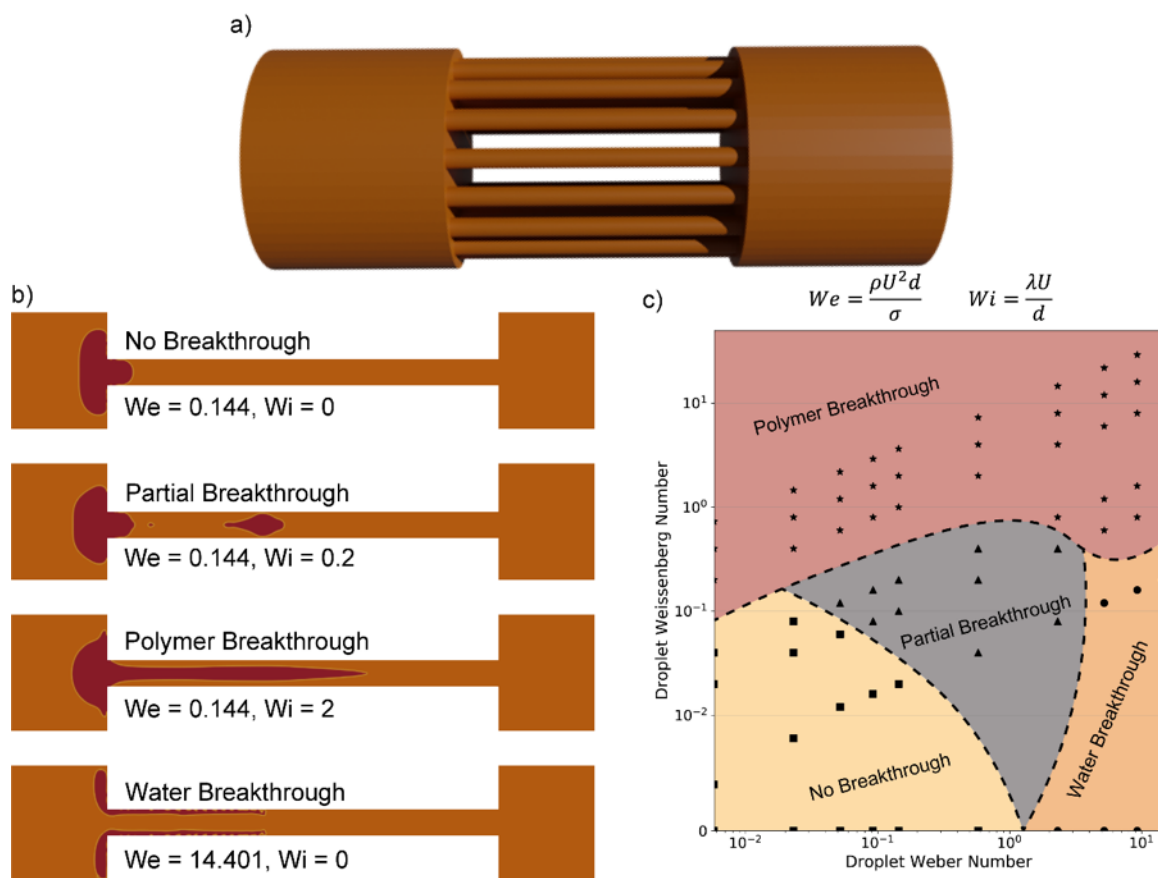


Figure 1: a) The 3D multipore simulation domain used for studying single droplet dispersion behaviour in an idealised porous environment, b) The four observed breakthrough regimes for a highly viscous droplet of varying viscoelasticity, c) The Weissenberg vs Weber number phase diagram of the four breakthrough regimes identified.

Complex Real Membrane System

Moving from the ideal system to the real complex membrane was first done for a simplified Newtonian system to assess the droplet dispersion behaviour based on activity, i.e., by varying the membrane static contact angle. Figure 2a depicts the simulation domain showing an inlet chamber where the initial drop was instantiated, the meshed complex membrane structure, and finally a long outlet chamber for the produced droplets to evolve in.

Keeping the pressure drop through the membrane constant, we observed that at small contact angles as in Figure 2bi the membrane shows a high affinity for liquid/liquid filtration with a large part of the initial droplet trapped inside or coalescing at the membrane exit. At larger contact angles as in Figure 2bii the membrane shows a higher affinity for emulsification resulting in the production of a droplet size distribution in the outlet chamber.

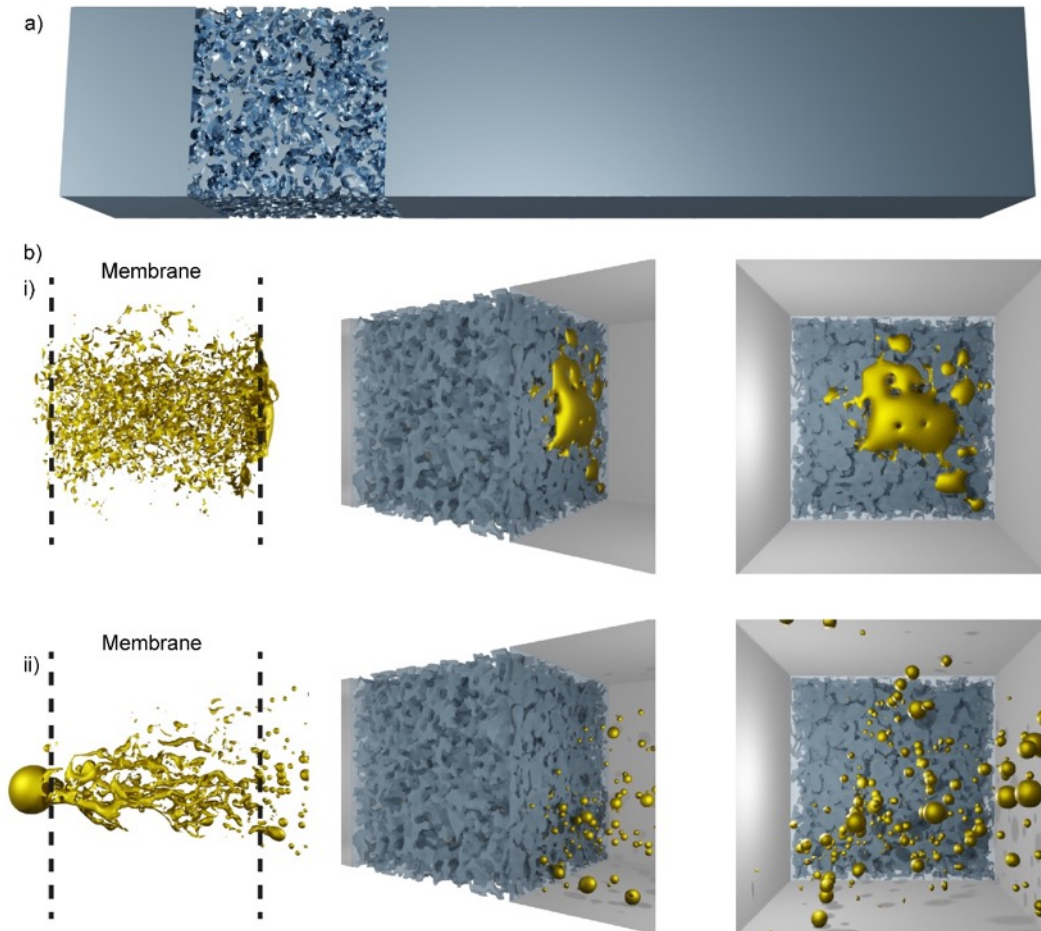


Figure 2: a) The 3D membrane simulation domain constructed from a μ CT scanned P2 Robuglas membrane structure used for studying single droplet dispersion behaviour in a real porous environment, b) Illustrative simulation snapshots, from left to right: side view showing the droplet dispersion within the membrane structure, perspective and front views showing the membrane outlet for i) a hydrophobic and ii) a hydrophilic membrane.

Outlook

For the last part of the project that is still underway simulations of the same membrane system with viscoelasticity will be performed and the results compared to actual experimental data from our lab using the premix emulsification process. Preliminary experiments have shown that with increased viscoelasticity the obtained droplet size distribution shifts to smaller sizes and we plan to study and quantify this effect in more detail.

Publications

1. Wollborn, T., Luhede, L., & Fritsching, U. (2019). Evaluating interfacial shear and strain stress during droplet deformation in micro-pores. *Physics of Fluids*, 31(1), 012109.
2. Wollborn, T., et al. (2021) Investigation of local and temporal interfacial shear stress distribution during membrane emulsification. *Can. J. Chem. Eng.*

Presentations

3. A. Kyrloglou, U. Fritsching, Dispersion of Viscoelastic Fluids in Porous Structures: An Experimental and Computational Investigation, ECCOMAS, 2022, Oslo, Norway (Oral Presentation)
4. A. Kyrloglou, U. Fritsching, The Dispersion Behaviour of Viscoelastic Fluids in Porous Structures, ProcessNET MPH, 2022, Online (Poster)
5. A. Kyrloglou, U. Fritsching, The Dispersion Behaviour of Viscoelastic Fluids in Porous Structures, MMPE, 2022, Berlin, Germany (Poster)

6.9 **hbi00037: Molekulardynamische Untersuchung der Stressbeanspruchungen auf Proteine an der Phasengrenzfläche beim Premix-Membranemulgieren**

HLRN-Projektkenung:	hbi00037
Laufzeit:	I/2019 – II/2022
Projektleiter:	Prof. Dr.-Ing. habil. Udo Fritsching
Projektbearbeiter:	Patrick Giefer, M.Sc.
Institut / Einrichtung:	Fachgebiet Mechanische Verfahrenstechnik, Universität Bremen

Überblick

Emulgierverfahren werden im Rahmen des Downstream-Prozessierens und der Weiterverarbeitung/Formulierung zur Homogenisierung oder auch Verkapselung in biogenen Produkten eingesetzt. Beim Premix-Emulgieren wird eine grobdisperse Voremulsion mittels der Dispergierung in porösen Membranen in eine Feinemulsion bzw. -dispersion überführt. Insbesondere das Stress-Verweilzeitverhalten und die darauf erfolgende Reaktion eines protein-stabilisierten dispersen Systems bedarf einer vertieften wissenschaftlichen Klärung. Hieraus können mechanistische Schädigungsmodelle abgeleitet werden. Die im Emulgierprozess auftretenden mikromechanischen Belastungen auf biologische Systeme sind nicht vollständig geklärt, die Prozessumgebung ist somit noch weiter zu entwickeln im Hinblick auf die Anpassung an spezielle biologische Systeme. Um den Einfluss des Premix-Emulgierverfahrens und der dabei auftretenden Stress-Verweilzeit-Belastungen auf die agglomerierten Proteine (hier Beta-Lactoglobulin) im Fluid und an den Phasengrenzflächen zu untersuchen, werden numerische Untersuchungen auf molekular-dynamischer Ebene an Proteinstrukturen durchgeführt. Diese Untersuchungen zeigen, inwieweit die Proteinstrukturen durch den Emulgiervorgang belastet und geschädigt werden können, beziehungsweise ob eine proteinschonendere Emulgierung mit den Membranen möglich ist.

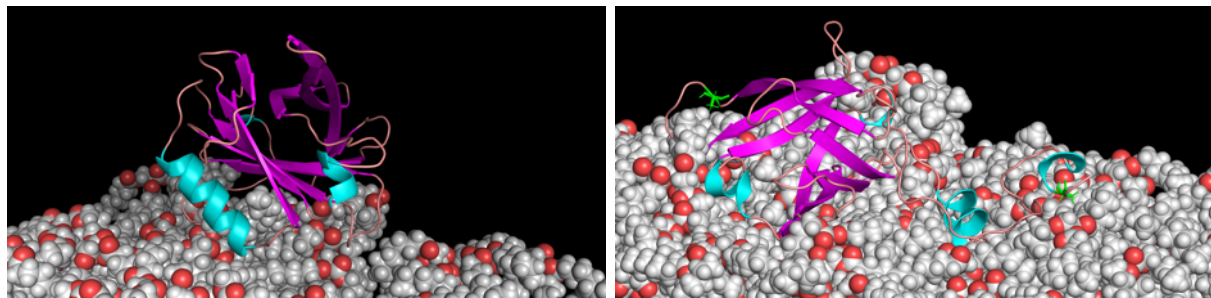
Das Projekt ist in dem DFG geförderten Schwerpunktprogramm 1934 „DISPBiotech“ eingebunden. Der Förderungszeitraum der zweiten Förderperiode beträgt 36 Monate

Ergebnisse

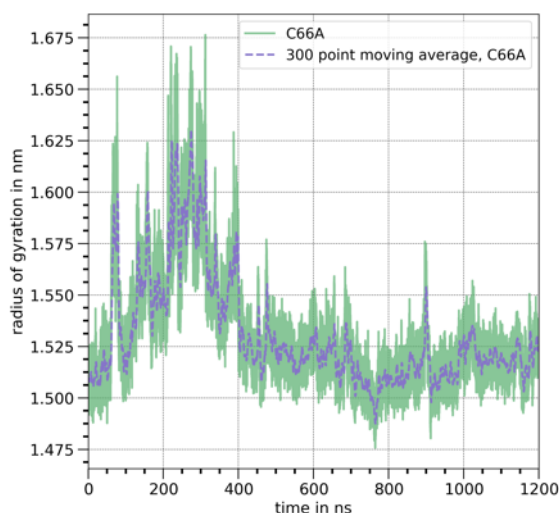
Zielsetzung des vorhergegangenen Projektzeitraumes war die Untersuchung von nativem und rekombinanten Beta Lactoglobulin an Öl/Wasser-Grenzflächen, zur Quantifizierung des Einflusses der rekombinanten Variante auf die Fähigkeit der Emulsionsstabilisierung. Dazu wurden zunächst Strukturen des nativen Proteins mutiert, um der Struktur der rekombinanten Variante zu entsprechen. Die rekombinante Variante wird von dem Bakterium E-coli synthetisiert und unterscheidet sich in der Ausbildung der Disulphidbrücken. Dabei bezeichnet „C66A“ eine Mutante, bei der das Cystein an der Stelle 66 durch ein Alanin ausgetauscht wurde und eine Disulphidbrücke zwischen den Cysteinen 106 und 119 besteht. Die Mutante „noCys“ besitzt keine Cysteine und ist folglich ohne Disulphidbrücken. Weiter wurde die Adsorption von Beta Lactoglobulin an der Silica/Wasser-Grenzfläche untersucht, da sich in Experimenten gezeigt hat, dass Proteine an die Membran adsorbieren.

In Abbildung 1 ist die Adsorptionskonfiguration der Mutante C66A (A) und noCys (B) an der Öl/Wasser-Grenzfläche dargestellt. Den Abbildungen ist zu entnehmen, dass sich die Adsorptionskonfiguration unterscheidet. Während die Mutante C66A in globulärer Struktur an der Grenzfläche adsorbiert, ist bei der Mutante ohne Cysteine eine entfaltete Konformation vorhanden. Zur Quantifizierung des unterschiedlichen Entfaltungsgrades ist in Abbildung 1C-

D der Streumasseradius aufgetragen. Während die Variante C66A mit einer Disulphidbrücke nach ungefähr 600 ns eine stabile Adsorptionskonfiguration erreicht, entfaltet sich die Mutante ohne Disulphidbrücke noch an der Grenzfläche. Der Entfaltungsgrad zum Ende der jeweiligen Simulation liegt für die Mutante C66A zwischen 1.50 nm und 1.53 nm, während der Entfaltungsgrad für die Mutante noCys zwischen 1.8 nm und 2.1 nm liegt. Daraus lässt sich schließen, dass die Disulphidbrücke zwischen den Cysteinen 106 und 119 einen erheblichen Anteil in der Erhaltung der globulären Struktur bei der Grenzflächenadsorption hat. Der höhere Entfaltungsgrad der Variante noCys an der Grenzfläche lässt auf eine erhöhte Grenzflächenstabilisierung schließen, die experimentell durch eine stärkere Herabsetzung der Grenzflächenspannung im Vergleich zur Variante C66A bestätigt wurde.



C)



D)

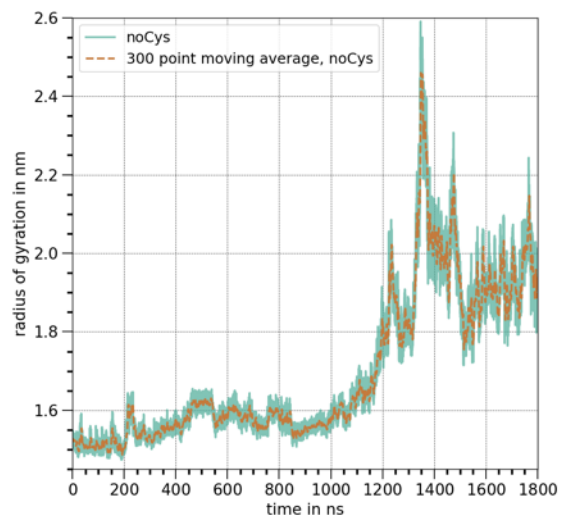


Abbildung 1: Snapshot aus MD-simulationen, A) C66a (1.2 μ s) und B) noCys (1.8 μ s) adsorbiert an MCT-Öl/Wasser-Grenzfläche, die Residuen 66 und 106 sind in grün hervorgehoben, C) radius of gyration der Mutante C66A, D) radius of gyration der Mutante noCys.

Den Simulationsergebnissen der Adsorption von nativem Beta Lactoglobulin an der Silica/Wasser-Grenzfläche ist zu entnehmen, dass die Adsorption des Proteins auf elektrostatische Wechselwirkungen zwischen dem Protein und der Oberfläche zurückgeführt werden kann, wie in Abbildung 2 dargestellt. Da die Silica Grenzfläche bei pH 7 vorwiegend negativ geladen ist, adsorbiert das Protein mit den übrigen positiv geladenen Resten (blau) an der Grenzfläche. Die negativ geladene Seite des Proteins (rot) ist von der Grenzfläche abgewandt und befindet sich parallel und senkrecht zur Grenzfläche. Die Adsorption erfolgt nach etwa 120 ns. Der Abbildung 3A ist zu entnehmen, dass die, bei pH 7, positiv geladenen Kontaktresiduen, LYS8, LYS14 und LYS100, identifiziert werden können. In der Abbildung sind die Residuen über die Zeit aufgetragen, die in einen Abstand zur Grenzfläche stehen, in dem sie Wasserstoffbrücken zur Grenzfläche ausbilden können. Dazu wird für jede

Nanosekunde, in der sich das Residuum in einem Abstand von 0.18 nm befindet, ein vertikaler Strich aufgetragen. Dadurch lassen sich konstante und frequente Bindungen quantifizieren. Bei einem pH-Wert von 7 ist Lysin protoniert und daher positiv geladen, was auf einen pKa-Wert von 10,5 zurückzuführen ist. Darüber hinaus weist der nicht geladene hydrophobe Rest TYR99 einen signifikanten Kontakt mit der Grenzfläche auf. Aufgrund seiner neutralen Ladung kann die Nähe zur Oberfläche durch den benachbarten Bindungsrest LYS100 erklärt werden.

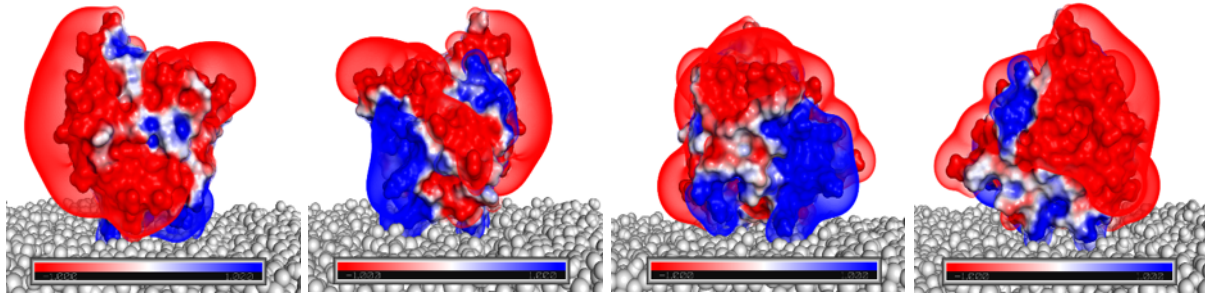
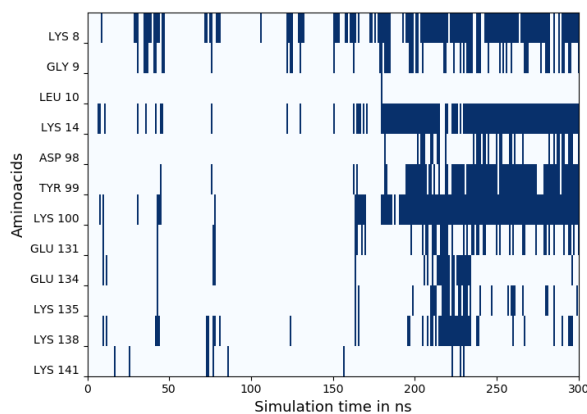


Abbildung 2: Elektrostatische Potential Oberfläche von -1 eV (red) bis 1 eV (blue) von β -Ig an Silica/Wasser Grenzfläche betrachtet aus vier verschiedenen Richtungen, die Silica Grenzfläche ist in grau representiert.

In der Abbildung 3B ist die Solvent Accessible Surface (SAS) für hydrophile und hydrophobe Residuen dargestellt. Nach der Adsorption an der Silica/Wasser-Grenzfläche bei etwa 120 ns ist eine Freilegung der hydrophoben Residuen zu beobachten. Diese Ergebnisse unterstreichen, dass die Adsorption durch elektrostatische Wechselwirkungen angetrieben und dann durch hydrophobe Wechselwirkungen stabilisiert wird, die während der Adsorption freigelegt werden.

Dank der Bereitstellung der Ressourcen durch das HLRN konnte ein molekulares Verständnis der Proteinadsorption innerhalb des Premix-Membranemulgierens geschaffen werden, was zur Prozessoptimierung beiträgt.

B)



A)

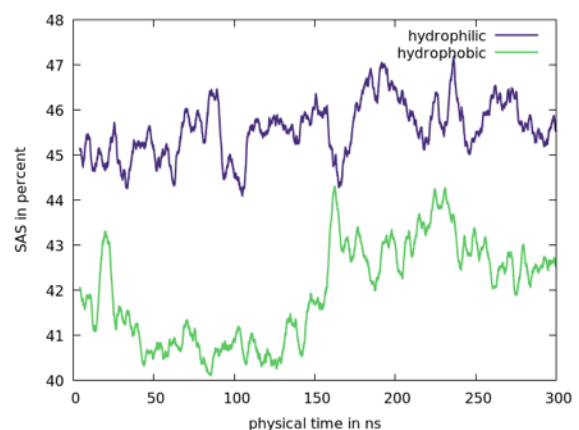


Abbildung 3: natives Beta-lactoglobulin an Silica/Wasser-Grenzfläche, A) Kontaktresiduen über die Zeit, B) hydrophile und hydrophobe Solvent Accessible Surface (SAS) über Zeit.

Publikationen

1. P. Giefer, S. Bäther, H. Kieserling, A. Heyse, N. Kaufmes, W. Wagemans, L. Barthel, V. Mayer, E. Schneck, S. Drusch, U. Fritsching, and A. M. Wagemans, „Characterization of β -lactoglobulin adsorption on silicate surfaces as used in the premix-membrane-emulsification process,” *under review*

Vortrag

2. P. Giefer, U. Fritsching, „An Atomistic View On Protein Adsorption to Interfaces and the Importance of Wettability on Drop Break-up in a Capillary Confinement from a fluid-dynamic perspective“, MMS Days Potsdam, April 2022

6.10 *hbi00042*: Drag reduction by air retaining surfaces – Long holes

HLRN Project ID:	hbi0042
Run time:	III/2018 – II/2022
Project Leader:	Prof. Dr. Albert Baars
Project Scientists:	Christoph Wilms, Daniel Matz
Affiliation:	City University of Applied Sciences Bremen

Overview

The reduction of hydrodynamic frictional drag in the case of ship hulls or flows of liquids in pipes/channels can contribute to diminish energy demand and CO₂ emissions. Inspired by the water fern *Salvinia molesta*, the effect of air retaining surface structures on drag reduction has been investigated for fully developed turbulent channel flow. Due to the lower dynamic viscosity of gases in comparison to liquids at equal thermodynamical conditions, (factor of around 1/50 for air/water at ambient conditions) an air layer between wall and liquid leads to a reduction of frictional drag in comparison to the standard case of pure liquid. To avoid the entrainment of air, superhydrophobic surface structures are applied. Due to the direct contact between liquid and parts of the surface structure, the drag reduction is diminished in comparison to a pure gas layer. In this context, the geometry and the size of the structure are crucial for drag reduction. At a friction Reynolds number of $Re_\tau = 180$, the effect of surface structures in form of pillars, long holes and grooves (the latter two oriented in streamwise direction) on frictional drag has been compared using direct numerical simulations. At equal widths for pillars and long holes, an increase of drag reduction with length of long holes can be observed which converges to the value of grooves.

Material and Methods

The surface structures are modelled by a plane with slip (gas/liquid interface) and no-slip (liquid/structure interface) boundary conditions and are applied on two oppositely oriented walls of a channel (height $2h$, length $2\pi h$, width πh). All investigated structures feature the same ratio slip to the total surface of the structure of 0.75. The pillars are of squared shape with periodic lengths in streamwise and spanwise direction of $W^+ = L^+ = 10, 20, 40, 80$ (in wall units). For long holes, the periodic length in streamwise direction is equal to $W^+ = 80, 160, 320, 640$ and in spanwise direction $L^+ = 20$. The third structure are grooves oriented in streamwise direction with a width of $L^+ = 20$. The conditions of the channel boundaries in streamwise and spanwise directions are cyclic. The friction Reynolds number $Re_\tau = u_\tau h/\nu = 180$ is calculated from the half channel height h , the friction velocity u_τ , and the kinematic viscosity ν . The spatial resolution in wall normal direction amounts to $y_1^+ < 0.04$ at the wall and $\Delta y_c^+ \approx 4$ at the centre of the channel. In stream- and spanwise direction, the resolution of long holes is $\Delta x^+ = \Delta z^+ \approx 0.5$ and of pillars between $\Delta x^+ = \Delta z^+ \approx 0.7$ ($L^+ = 10$) and $\Delta x^+ = \Delta z^+ \approx 2.6$ ($L^+ = 80$). The continuity and momentum equation for constant fluid properties are solved using the spectral element code Nek5000 (Fischer et al. 2017) with 3rd-order temporal and 5th (pressure) / 7th (velocity) order spatial discretisation scheme. The drag reduction DR is calculated from the bulk velocity (spatially and temporally averaged velocity in streamwise direction) for the standard case (wall with no-slip boundary condition) u_{b0} and the case with surface structured walls u_b

$$DR = 1 - \left(\frac{u_{b0}}{u_b}\right)^2.$$

Results

In Figure 1, the drag reduction DR is plotted versus the structure size L^+ . For pillars, an almost linear increase of DR can be observed up to $L^+ = 20$. From $L^+ = 20$ up to $L^+ = 80$ a less steep rise appears. In the case of long holes, an under-proportional growth of DR with the length of the holes W^+ appears. The progression of DR seems to converge towards the value of grooves. For the maximal chosen values of W^+ and L^+ in this study a nearly equal drag reduction occurs.

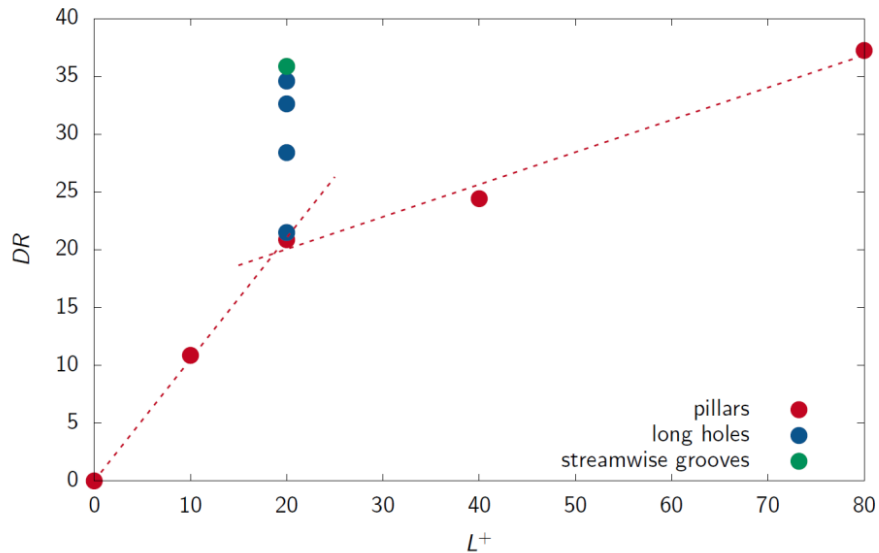


Figure 1: Drag reduction DR due to structured walls (reference, pillars, long holes, grooves) in fully developed turbulent channel flow plotted versus structure size in spanwise direction L^+ . In case of long holes drag reductions increases with W/L .

A more detailed insight to this behaviour can be gained from the averaged velocity u^+ plotted versus wall normal distance y^+ , both in wall units (Figure 2).

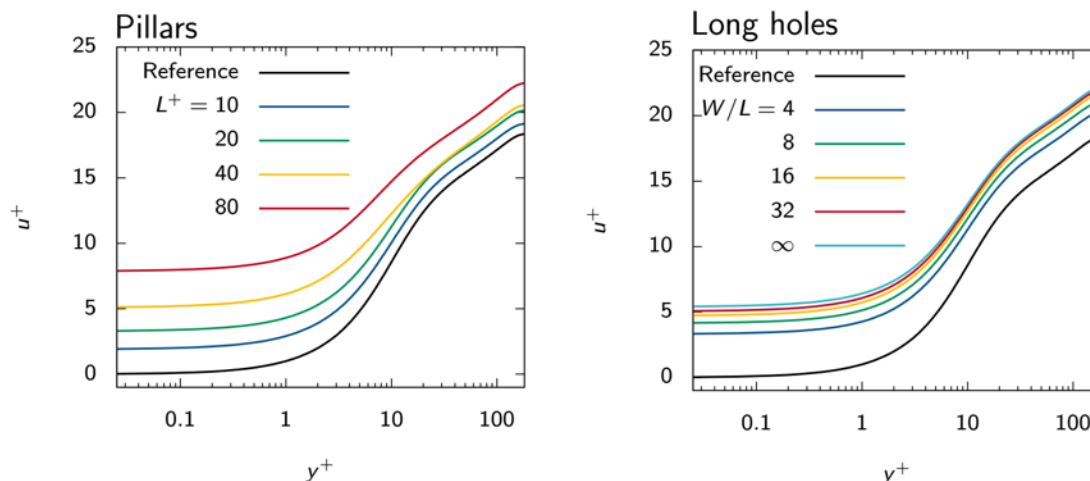


Figure 2: Averaged velocity in streamwise direction u^+ plotted versus wall normal coordinate y^+ in wall units for fully developed turbulent channel, different structure geometries and sizes. $W/L = \infty$ symbolises grooves in streamwise direction.

On the left-hand side, the profiles for pillars are shown. With growing L^+ the slip velocity at the surface ($y^+ = 0$) rises. This leads to an increase in bulk velocity and drag reduction. The change in inclination of DR with L^+ (Figure 1) can be recognised in the progression of the slip velocity with L^+ . The upward shift of the velocity profile due to the slip velocity is not fully transferred to all parts of the profile. Deviations to the reference appear in the buffer layer, which get more apparent by a downward shift of the velocity profile in the logarithmic and defect domain. This downward shift increases with L^+ , diminishes the bulk velocity, and the drag reduction. On the right-hand side of Figure 2, the velocity profiles for long holes and grooves are depicted. In general, a similar behaviour is observed for pillars. An obvious difference is the smaller downward shift with growing W^+ in comparison to L^+ , while the investigated range of W^+ is higher in comparison to L^+ .

In general, the influence of the structure size on drag reduction, the velocity profile including slip velocity at the wall and downward shift in the buffer layer is known, see Seo and Mani (2016) and Fairhall et al. (2019). An interesting aspect of this investigation is the anisotropic surface structure of long holes. With increasing W^+ , the frequency a near wall fluid element is decelerated by parts of the surface structure oriented in spanwise direction diminishes. This explains the increase in slip velocity and drag reduction with W^+ . The downward shift of the velocity profile with L^+ results from a rise in turbulent momentum transfer in the near wall region. The weaker influence of W^+ on turbulence in comparison to L^+ may be explained by the interaction of turbulent flow structures such as rolls with the structured wall. Due to the orientation of rolls with a main axis in streamwise direction, a constant L^+ and a rise in W^+ may less affect (a) the distance between rolls and the surface, (b) the turbulent momentum transport towards the wall, and (c) the downward shift of the velocity profile. This is supported by the profiles of the spanwise component $w'w'^+$ of the Reynolds stress tensor (Figure 3). With growing L^+ , $w'w'^+$ rises in the nearer wall region (pillars). For holes at constant L^+ , an increase in W^+ leads to a much smaller rise in $w'w'^+$. The relevant parameter for the downward shift seems to be the width L^+ of the structure.

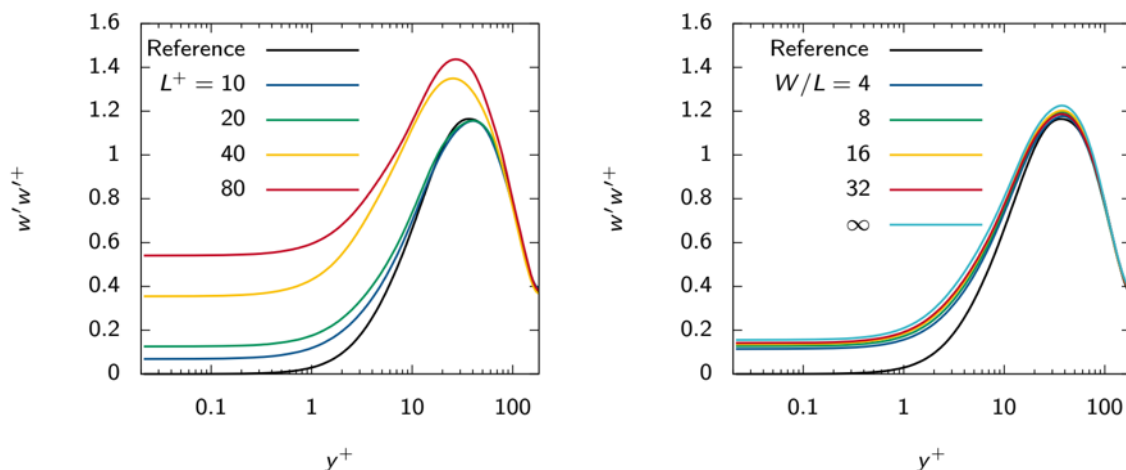


Figure 3: Spanwise component from Reynolds stress tensor $w'w'^+$ plotted versus wall normal coordinate y^+ in wall units for pillars (left), long holes and grooves (right)

Outlook

The chosen friction Reynolds number of 180 is the lower limit for a fully developed turbulent channel flow that remains turbulent. For such low Re_τ , the appearance of a proper logarithmic domain is questionable. Simulation should be carried out at least with $Re_\tau = 395$. The gas/liquid interface has been assumed to be a plane concise with the upper tips of the structure. A two-phase flow approach would consider the deflection of the interface and

possible air losses. Both suggestions are linked to an extensive rise in computation power in comparison to the described simulations.

Literature

1. Fairhall CT, Abderrahaman-Elena N, García-Mayoral R (2018) The effect of slip and surface texture on turbulence over superhydrophobic surfaces. *J. Fluid Mech.* 861, 88–118
2. Fischer PF, Lottes JW and Kerkemeier SG (2017) Nek5000 Version 17.
Available: <https://nek5000.mcs.anl.gov>, Argonne National Laboratory, Illinois
3. Seo J, Mani A (2016) On the scaling of the slip velocity in turbulent flows over superhydrophobic surfaces. *Physics of Fluids* 28, 025110

Presentations

4. Baars, A, Wilms C, Matz D, Kacwin A, Kesel AB (2022) Air Retaining Surface Structure of *Salvinia molesta* – Physics, Applications and Challenges. Annual Conference Society of Experimental Biology, 08.07.2022, Montpellier
5. Wilms, C, Matz D, Kesel A, Baars A (2022) Superhydrophobic surfaces: drag reduction of wall bounded turbulent flow. 14th European Fluid Mechanics Conference, 19.09.2022, Athens

The AIRCOAT project has received funding from the European Union's Horizon 2020 research and innovation programme under grant agreement N° 764553



6.11 *hbi00053*: Turbulent puff dynamics in pulsatile pipe flow

HLRN Project ID:	hbi00053
Run time:	IV/2021 – III/2022
Project Leader:	Prof. Dr. M. Avila
Project Scientists:	Daniel Morón Montesdeoca
Affiliation:	ZARM, University of Bremen

Overview

Pulsatile pipe flow, pipe flow whose bulk velocity has a mean and one or more oscillatory components, is ubiquitous in industrial and biological applications. The presence of turbulence in pulsatile pipe flow is related with undesired energy losses [1], and even with cardiovascular diseases in our vessels, [2, 3]. Therefore, it is of high interest to understand how turbulence arises and behaves in this type of flows, and how it depends on the flow dimensionless parameters. These are the Reynolds number (Re), which compares the inertia and viscous forces; the Womersley number (Wo) that represents a non-dimensional frequency of the pulsation; and the waveform of the pulsation. Depending on the three, turbulence can either spread, localize or even decay after forming. While the effect of Re and Wo on turbulence have been systematically studied [4], the effects of the waveform remain largely unexplored.

In this project, we study the effect of the waveform on turbulence transition and sustenance. We restrict our analysis to $Re=2000$ and $Wo=11$, values for which turbulence appears in the form of localized patches, called puffs. Independently of the shape of the pulsation, puffs at this Re and Wo are expected to decay in a stochastic way. We perform ensembles of direct numerical simulations of pulsatile pipe flows driven with different waveforms, and identify the features of the waveform that enhance turbulence transition and survival.

Methods

We consider a Newtonian fluid with constant properties confined in a cylindrical pipe. The fluid is driven in the axial direction at a time periodic bulk velocity. The flow is assumed to be incompressible, and governed by the incompressible Navier–Stokes equations (NSE). We numerically integrate the NSE using our pseudo-spectral code **nsPipe** [5]. The code discretises the problem in cylindrical coordinates and considers periodic boundary conditions in the azimuthal and axial directions, and zero velocity (no-slip boundary conditions) at the wall. At each time step the code adapts the bulk velocity of the flow so it follows the desired waveform.

We perform direct numerical simulations of pulsatile pipe flows driven with 8 different bulk velocities. The shape of the bulk velocities is controlled by 3 parameters (see Figure 1). All the bulk velocities have an acceleration phase (AC), where the bulk velocity increases and whose slope is set by t_{ac} . After the acceleration they reach a plateau of high velocities, whose duration is set by t_m . Then the bulk velocity decelerates (DC) at a rate set by the slope t_{dc} and reach a plateau of zero bulk velocity. See the definition of our bulk velocities in Table 1, and an example in Figure 1. For each bulk velocity we perform 10 simulations with different initial turbulent puffs, making a total of 80 simulations. We then gather statistics of the time evolution of turbulence fraction in the pipe F_{turb} . Note that $F_{turb}=1$ means a pipe filled with turbulence, and $F_{turb}=0$ a fully laminar flow. We run the cases for at least 20 pulsation periods (T), initialized with a localized turbulent structure. We stop the simulations as soon as a case relaminarizes, $F_{turb}=0$, or reaches the hard limit of 20 pulsation periods.

Results

According to our simulations the waveform parameters, and therefore the shape of the waveform have an effect on turbulence decay. In Figure 2 we show the turbulent fraction for all the different waveforms we consider. For large t_m only 13 out of 40 cases remain turbulent for the full 20 periods, whereas 16 out of 40 cases remain turbulent when t_m is small. Regarding the other two parameters, for large t_{dc} 17 out of 40 cases remain turbulent for the full 20 periods, whereas 12 out of 40 cases remain turbulent when t_{dc} is small. For large t_{ac} 20 out of 40 cases remain turbulent for the full 20 periods, whereas 9 out of 40 cases remain turbulent when t_{ac} is small. In short, pulsatile flows that have steeper acceleration and deceleration phases (small t_{ac} and t_{dc}), and have shorter phases of the period with low (nearly zero) bulk velocity (smaller t_m) tend to relaminarise earlier than other pulsatile pipe flows.

We also study turbulence transition, and its dependency on the pulsation waveform. Opposite to turbulence survival, pulsations with milder deceleration and with longer phases of the period with 0 bulk velocity, are more susceptible to turbulence transition. Our results suggest that, a waveform that enhances transition does not need to also delay turbulence decay.

The results of this project been published in the leading international journal of the field, the Journal of Fluid Mechanics [P1].

Outlook

It is our objective to continue this line of work and study the effects viscoelasticity and flexible walls have on turbulence transition and survival in pulsatile flows. The final goal of the project is to describe turbulence transition in cardiovascular flows by considering the combined effect of all its complex features.

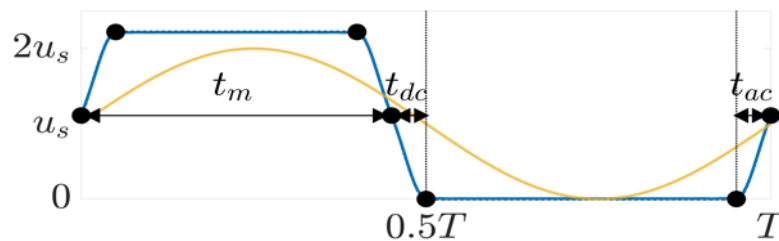


Figure 1: Definition of the waveform using 3 parameters: t_m , t_{ac} , t_{dc} . In blue WF1 of table 1, in yellow a sine wave pulsation. The units of the plot are normalized with the pulsation period T and mean bulk velocity u_s .

	WF1	WF2	WF3	WF4	WF5	WF6	WF7	WF8
t_m	0.45	0.45	0.45	0.45	0.55	0.55	0.55	0.55
t_{ac}	0.05	0.05	0.2	0.2	0.05	0.05	0.2	0.2
t_{dc}	0.05	0.2	0.05	0.2	0.05	0.2	0.05	0.2

Table 1: Definition of the 8 waveforms used in this study.

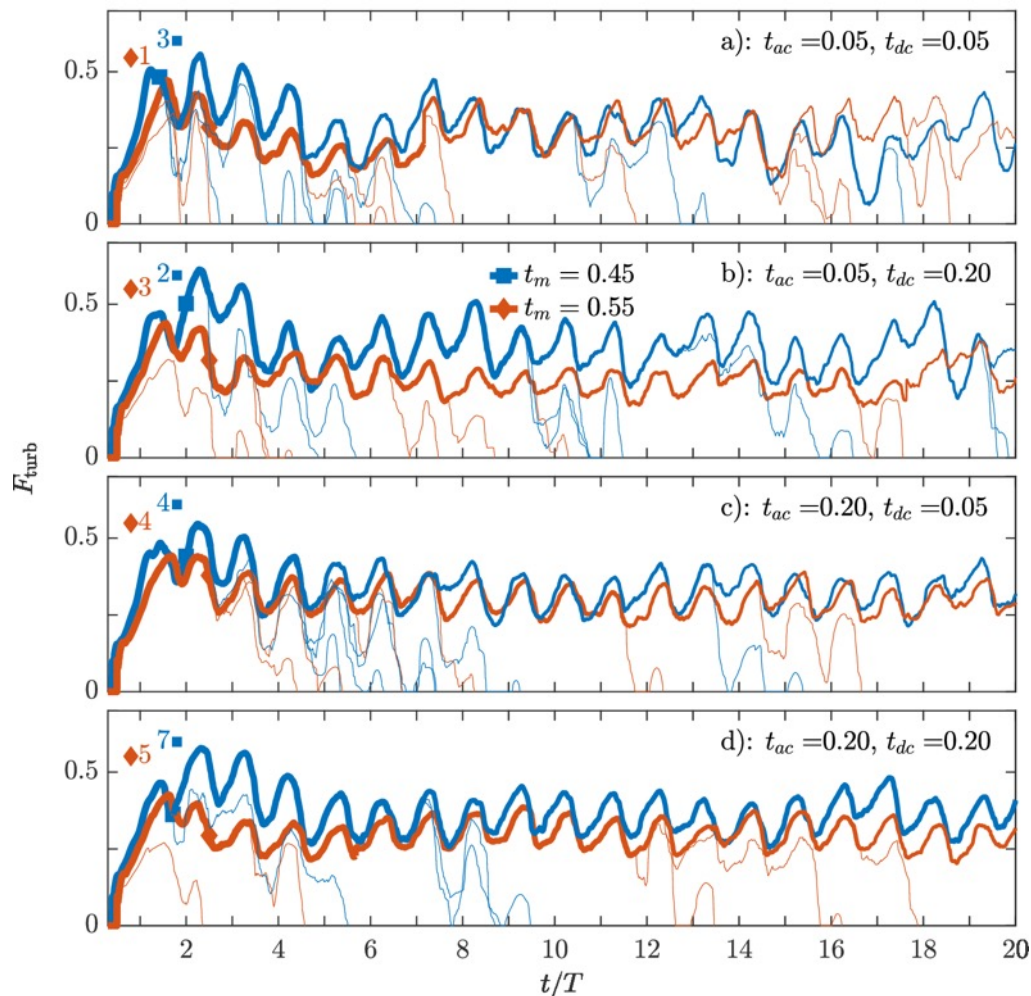


Figure 2: Turbulent fraction in all our 80 DNS with respect to time. In panels find the cases with the same pair of t_{ac} , t_{dc} . The colors and symbols of the lines denote different t_m . In each panel, and for each t_m we show in a thick line the instantaneous mean turbulent fraction of the cases that have not yet relaminarised. The thickness of the mean turbulent fraction decreases whenever one of the 10 cases relaminarises. With numbers in the top left corner we denote the number of cases where turbulence is sustained for $t > 20T$.

Related Publications

P1. D. Morón, D. Feldmann, and M. Avila, “Effect of waveform on turbulence transition in pulsatile pipe flow”. *Journal of Fluid Mechanics*, 948, A20, 2022

References

1. T. Gebreegziabher, E. Sparrow, J. Abraham, E. Ayorinde, and T. Singh, “High-frequency pulsatile pipe flows encompassing all flow regimes,” *Numerical Heat Transfer, vol. Part A: Applications*, pp. 811–826, 11, 2011.
2. J. Golledge and P. E. Norman, “Atherosclerosis and abdominal aortic aneurysm: cause, response, or common risk factors?,” *Arterioscler Thromb Vasc Biol.*, 30(6):1075-1077, 2010.
3. K. S. Cunningham and A. I. Gotlieb, “The role of shear stress in the pathogenesis of atherosclerosis,” *Laboratory investigation*, vol. 85, no. 1, pp. 9–23, 2005.
4. D. Xu and M. Avila, “The effect of pulsation frequency on transition in pulsatile pipe flow, *Journal of Fluid Mechanics*”, 857, 937-951, 2018
5. J. M. López, D. Feldmann, M. Rampp, A. Vela-Martín, L. Shi, and M. Avila, “nsCouette a high-performance code for direct numerical simulations of turbulent taylorcouette flow,” *SoftwareX*, vol. 11, p. 100395, 2020

6.12 *hbi00055*: Validation and parametrisation of turbulence and transport models used in computational fluid dynamic studies of aerosol transport in indoor environments

HLRN Project ID:	hbi00055
Run time:	II/2022–I/2023
Project Leader:	Daniel Feldmann
Project Scientists:	Christoph Kühn
Affiliation:	Universität Bremen, Center of Applied Space Technology and Microgravity (ZARM), Am Fallturm 2, 28203 Bremen, Germany

Motivation and starting point

There is compelling evidence that transmission of SARS-CoV-2 occurs predominantly in indoor environments [1, 2] and that airborne transmission is a significant route of infection [3]. While respiratory droplets can be subject to strong evaporation under some conditions [4] and quickly settle to the ground within typically a two meters radius [5, 6], aerosol particles can remain airborne up to hours [7]. Their transport, can be augmented for example by air-conditioned ventilation and directly result in airborne transmission from person to person [8]. Also important for airborne virus transmission is the accumulation of aerosols in particular regions of a closed air space shared with others. An infectious dose might build up over typical meeting times (~ 90 min) in distances much larger than 2 m away from infected individuals, even though larger droplets have quickly settled to the ground [4]. In such scenarios, not only short-range dynamics and evaporation of droplets are important but also long-range convective transport, turbulent dispersion and long-term local accumulation of virus-laden aerosols in distant areas become a key factor for indirect and airborne transmission of SARS-CoV-2 [7, 3, 9].

Bio-aerosol transport dynamics in indoor environments are notoriously complex and therefore not straightforward to assess due to its multi-scale-multi-physics nature [10]. Regions of quiescent (laminar) air flow coexist next to turbulent regions, where entrainment and dispersion processes become relevant. Breathing individuals and unsteady room ventilation generate high-velocity jets, but also much slower thermal plumes, resulting in fluid flows which span huge ranges of time and length scales. A large body of literature on these and related topics has emerged over the last decades and the recent pandemic has accelerated efforts and output substantially. However, many aspects of aerosol virus transmission in closed spaces are still not fully understood and affordable, robust modelling of the full system remains challenging [10].

Reynolds-Averaged-Navier-Stokes (RANS) approaches are well established in engineering and allow for simulations of statistically stationary flows to acceptable accuracy in many contexts (incl. complex indoor environments). Unsteady RANS can additionally account for slow variations on the integral length scale due to non-stationary ventilation or breathing. In URANS, the transport of aerosols and particles can be modelled through Euler–Euler approaches provided that the particle size and concentration are sufficiently small [11]. Scale-resolving multi-phase simulations (DNS, LES) provide very valuable insight into isolated aspects of the problem (e. g. coughing with mask [6, 12]) but are infeasible for realistic full-scale indoor scenarios.

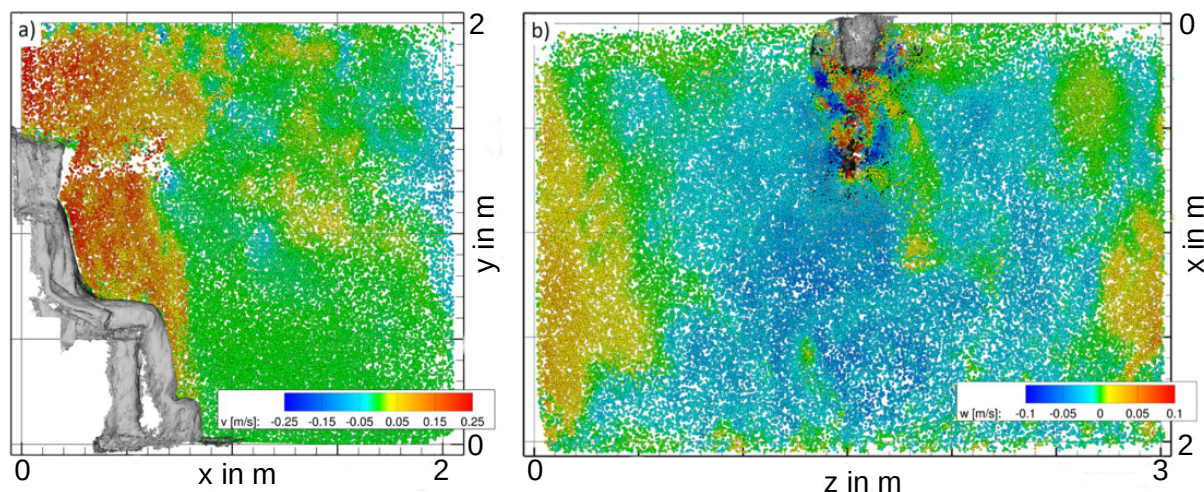


Figure 1: Experimental reference data base generated at DLR in Göttingen (Figure taken from Schröder et al. [13] and slightly modified). Shown are instantaneous snapshots of 3×10^6 HFSB tracked for 50 s through the entire room (3d) using the Shake-The-Box LPT approach [14]. a): Vertical slice ($z = 1.5$ m), where colour coding corresponds to the vertical velocity. b): Horizontal slice ($y = 1.5$ m), where colour coding corresponds to the lateral velocity.

Here, we aim at testing and validating computationally affordable and generally accessible CFD approaches for this specific task. A unique data set for a generic yet realistic full-scale room-breathing scenario (Fig. 1) recently generated at DLR in Göttingen [13] allows for the first time to validate commonly used CFD tools for this specific scenario. In that study, high-fidelity Lagrangian particle tracking (LPT) measurements were performed in a 12 m^3 room including a seated manikin to provide a generic yet realistic reference data set for typical indoor-ventilation scenarios. The manikin was heated to $32 \text{ }^\circ\text{C}$ and equipped with mechanical lungs to simulate breathing. Before measurement, the room was homogeneously seeded with helium-filled-soap-bubbles (HFSB). The HFSB are neutrally buoyant and can thus be considered as ideal tracers (alike aerosol particles). During measurements, up to 3×10^6 HFSB were tracked in the entire room for up to 50 s using 1800 high-power LED and six cameras. Raw particle locations were filtered in time using the TrackFit algorithm [15], yielding particle positions, velocities and accelerations at high spatial resolution and accuracy. Bubble trajectories were reconstructed using the Shake-The-Box LPT algorithm [14], followed by a regularised interpolation to an Eulerian grid using the FlowFit data assimilation method [15]; all three developed at DLR Göttingen. Subsequently, particle information was fed into FlowFit, which iterates millions of cubic B-splines to fit the measurement data making use of a physical regularisation via the Navier-Stokes equation to further increase spatial resolution. The result is a continuous function, describing velocity, acceleration and pressure in three-dimensional (3d) space. This function can be arbitrarily queried; via derivation, e. g. the full velocity gradient tensor is available, which has never been computed before for an entire room. As an example, Fig. 1 shows the instantaneous particle positions for a heavily breathing manikin and Fig. 2a shows the corresponding velocity field reconstructed from the continuous particle trajectories.

Comparing standard CFD methods against unique experimental data set

Here, we have conducted a large set of URANS simulations for the same set-up as in the Göttingen experiments based on the open-source framework **OpenFOAM** and using the most common closure models for turbulence modelling. Figure 2 exemplarily demonstrates qualitative and quantitative agreement of the flow fields predicted in our URANS simulations with the ones measured in Göttingen [13]. The entire scenario is dominated by two distinct flow features. First, the free-shear jet exhaled from the manikin and, second, the thermal plume rising from its heated body thereby driving a stable large-scale circulation in the upper half of

the room. Both defining features are well predicted by our URANS simulations (Fig. 2b) in good agreement with the experimental reference data set (Fig. 2a). Additionally, the warm exhaled jet is slightly tilted upwards due to buoyancy. This effect, for example, is clearly underestimated in the simulations, though. Figure 3 quantifies the performance of different closure models by comparing velocity profiles along a horizontal line extracted from different URANS simulations.

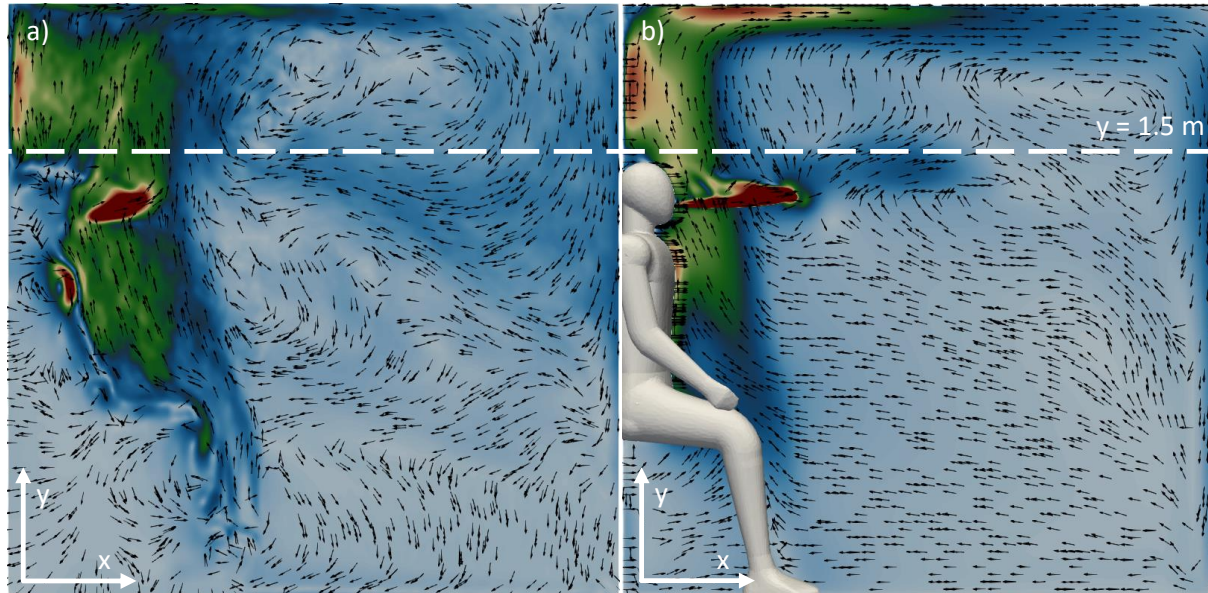


Figure 2: Phased-averaged flow field in our generic set-up during the phase of maximum expiration of the manikin. The magnitude of the flow velocity is shown in colour (from blue/slow to red/fast) and the in-plane velocity components are shown as vectors. The data is shown in an x-y-plane cutting through the manikin ($z = 1.5$ m). Broken lines indicate locations for data depicted in Fig. 3. a): From reference data base generated in a shake-the-box measurement campaign in Göttingen [13]. b): From our Reynolds-averaged Navier–Stokes simulation using a $k-\epsilon$ closure model.

Whilst the distinct peak in the up-welling thermal plume ($x \approx 0.2$) is very well reproduced by all $k-\epsilon$ -class models, it is slightly underestimated by all tested $k-\omega$ -type closure models. However, in the region where the exhaled free-shear jet is dominating the transport scenario ($x > 0.2$), the predicted flow field is highly depending on the choice of the closure model in combination with the local grid resolution. Especially with the standard $k-\epsilon$ -model, the exhaled jet is completely dissipated away for increasingly finer grids in the jet region (not shown here). Considering the first rough analysis shown here, out of all the tested closure models we recommend to use the low-Reynolds-Lauder–Sharma- $k-\epsilon$ or the $k-\omega$ -SST approach as a starting point for this type of problems. Both models predict the near-wall regions and the up-welling plume reasonably well and at the same time do not destroy the exhaled jets by overestimating the dissipation. This however leads to over-predicted life times of the exhaled jets; the local maxima at $x \approx 1$ represent jet residuals from the former breathing cycle, which are less pronounced in the reference data. Despite many details remain unanswered, it is important to note, that no validation and comparison of the standard closure models has been performed before for this specific scenario (heated/breathing manikin in closed room) due to the lack of an experimental data.

What next?

Next steps include optimising the model constants to better predict the decay of the exhaled jet and comparing the transport of (neutrally buoyant) aerosol particles based on the predicted flow fields (e. g. with additional Euler-Euler approaches) with the actual particle transport known from the experimental Shake-The-Box data set.

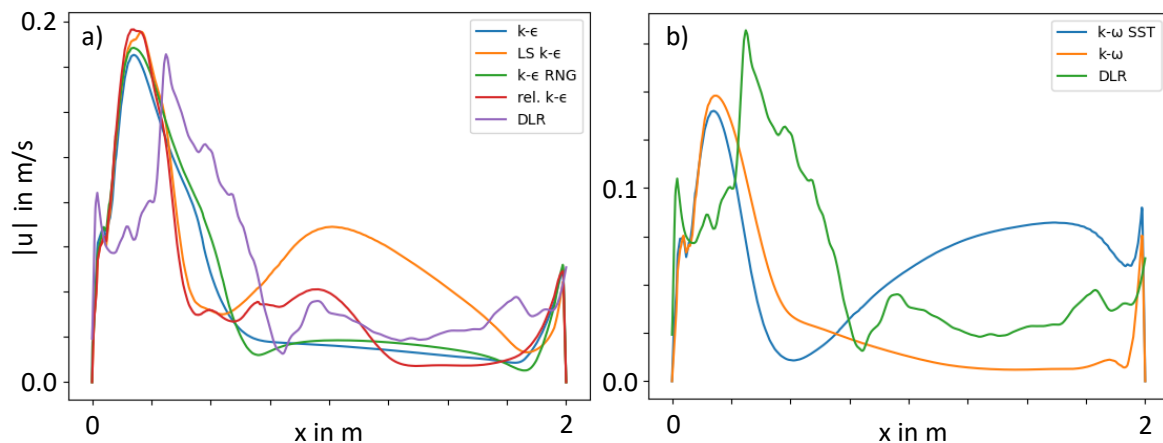


Figure 3: Performance of different turbulence models used in our simulations with respect to the experimental reference data base generated at DLR in Göttingen. Shown are phase-averaged velocity magnitudes ($|u|$) extracted along a horizontal line (x) as indicated in Fig. 2a): URANS results based on k - ϵ -type models. b): URANS results based on different k - ω -type models.

Presentations

1. D. Schanz, P. Godbersen, A. Schröder, **D. Feldmann**, **C. Kühn**, M. Avila, *CFD modelling of indoor aerosol transport based on experimental Lagrangian particle tracking measurements*, DFG wiss. Netzwerk Aerosolforschung, online, 2. Feb. 2021.
2. **C. Kühn**, **D. Feldmann**, M. Avila, *Validation of standard closure models for URANS simulations of indoor air flow scenarios based on a new Lagrangian particle tracking measurement data base*, DFG wiss. Netzwerk Aerosolforschung, Hamburg, 21. Apr. 2022.

References

- [1] Q. J. Leclerc et al., “What settings have been linked to SARS-CoV-2 transmission clusters,” *Wellcome Open Research*, vol. 5, p. 83, 6 2020.
- [2] H. Qian et al., “Indoor transmission of SARS-CoV-2,” *Indoor Air*, p. 12766, 2020.
- [3] L. Morawska and J. Cao, “Airborne transmission of SARS-CoV-2: The world should face the reality,” *Environment International*, vol. 139, p. 105730, 6 2020.
- [4] X. Xie et al., “How far droplets can move in indoor environments,” *Indoor Air*, vol. 17, p. 211, 6 2007.
- [5] M. Abuhegazy et al., “Numerical investigation of aerosol transport in a classroom with relevance to COVID-19,” *Phys Fluids*, vol. 32, p. 103311, 10 2020.
- [6] A. Khosronejad et al., “Fluid dynamics simulations show that facial masks can suppress the spread of COVID-19 in indoor environments,” *AIP Advances*, vol. 10, p. 125109, 12 2020.
- [7] N. van Doremalen et al., “Aerosol and Surface Stability of SARS-CoV-2 as Compared with SARS-CoV-1,” *New England Journal of Medicine*, vol. 382, p. 1564, 4 2020.
- [8] J. Lu et al., “COVID-19 Outbreak Associated with Air Conditioning in Restaurant, Guangzhou, China, 2020,” *Emerging Infectious Diseases*, vol. 26, p. 1628, 7 2020.
- [9] E. L. Anderson et al., “Consideration of the Aerosol Transmission for COVID-19 and Public Health,” *Risk Analysis*, vol. 40, no. 5, p. 902, 2020.
- [10] R. Mittal, R. Ni, and J.-H. Seo, “The flow physics of COVID-19,” *J. Fluid Mech.*, vol. 894, p. F2, 2020.
- [11] S. Balachandar and J. Eaton, “Turbulent dispersed multiphase flow,” *Ann Rev Fluid Mech*, vol. 42, p. 111, 2010.
- [12] K. Monroe et al., “Role of pulsatility on particle dispersion in expiratory flows,” *arXiv:2103.00581*, 2021.
- [13] A. Schröder, D. Schanz, J. Bosbach, M. Novara, R. Geisler, J. Agocs, and A. Kohl, “Large-scale volumetric flow studies on transport of aerosol particles using a breathing human model with and without face protections,” *Physics of Fluids*, vol. 34, p. 035133, mar 2022.
- [14] D. Schanz, S. Gesemann, and A. Schröder, “Shake-The-Box: Lagrangian particle tracking at high particle image densities,” *Experiments in Fluids*, vol. 57, p. 70, may 2016.
- [15] S. Gesemann, F. Huhn, D. Schanz, and A. Schröder, “From Noisy Particle Tracks to Velocity, Acceleration and Pressure Fields using B-splines and Penalties,” in *18th International Symposium on Applications of Laser Techniques to Fluid Mechanics*, (Lisbon), p. 17, jul 2016.

6.12 *hbi00056*: Pipes - gliding on air?

Turbulent pipe flow – drag reduction by superhydrophobic surfaces

HLRN Project ID:	hbi0056
Run time:	IV/2021 – I/2023
Project Leader:	Prof. Dr. Albert Baars
Project Scientists:	Alexander Koehnsen, Daniel Matz
Affiliation:	City University of Applied Sciences Bremen

Overview

Frictional drag at the interface between solid and liquid is a substantial contributor to increased energy demands in many technical applications. Several approaches have been addressed to reduce this type of drag in the past, ranging from riblets to gas bubbles (1, 2). A further approach is structured superhydrophobic surfaces which are able to retain air. Previous numerical simulations and experiments have indicated drag reductions DR in the two-digit percent range are achievable (3). One of the main challenges is balancing the structure size. Too small structures do not provide useful DR , while too large structures will not maintain the air layer. Therefore, it is pivotal to analyse how different geometries may influence DR while keeping structures small. This project deals with the application of air-retaining surfaces in pipe flows. We used direct numerical simulations at a friction Reynolds number of 180 to investigate different geometries (squared pillars as well as long holes with aspect ratios $AR = 2 \dots 8$) at a constant structure size in spanwise direction of $L^+ = 40$ to evaluate DR .

Methods

The air-filled surface structures are modelled on the inner surface of a cylinder with no-slip and slip boundary conditions. The no-slip area represents the area of the surface structure in contact with water and the slip boundary condition is assumed at the air-water interface. For all structure sizes a ratio of 75 % slip area to total area is used. All structures in this project show a structure size of $L^+ = 40$ in the spanwise direction. We investigated squared pillars ($L^+ = W^+$) and long holes with aspect ratios ($AR = W/L$) ranging from 2 to 8, resulting in a W^+ (size streamwise direction) of 80 to 320.

The computational domain is a cylinder with a radius r and a length of at least $2.5\pi r$. For the first gridpoint in the computational domain a distance normal to the wall of $y^+ \leq 0.04$ (in wall units) holds. A cyclic boundary condition is applied to the inlet/outlet and the boundaries in spanwise direction, while the walls have the aforementioned combination of slip and no-slip boundary conditions. The computational domain contains a Newtonian fluid with constant kinematic viscosity ν and density ρ . The flow is driven by a constant volume-related force in streamwise direction and the friction Reynolds number amounts to $Re_\tau = 180$.

Both the continuity and momentum equation are solved with the spectral element code Nek5000 (4) using a 3rd-order temporal and 5th (pressure) / 7th-order (velocity) spatial discretisation scheme. Comparisons of own results (reference case) with literature data at the same Re_τ from (5) show a good agreement (Figure 2 left) and the bulk velocity between the cases deviates by 0.88%.

Drag reduction DR was determined by the bulk velocity of the reference case (homogenous no-slip condition at the wall) u_{b0} and the bulk velocity with a partial slip boundary condition at the wall u_b .

$$DR = 1 - \left(\frac{u_{b0}}{u_b}\right)^2$$

Results

The drag reduction in pipe flow at $Re_\tau = 180$ and for different structures (reference, pillars, long holes) is plotted versus structure size in streamwise direction W^+ in Figure 1.

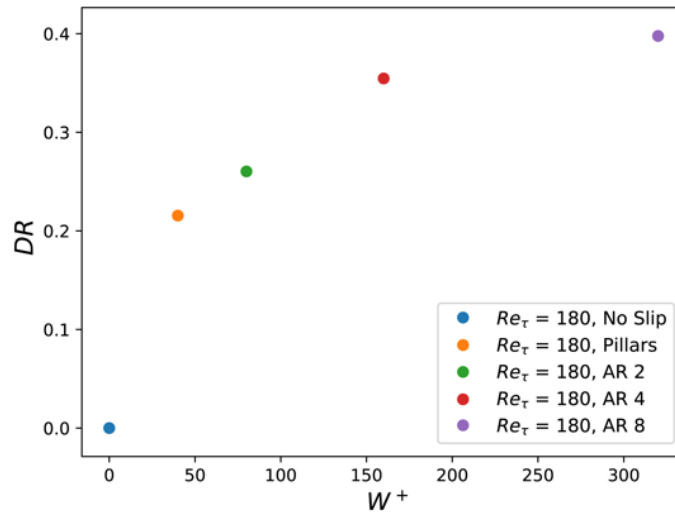


Figure 1: Drag reduction DR versus structure length W^+ for reference, pillars, and long holes with varying aspect ratios AR at a constant width $L^+ = 40$ and friction Reynolds number $Re_\tau = 180$

As expected, an increasing aspect ratio (via increasing structure size in streamwise direction W^+) leads to an increase in drag reduction. The results are consistent with previous work on channels (see hbi00042 report). The data points of the long holes seem to follow an asymptotic behaviour converging on the value of streamwise grooves. The value for pillars does not fully conform to this development. This may be explained by the corresponding velocity profiles (Figure 2).

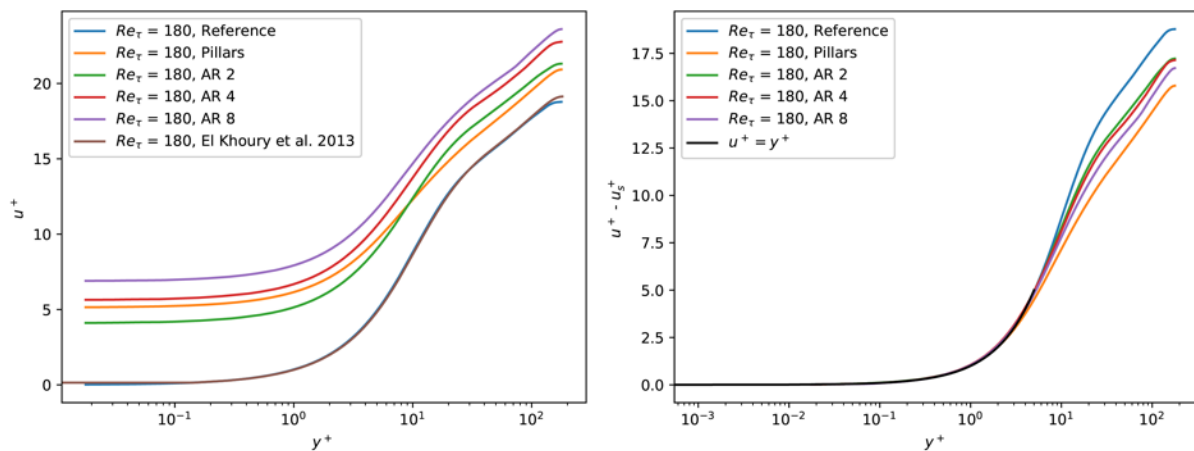


Figure 2: Averaged velocity in streamwise direction u^+ (left) and difference of u^+ with the slip velocity at the wall u_s^+ (right) versus wall normal coordinate y^+ in wall units for the reference case, pillars and long holes of different aspect ratios AR

The plot of u^+ versus y^+ shows a typical progression with a viscous sublayer, defect layer, a logarithmic domain and wake region for all profiles. Obvious differences between the shown cases appear in form of the velocity at the wall (slip velocity u_s^+) which grows from zero (reference case) via long holes of $AR = 2$, pillars, and long holes of $AR = 4$ and 8. This upward shift of the velocity profile leads to a rise in bulk velocity and is the reason for drag reduction. Hence, slip velocity u_s^+ and drag reduction DR are directly correlated at constant friction Reynolds number. This is not fully valid in the case of pillars, which show the lowest drag reduction of all structured surfaces but the second-lowest slip velocity. This results from the downward shift of the profiles in the defect layer which lowers the drag reduction. By subtracting the slip velocity from the velocity profile (Figure 2 b) this becomes evident. The highest downward shift appears for pillars followed by long holes of $AR = 8, 4$ and 2. The general effect of slip velocity and the downward shift has been described by (6,7).

The reason for the slip velocity at the wall results from the partial slip boundary condition. Figure 3 visualises the velocity at the wall of the tube for the investigated surface structures.

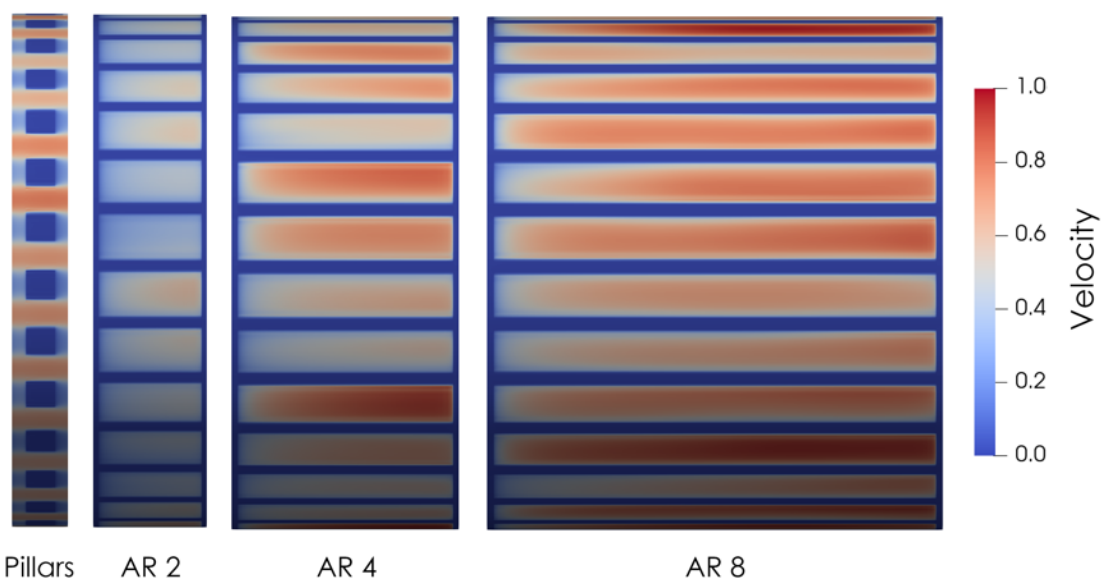


Figure 3: Instantaneous velocity fields at the wall for different surface structures all with $L^+ = 40$

Blue-coloured domains with a velocity of zero mainly correspond to the no-slip interface between solid and liquid. In the other parts, there is the gas/liquid interface. Two different types of gas/liquid interface can be distinguished: (a) no obstacles in the streamwise direction, here, maximal velocities occur, and (b) gas/liquid interface between obstacles in the streamwise direction. For (b) much lower local slip velocities occur due to the frequent deceleration of the liquid in the spanwise direction. Long holes feature both types of surface, (a) for small AR and (b) for $AR \rightarrow \infty$. Therefore, it is reasonable to receive higher slip velocities for pillars in comparison to long holes of lower AR .

The downwards shift of the velocity profiles for structured surfaces results from higher turbulent momentum transfer towards the wall in comparison to full no-slip boundary condition, see also (6,7). In the domain of slip surfaces turbulent motion can occur nearer to the surface. Furthermore, the comparison of profiles between pillars and long holes shows that the momentum transfer is higher for pillars in comparison to long holes. The smaller differences in the downward shift of velocity for long holes in comparison to pillars indicate, that the investigated range of parameter W^+ takes less influence on the momentum transfer than the change from long holes to pillars, see also the report of hbi00042.

Conclusion / Outlook

The presented results indicate that the geometry of the surface structure impacts both the slip velocity at the wall and the downward shift of the velocity profile due to turbulent momentum transfer. An increase in slip velocity leads to a rise in drag reduction and an increase in the downward shift to a decrease in drag reduction. Long holes show a rise in drag reduction with structure size in streamwise direction. For the investigated parameter range long holes feature higher DR than pillars of equal friction Reynolds number, area ratio and structure size in the spanwise direction.

Future works should consider longer calculation times for the long holes. The velocity profiles do not seem to be fully developed. Furthermore, smaller structure sizes in spanwise direction, and higher friction Reynolds numbers should be applied as well as the consideration of two-phase flows, see also the report of hbi00042.

Presentations

Köhnsen A, Kampf N, Wilms C, Trumann L, Matz D, Kacwin A, Hoffmann F, Kesel AB, Baars AJ (2022) Influence of Salvinia effect on drag reduction in closed and open turbulent channel flows. XXV International Symposium: Research Education and Technology 30.06.2022, Bremen

Literature

1. Murai Y (2014) Frictional drag reduction by bubble injection. *Exp Fluids* 55, 1773
2. Dean B, Bhushan B (2010) Shark-skin surfaces for fluid-drag reduction in turbulent flow: a review. *Phil. Trans R. Soc. A* 368, 4775-4806
3. Costantini R, Mollicone J-P, Battista F (2018) Drag reduction induced by superhydrophobic surfaces in turbulent pipe flow. *Physics of Fluids* 30, 025102
4. Fischer PF, Lottes JW, Kerkemeier SG (2008) NEK5000, Version V19.0 <http://nek5000.mcs.anl.gov>
5. El Khoury G, Schlatter P, Noorani A, Fischer PF, Brethouwer G, Johansson AV (2013) Direct Numerical Simulation of Turbulent Pipe Flow at Moderately High Reynolds Numbers. *Flow. Turbulence and Combustion* 91, 475 - 495
6. Seo J, Garcia-Mayoral R, Mani A (2016) Pressure fluctuations and interfacial robustness in turbulent flows over superhydrophobic surfaces. *J. Fluid Mech.* 783, 448-473
7. Min T, Kim J (2004) Effects of hydrophobic surface on skin-friction drag. *Phys. Fluids* 16, L55

This project is funded by the Federal Ministry of Education and Research, Germany (13XP5171B)

6.13 *hbk00059*: Joint state-parameter estimation for the Last Glacial Maximum with CESM1.2

HLRN Project ID:	hbk00059
Run time:	II/2017 – III/2023
Project Leader:	Prof. Dr. Michael Schulz
Project Scientists:	Dr. Tamás Kovács, Dr. André Paul
Affiliation:	Fachbereich Geowissenschaften, MARUM--Zentrum für Marine Umweltwissenschaften, Universität Bremen

Overview

This compute project is set within the framework of PALMOD, a BMBF-funded project that seeks to understand climate system dynamics and variability during the last glacial cycle. Specific topics are: i) to identify and quantify the relative contributions of the fundamental processes which determined the Earth's climate trajectory and variability during the last glacial cycle, ii) to simulate with comprehensive Earth System Models (ESMs) the climate from the peak of the last interglacial (the Eemian warm period) up to the present, including the changes in the spectrum of variability, and iii) to assess possible future climate trajectories beyond this century during the next millennia with sophisticated ESMs tested in such a way.

In the current phase, our main focus is on the direct forward modeling of stable water isotopes, combined with a comprehensive analysis of reconstructed and simulated isotope distribution. For this, we are using a global and comprehensive Earth system model: the Community Earth System Model version 1.2, in its isotope-enabled configuration (Brady et al. 2019). This version can provide stronger constraints regarding model-data comparison than simulations of only the basic physical variables without the explicit simulation of isotopes.

Results

The main outcome of this compute project in the previous year was the setting up and equilibrating a steady-state model run for the Marine Isotope Stage 3 (MIS3), and the analysis of its results. The MIS3 lasted from about 60 to 27 thousand years before present, and is characterized by climate variability on different time scales: most notably, by climate transitions between cold stadial and warm interstadial states on a multi-millennial time scale called Dansgaard-Oeschger events.

Our MIS3 simulation uses boundary conditions and greenhouse gas and orbital forcing representative of 38 thousand years before present, and has been intergrated to 5500 years to allow equilibrium even in the deep ocean. However, this equilibrium is only true on a longer time scale, as the model results show high-frequency oscillations in the strength of the Atlantic Meridional Overturning Circulation (AMOC). These are presented in Fig.1a that shows the time series of strength of the upper, North Atlantic Deep Water cell of the AMOC, defined here as the maximum value of the meridional barotropic streamfunction below 500 meters in the Atlantic Ocean at 30°N. According to Fig.1a the AMOC oscillates with an amplitude of nearly 7 Sv (Sverdrups; $1 \text{ Sv} = 10^6 \text{ m}^3\text{s}^{-1}$) in terms of extreme annual values, and its strength varies between 20 and 16 Sv when we apply a 100 years low-pass filter to remove sub-centennial signals from the series. The spectral analysis of the series in Fig.1b shows that it is dominated by a fluctuation of about 500 years.

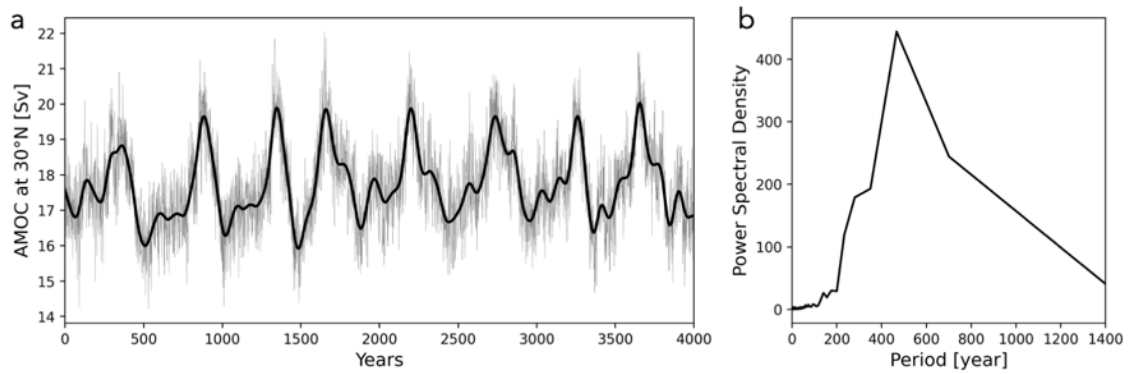


Figure 1: Simulated maximum AMOC strength at 30°N. **a** Annual (grey) and 100 years low-pass filtered (black) time series. **b** Power spectral density.

The variations in AMOC strength lead to changes in sea ice edge and surface temperature that are strongest in the North Atlantic Ocean. In order to evaluate the characteristics of surface temperature variability and their potential links to regional changes in the isotopic composition of precipitation, we have performed a Redundancy Analysis (RDA), a method that is able to identify pairs of patterns that are linked through a regression model. Detailed introduction of the method can be found in von Storch and Zwiers (1998), and an application of it in climate sciences in for example Kauker and Meier (2003). Here in our analysis the predictor is $\delta^{18}\text{O}$ in precipitation and the predictand is surface temperature.

The results of the redundancy analysis suggest that the AMOC-related variations in North Atlantic surface temperature are tightly linked to regional changes in $\delta^{18}\text{O}$ in precipitation. According to Fig. 2a, the first RDA mode of $\delta^{18}\text{O}$ in precipitation is centered over Greenland, with very weak or no signal elsewhere, and although it describes only 11.8% percent of predictand variance, it is the pattern that best represents the main mode of variance in the predictand, surface temperature, seen in Fig. 2b. The predictand pattern describes 35.2% of variance in surface temperature, and has two centers of action of the same sign: in the Labrador Sea and in the Nordic Seas. The time series of predictor and predictand patterns, plotted in Fig. 2c, are significantly correlated with a correlation coefficient of 0.87.

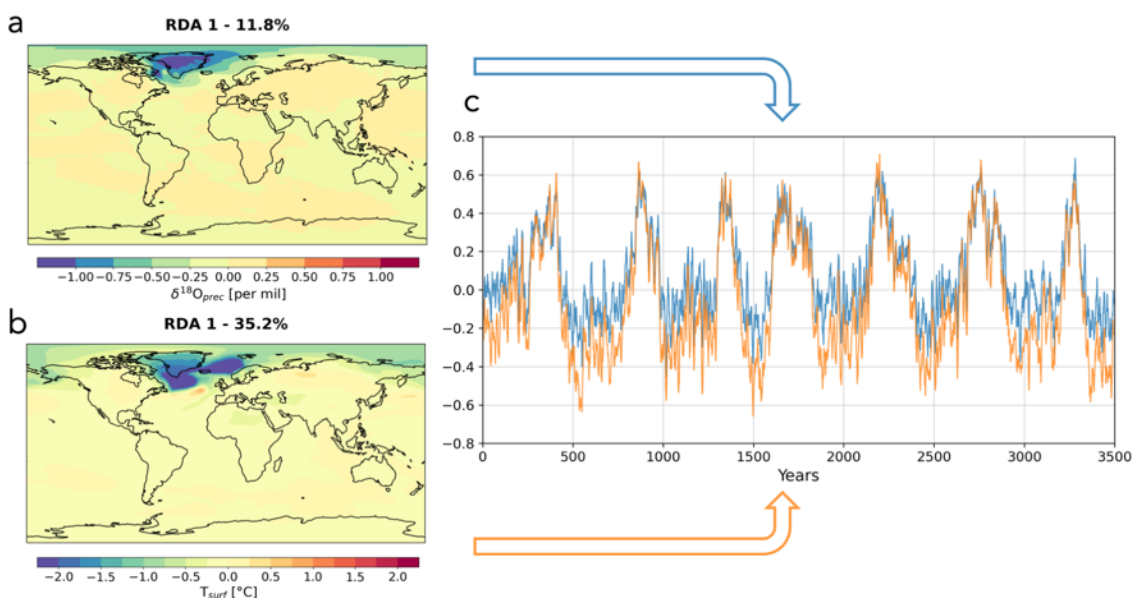


Figure 2: First redundancy mode between simulated $\delta^{18}\text{O}$ in precipitation as predictor (**a**) and surface temperature as predictand (**b**) and their time series (**c**).

The model results show that changes in $\delta^{18}\text{O}$ in precipitation over Greenland best represent North Atlantic surface temperature variations that are caused by the AMOC oscillations. This suggests that the isotopic composition measured in local ice cores is a potential proxy for AMOC variability. Therefore, we have analyzed $\delta^{18}\text{O}$ measurements in Greenland ice cores in order to search for variations analogous to those in our simulation.

Figure 3a shows time series of $\delta^{18}\text{O}$ measured in the ice core from the North Greenland Ice Core Project (NGRIP) site presented on the GICC05 time scale from Badgeley et al. (2020) covering most of the MIS3 period from 48 to 33 thousand years before present. The time series is dominated by large, multicentennial variations of abrupt enrichments followed by gradual depletion, resembling the typical sawtooth pattern of the Dansgaard-Oeschger events. These are different both in timing and shape from the oscillations in our model results. However, there are also occasional smaller variations on a centennial scale, for example in the period highlighted with grey background in Fig. 3a, enlarged in Fig. 3b. Comparing the event around 40 thousand years before present we can see that the time scale and amplitude of this observed event (in blue) is very similar to the oscillation in our model simulation for the same location (in orange). A spectral analysis for this selected shorter period in Fig. 3c shows that the modeled series are dominated by a fluctuation of about 500 years, and while the observations are dominated by lower frequency variations, there is a smaller local maximum around 500 years in the ice core data too. This provides evidence of an event similar to the variations in our model results both in amplitude and time scale.

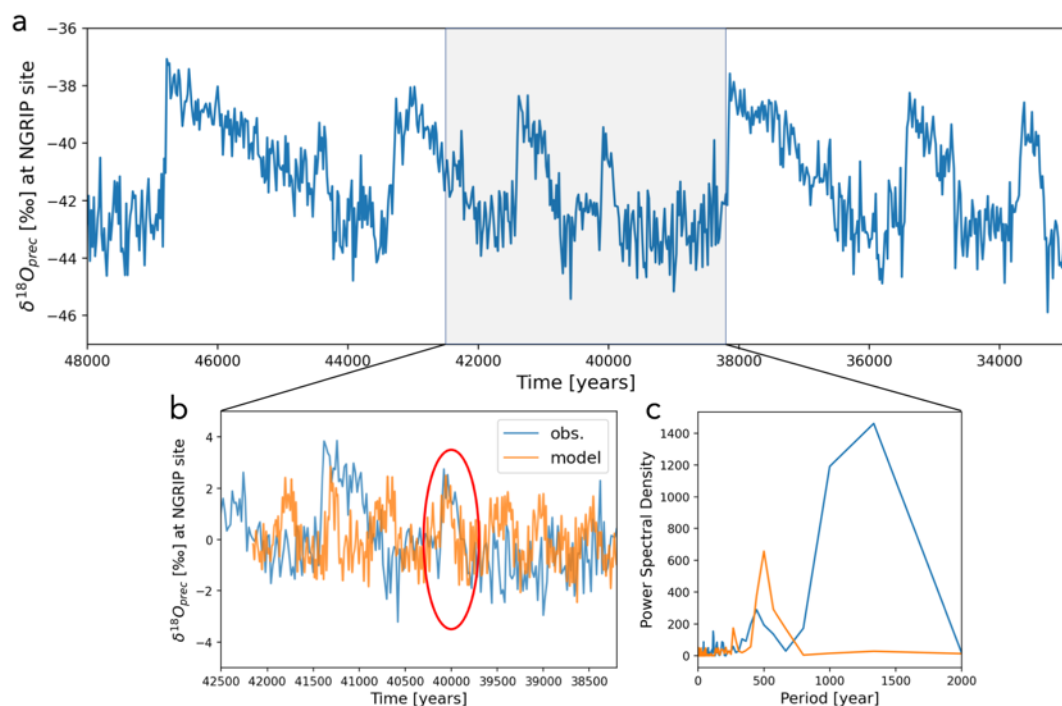


Figure 3: $\delta^{18}\text{O}$ in precipitation in Greenland at the NGRIP site. **a** Time series reconstructed from ice core observations (Badgeley et al. 2020), and **b** comparison of anomalies in ice cores and iCESM1.2 model simulations for the period 38.2ka-42.5ka and **c** their power spectral densities.

Outlook

Our planned experiments for the next year comprise transient simulations of different periods of the last glacial cycle. For the first time, transient simulations of the Marine Isotope Stage 3 and the last deglaciation will be performed with a fully coupled model with a full carbon cycle, as well as carbon and oxygen isotopes.

References

1. J. A. Badgeley, E. J. Steig, G J. Hakim, and T. J. Fudge, *Reconstructions of mean-annual Greenland temperature and precipitation for the past 20,000 years and the ice-core records used to create the reconstructions* (2020). Arctic Data Center.
2. Brady, E., Stevenson, S., Bailey, D., Liu, Z., Noone, D., Nusbaumer, J., Otto-Bliesner, B. L., Tabor, C., Tomas, R., Wong, T., Zhang, J., Zhu, J, *The connected isotopic water cycle in the Community Earth System Model version 1*. Journal of Advances in Modeling Earth Systems, 11, 2547–2566 (2019).
3. Kauker, F., and H. E. M. Meier, *Modeling decadal variability of the Baltic Sea: 1. Reconstructing atmospheric surface data for the period 1902–1998*, Journal of Geophysical Research: Oceans, 108 (2003).
4. von Storch, H., and F. W. Zwiers, *Statistical Analysis in Climate Research*, Cambridge University Press (1998).

Presentations

5. A. Dolman, T. Laepple, T. Kovacs, A. Paul, X. Shi, M. Werner, *Integrating water isotopes in climate simulations: Glacial-interglacial changes, variability and temperature*. PalMod General Assembly, Travemünde, 16-17 May 2022.
6. T. Kovacs, A. Paul, M. Schulz, *Simulated isotopic fingerprint of glacial AMOC variability*. PalMod General Assembly, Travemünde, 16-17 May 2022.

6.15 *hbk00062*: Retrieval of stratospheric ozone profiles from OMPS observations in limb geometry and long term trends

HLRN Project ID:	hbk00062
Run time:	IV/2017 – IV/2022
Project Leader:	Dr. Alexei Rozanov
Project Scientists:	Dr. Carlo Arosio, Dr. Alexei Rozanov
Affiliation:	Institute of Environmental Physics, University of Bremen

Overview

Stratospheric ozone recovery is expected during the 21st century according to model studies as a consequence of the decreasing emission of chlorine-containing ozone depleting substances (ODSs) and the increasing concentration of CO₂ in the troposphere. The ban of several ODSs after the Montreal Protocol has proven to be beneficial for the ozone layer.

To monitor the status of the ozone layer and the onset of its recovery, satellite measurements are an important tool, as they provide observations with high temporal and spatial resolution. In particular, measurements in limb geometry, as performed by SCIAMACHY (SCanning Imaging Absorption spectroMeter for Atmospheric Chartography) and OMPS-LP (Ozone Mapping and Profiler Suite – Limb Profiler), enable the study of ozone profiles with a vertical resolution of about 3 km. However, single satellite missions are generally too short to assess long-term ozone changes and the merging of several time series is required. Several studies using satellite merged data sets detected positive trends in the upper stratosphere, particularly at mid-latitudes: a hint of the ozone recovery.

In this framework, the main activities within this project are related to the retrieval of ozone profiles from OMPS-LP satellite observations, starting from the beginning of 2012 till present. The merging with the SCIAMACHY time series enabled the study of altitude-, latitude- and longitude-resolved ozone changes over the last 20 years. The validation with independent data sets showed a general good quality of the produced data set. Improvements in the retrieval of ozone profiles are ongoing and the release of a new version of Level 1 OMPS-LP data requires the re-processing of the entire time series. The comparison of the obtained trends with simulations from a chemistry transport model (CTM) is an example of the usage of the created data set and will be presented in the report.

Results

The improvement of the retrieved ozone profiles is a goal of this project and the quality of the profiles has been validated against independent measurements. To this aim, ozonesonde measurements are particularly valuable up to 30 km, whereas observations from the MLS (Microwave Limb Sounder) satellite instrument offer a valuable reference from 18 up to 60 km. Over the last years, the agreement with ozonesondes in the lower stratosphere was improved, with average discrepancy within 10%. The tropical lower stratosphere is a particularly challenging atmospheric region for satellite observations, as the sensitivity of limb measurements drops and the ozone concentration below ~18 km strongly decreases. Aerosol and cirrus clouds, although accounted for in the ozone retrieval, may still affect the results. A retrieval algorithm was implemented to derive particle number density and mean radius of polar mesospheric clouds, which occur in the summer hemisphere at high latitudes. This information was then used in the ozone retrieval and led to a significant improvement in the retrieved profiles in the presence of these clouds and to a better coverage of the polar regions.

An issue that is being tackled in the current months is the OMPS-LP drift with respect to independent satellite observations, e.g. from MLS, that was identified in the last years, particularly above 35 km. The NASA team has recently implemented some calibration corrections, a wavelength registration adjustment and improved the pointing of the instrument. The main aim of this update is the removal of the positive drift shown in the previous OMPS-LP ozone product. So far, a subset of data has been analysed, including one day of data per month, to check the improvements in the drift. In the left panel of Fig. 1, the drift between OMPS-LP and MLS time series is shown as a function of altitude and latitude, in terms of % per decade, over 2012-2020. In the right panel, the drift of the time series retrieved using the new version of L1 (2.6) data is shown. The absolute values of the drift are strongly reduced.

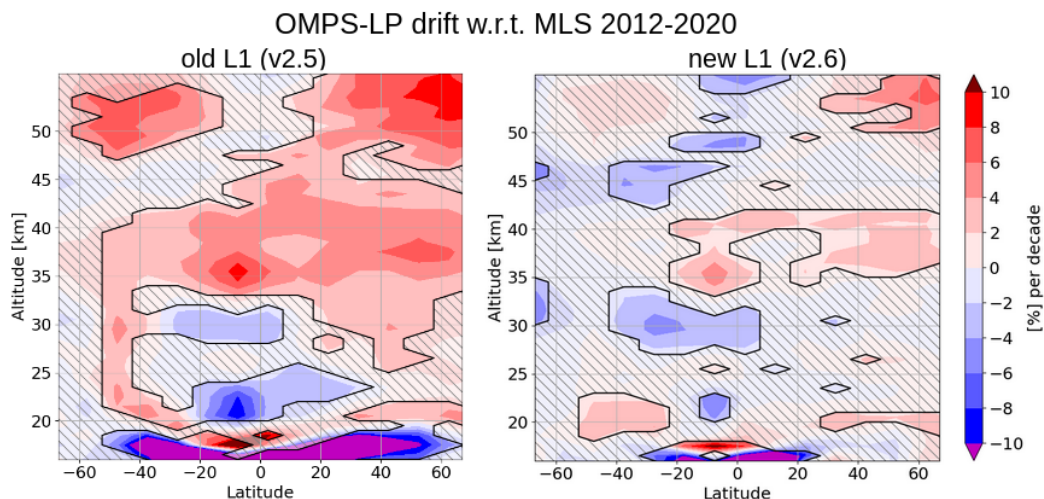


Figure 1: Drift in OMPS-LP ozone profiles w.r.t. MLS in % per decade over 2012-2020. Left panel: results when using the older data set, right panel when using the profiles retrieved with new L1 data.

Application of the merged data set

By merging SCIAMACHY and OMPS time series, we obtained an ozone data set (SCIA+OMPS) starting from 2003, vertically resolved every 3.3 km, and spatially binned every 5° latitude and 20° longitude. This enables the study of longitude-resolved structures and changes in the ozone distribution. To compute trends, a standard multi-linear regression approach was used, accounting for proxies like El Nino, QBO and solar activity. Recently a collaboration with the University of Leeds, made possible a comparison of the satellite trends with simulations of the TOMCAT CTM. The interest was to check whether the model reproduces the zonal asymmetries in trends and better understand their driving mechanisms. To this aim, we also computed seasonal trends, changes in the temperature field, and looked into meridional winds from ERA5 with a focus on the winter and spring seasons.

A good agreement between the CTM and the satellite trends was generally found. Large asymmetries are seen in winter and spring months at northern high latitudes. In Fig.2 the focus is brought to winter season, when a comparison of TOMCAT with the merged data set is more difficult as limb observations do not sample the polar night conditions. This highlights the importance of the usage of a CTM for the study. The satellite observations show larger positive values w.r.t. TOMCAT, possibly due to the positive drift affecting OMPS-LP time series after 2016. When considering the whole TOMCAT time series we discover a more complex structure with two positive and two negative cores over Greenland and Siberia. Trends in meridional winds show also a 4-core structure, similarly to the ozone plot, which point out a sort of rotation/transaltion of the polar vortex. These findings indicate a dynamical origin of the observed asymmetry, possibly related to the shift of the position of the polar vortex towards Siberia, which was pointed out by a previous study (Zhang et al. 2016).

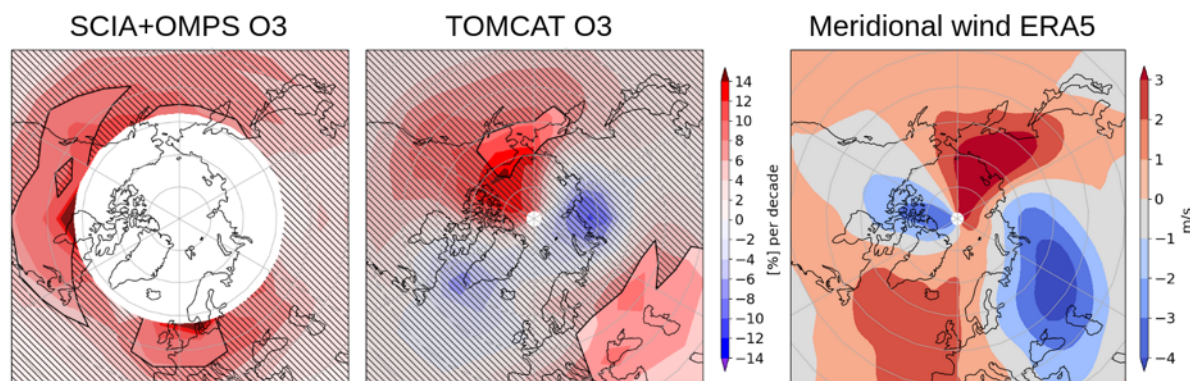


Figure 2: Long-term changes over 2003-2020 for winter months (DJF) at 40 km: in the left panel ozone trends from the SCIA+OMPS data set, in the middle ozone trends from TOMCAT, on the right meridional wind trends from ERA5. Shaded areas indicate non-significant values.

Outlook

The re-processing of the entire OMPS-LP data set is starting after some testing of the retrieval settings. This shall improve the long-term stability of the OMPS-LP time series, as shown, and give more robustness in the trend studies from merged data-sets including the OMPS-LP data.

Publications

1. Arosio, C., et al. "Merging of ozone profiles from SCIAMACHY, OMPS and SAGE II observations to study stratospheric ozone changes", *Atmospheric Measurement Techniques*, 12.4, (2019): 2423-2444.
2. Arosio, Carlo, et al. "Assessment of the error budget for stratospheric ozone profiles retrieved from OMPS limb scatter measurements." *Atmospheric Measurement Techniques* 15.20 (2022): 5949-5967.
3. Sofieva, Viktoria F., et al. "Updated merged SAGE-CCI-OMPS+ dataset for evaluation of ozone trends in the stratosphere." *Atmospheric Measurement Techniques Discussions* (2022): 1-27.
4. Weber, Mark, et al. "Global total ozone recovery trends attributed to ozone-depleting substance (ODS) changes derived from five merged ozone datasets." *Atmospheric Chemistry and Physics* 22.10 (2022): 6843-6859.

Presentations in 2022

- Living Planet Symposium, poster presentation:

"Investigating longitudinally resolved long-term ozone changes in the stratosphere using satellite limb observations and CTM simulations", Arosio C., Rozanov A., Chipperfield M. P., Dhomse S., Feng W., Burrows J. P.; LPS, May 13 - 27 2022.

- TRENDS 2022, oral contribution:

"Zonal asymmetries in ozone trends: a study using satellite limb observations and TOMCAT chemistry transport model", Arosio C., Rozanov A., Chipperfield M. P., Dhomse S., Feng W., Burrows J. P.; TRENDS, May 30 – June 3 2022.

6.16 **hbk00071: Development of an Earth system model coupled with a sediment diagenesis model toward long-term paleoclimate simulations**

HLRN Project ID:	hbk00071
Run time:	I/2022 – IV/2022
Project Leader:	Prof. Dr. Michael Schulz
Project Scientists:	Dr. Takasumi Kurahashi-Nakamura
Affiliation:	Fachbereich Geowissenschaften, MARUM – Zentrum für Marine Umweltwissenschaften, Universität Bremen

Overview

To reliably project the CO₂ level in the future, it is essential to understand the mechanisms for CO₂-level changes and to have comprehensive Earth System Models (ESMs) including the latest knowledge and skills. The last glacial cycle in the last 100 kyrs is considered to be one of the most qualified research targets offering many test cases with large variations in the CO₂ level.

Thus far, comprehensive models are unable to quantitatively reproduce the CO₂-level history in the 100 kyrs. This project will tackle that issue by focusing on the marine carbon cycle that would have played a key role in the variations of the CO₂ level.

In the previous phases of this project, we completed an interactive coupling of the Community Earth System Model version 1.2 (CESM1.2) and Model of Early Diagenesis in the Upper Sediment of Adjustable complexity (MEDUSA) and found that the MEDUSA-coupled CESM outperformed the uncoupled CESM in reproducing the observation-based global distribution of sediment properties through modern-based simulations (Kurahashi-Nakamura et al., 2020). The coupling will also contribute to the improvement of model representation of seawater chemistry. Moreover, the sediment model will act as a “bridge” between the ocean model and paleoceanographic data providing an important fingerprint for the paleo-carbon cycle.

We have subsequently carried out key time-slice simulations and demonstrated that the CO₂ concentration in the atmosphere both in the modern (pre-industrial) age (~280 ppm) and in the glacial age (~190 ppm) can be reproduced by the model with a common configuration by giving reasonable model forcing and ocean inventories of key biogeochemical tracers for the respective time slices (Kurahashi-Nakamura et al., 2022).

Results

Following the work in the previous year, further analyses on the three time-slice LGM simulations and the reference PI run that were based on the ICE-6G-C reconstruction were done (Fig. 1). Bottom-water salinity, carbonate-ion concentrations, and sea-ice extension were also added to the analyses in terms of the model-observation comparison to discuss the effect of different ocean circulation fields. Furthermore, the ocean inventories of total alkalinity and DIC in the four simulations were carefully assessed to examine the compatibility of the model states for two different time periods. Mass budget calculation showed that the differences in the ocean inventories can be readily explained by the changes in the sizes of other reservoirs in the climate system across the deglaciation, although large uncertainties of observation-based reconstructions of the changes in each reservoir size prevented us from constraining the model states better. This discussion would emphasize the importance of the reliable quantitative reconstruction of the flux of biogeochemical matter (at least) by the chemical

weathering on land and deposition into the sediments, which should be given as accumulative quantities throughout the glacial-interglacial climate evolutions.

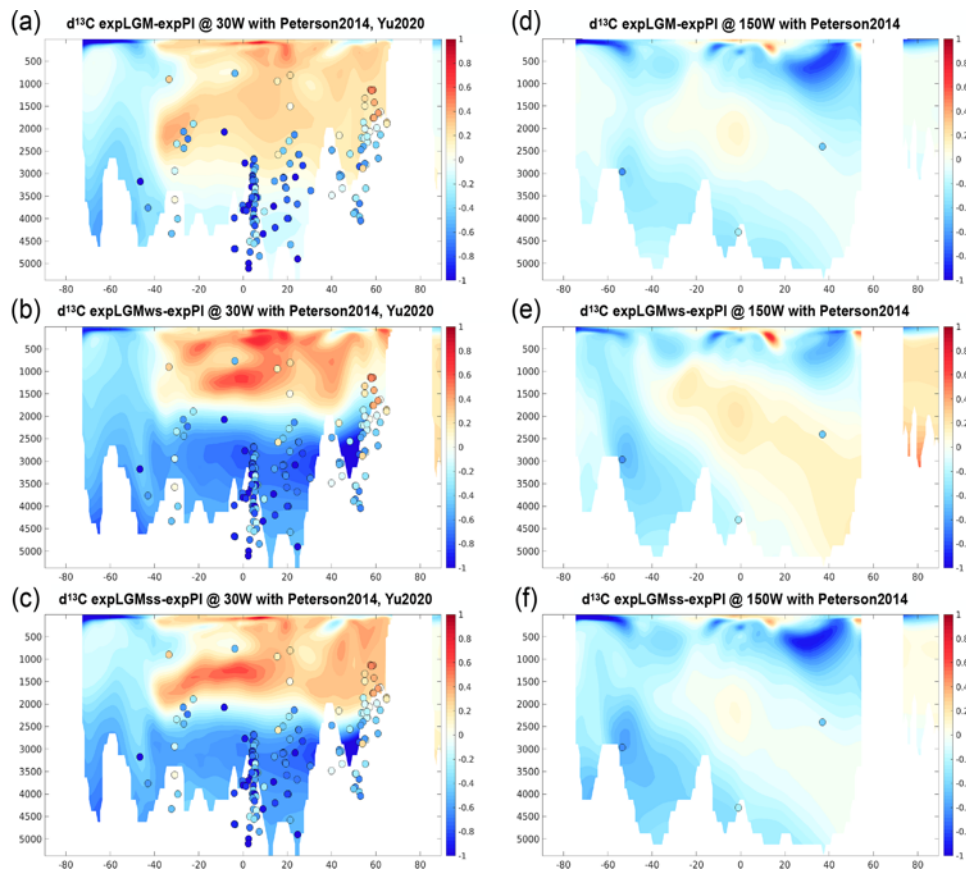


Figure 1: Meridional sections in the Atlantic (a–c; at 30W) and in the Pacific (d–f; at 150W) of the simulated $\delta^{13}\text{C}$ of DIC in the LGM experiments (‰) (Kurahashi-Nakamura et al., 2022): LGM (a, d), LGM with a weaker & shallower AMOC (b, e), and LGM with a stronger & shallower AMOC (c, f). The differences between LGM experiments and PI reference run are shown. The dots indicate observation-based reconstructions.

For comparison, LGM simulations with another ice sheet configuration based on GLAC-1D were also carried out, again with three different freshwater forcing. Systematic warming (higher global mean sea surface temperature by ~ 0.5 C) were observed as compared to the previous runs, which accordingly led to higher predicted $p\text{CO}_2$, although the differences were minor (~ 5 ppm). The global ocean circulation fields were not substantially affected in the standard LGM case and in the stronger-and-shallower-AMOC case as compared to those in the original simulations with the ICE-6G-C ice-sheet configuration, while the AMOC was further weaker in the weaker-and-shallower case being accompanied by a more extended sea-ice cover in the North Atlantic.

We also developed MIS3 (marine isotope stage 3) simulations with interactive carbon cycle, where the $p\text{CO}_2$ predicted by the carbon cycle module of the model were actually used for the radiative forcing in subsequent calculations. We hypothesized that the stadial periods during MIS3 can be divided into three types depending on the amount of aeolian dust flux in the Antarctic region and the emergence of Heinrich events, and selected 38ka, 29ka, and 21ka for target time slices corresponding to the three types. We configured the orbital, dust, and ice-sheet forcing for the three time periods and gave three different freshwater forcing to each of them to mimic increased freshwater input in stadials, which resulted in nine time-slice simulations in total. For the ocean biogeochemistry, we initialized the ocean inventory of DIC

and alkalinity by taking the model state of a time-slice LGM simulation, where they had been tuned so that the model predicted the glacial $p\text{CO}_2$ level (~ 190 ppm) and the increased deep-ocean carbon storage. The model results showed that the ocean inventories tuned for the LGM also worked for the MIS3 carbon-cycle simulations in a sense that the model was able to reproduce the reconstructed (ice-core based) CO_2 levels for MIS3 by giving appropriate external forcing (Fig. 2). Analyses of the nine simulations showed that the different dust input had larger influence on the modelled $p\text{CO}_2$. We did not find conclusive differences between two types with higher dust input in the framework of this study. Freshwater perturbation of a different magnitude might be able to explain the difference, but the relationship between the length of stadials and freshwater input pattern should be further examined.

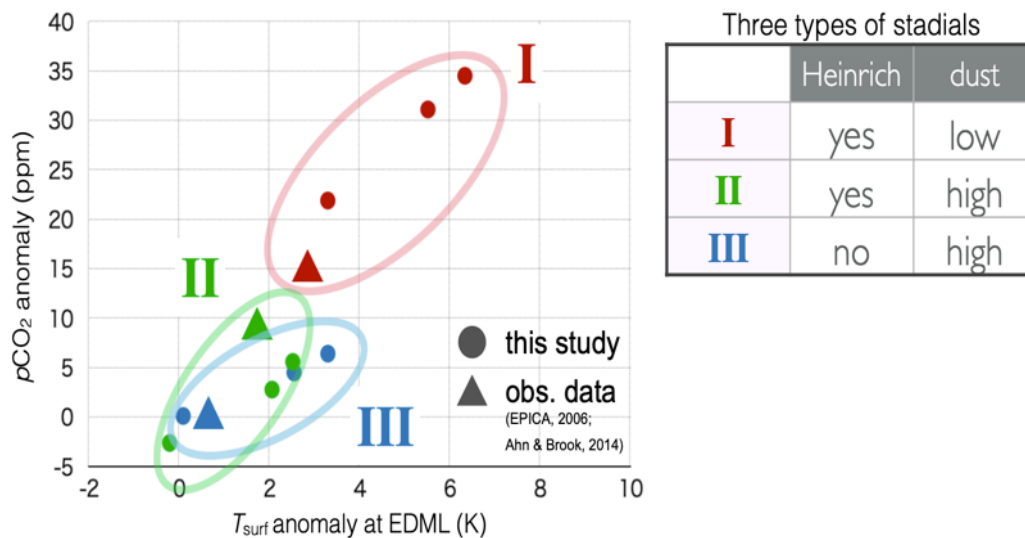


Figure 2: Model-observation comparison in terms of the increment of the atmospheric $p\text{CO}_2$ and the surface temperature at the EDML site during the stadial periods. The suggested three types for MIS3 stadials (type I, II, III shown in the embedded table) correspond to 38ka, 29ka, 21ka, respectively. For the model results (dots), three simulations with different freshwater forcing are shown for each time slice.

Outlook

In the future work, the simulated ocean states are expected to serve as an initial state for transient runs that is expected to simulate dynamical climate evolutions. The balance of the bulk ALK and DIC budgets show that all the LGM simulations in this study are likely to be compatible with the pre-industrial state within the uncertainties of available constraints, at least from a mass balance point of view. The question of whether they would indeed reach the pre-industrial state with a realistic trajectory would need to be examined in a transient context. Shelf or shallow-water processes accompanied by sea-level changes such as the land weathering and deposition of biogeochemical matter would be fundamental to the evolution of the global carbon cycle at the glacial-interglacial timescale, not only for the post-glacial evolution but also during the evolution in the time period that preceded the LGM. Considering that the sea-level change is a direct consequence of the ice sheet evolution induced by climate changes, it would be essential to analyse and discuss the evolution of the coupled carbon cycle–ice sheet system.

Publications

1. Kurahashi-Nakamura, T, A. Paul, U. Merkel, and M. Schulz, *Glacial state of the global carbon cycle: time-slice simulations for the last glacial maximum with an Earth-system model*, *Clim. Past*, 18, 1997–2019, <https://doi.org/10.5194/cp-18-1997-2022>, 2022.

Presentations

1. Kurahashi-Nakamura, T, A. Paul, U. Merkel, and M. Schulz, *MIS3 simulations with interactive carbon cycle using CESM, 3rdPalMod* General Assembly, Lübeck-Travemünde, May 16, 2022.
2. Kurahashi-Nakamura, T, A. Paul, U. Merkel, and M. Schulz, *Glacial state of the carbon cycle: time-slice simulations with CESM, 3rdPalMod* General Assembly, Lübeck-Travemünde, May 16, 2022.
3. Kurahashi-Nakamura, T, A. Paul, U. Merkel, and M. Schulz, *Carbon cycle simulations for MIS3: for three time slices*, 27th Annual CESM Workshop PALEOCLIMATE WORKING GROUP MEETING, online, June 15, 2022.

6.17 *hbk00075*: Assessing the effect of environmental and biological conditions on Antarctic krill large-scale connectivity facilitated by ocean currents

HLRN Project ID:	hbk00075...
Run time:	IV/2019 – IV/2022
Project Leader:	Prof. Dr. Björn Rost ¹
Project Scientists:	Dr. Judith Hauck ² , Dr. Bettina Fach, Dr. Ralph Timmermann
Affiliation:	Alfred-Wegener-Institut, Helmholtz Zentrum für Polar- und Meeresforschung ¹ principal investigator, also at the University of Bremen, ² project administrator

Overview

Antarctic krill, *Euphausia superba*, has long been recognized as a key component of the Antarctic marine food web (Marr, 1962) playing a fundamental role in the transfer of energy between the lower and the upper trophic levels. It inhabits the Southern Ocean predominantly south of the Polar Front, with recent estimates of the total stock biomass ranging between 169 and 379 million metric tons (Siegel, 2005; Atkinson et al., 2009). Antarctic krill, like other species, has been shown to be impacted by the observed regional warming. Specifically, their distribution in the south-west Atlantic sector, their main population center, has been shown to shift southward, retreating towards the Antarctic continental shelves (Atkinson et al., 2019).

Many marine populations, including Antarctic krill or other zooplankton and fish stocks, are structured by their physical environment. As a result, the spatial relationships between physical and biological processes are potentially key to understanding their distribution and abundance. Dispersal occurs mostly during early life through advection by ocean currents, when young individuals are not yet capable of active movement. Older life stages exhibit behavior and active movement and can therefore often move on different spatial scales. Larval dispersal by ocean currents and the resulting connectivity between different oceanic regions have been identified as crucial factors for structuring marine populations (Cowen et al., 2006) as well as for designing networks of Marine Protected Areas (MPAs) (Lester et al., 2009), or even understanding the spread of marine pests (Glasby and Lobb, 2008).

Studies in the Lazarev Sea concluded that this region does not support a single self-maintaining krill population, but represents a complex transition zone of stocks with different origins. Krill recruitment is strongly influenced by the environmental conditions that krill face upstream of the region under investigation as krill is subject to large-scale transport by ocean currents (Hofmann et al., 1998; Fach et al, 2006, Pinones and Fedorov, 2016) and a constantly changing seascape that provides changing food environments during this transport.

In this project we use a global version of the Finite Element Sea Ice-Ocean Model (FESOM) coupled with the Regulated Ecosystem Model 2 (REcoM2) to investigate the possible connectivity of Antarctic krill (*Euphausia superba*) throughout the Southern Ocean via ocean currents with special focus on the Lazarev Sea. Lagrangian particle simulations with an individual based model (IBM) of krill utilize the FESOM-REcoM2 model output in form of environmental conditions (temperature, salinity and currents) as well as biological conditions (phytoplankton and zooplankton distribution and abundance) The aim is to find populations supplying input to the Lazarev Sea krill population, and investigate how environmental and biological factors impact population dynamics of Antarctic krill during transport.

Results

Over the past year, we have completed all changes to the model code which were necessary to address the aims highlighted in the previous section. We have settled on the BOLD mesh with a resolution of ~15 km in the areas of interest, and investigate the differences between low and high resolution on the connectivity and help understand the population dynamics of the Lazarev Sea krill population as planned.

As expected, the high-resolution simulation is showing much more detail in current structure of the ACC and the drifter paths that is evident between simulations. This is of importance in the context of this study, as eddies are important features for krill retention and accumulation of food such as phytoplankton and copepods.

Lagrangian drifter simulations show three main transport patterns in the Lazarev Sea with retention in the Lazarev Sea (~67S to 63S), transport into the Weddell Sea via ASC, and northward transport and entrainment into currents of the ACC with export out of the study area (Figure 1). The three patterns make for very different environmental conditions and, more importantly, available food for krill. The effect of these different conditions was tested with a krill IBM (Fach et al. 2008) and results show that retention in the Lazarev Sea provides the best environment for growth of larvae and juveniles (Figure 2A). Also, recruitment is best when krill larvae are retained in the Lazarev Sea, while transport into the ACC increases recruitment of juvenile krill. Recruitment is defined as follows: larvae are able to reach juvenile stages and juveniles reach adult stage during transport. These results are very encouraging and prove that the concept is working and gives an insight into the connectivity and population dynamics of krill.

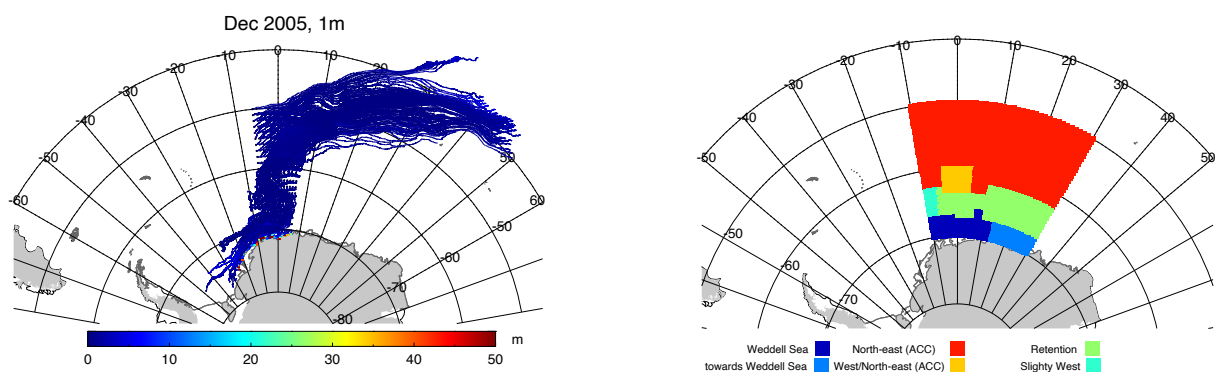


Figure 2: Left panel: Lagrangian drifter paths of particles representing Antarctic krill in the surface layer of the FESOM-REcoM2 simulation using Core grid starting December 2005. Right panel: summary of all Core grid simulation drifter paths over 10 years and three release months (December, January, February).

A more detailed look at the seasonal variability at specific Lazarev Sea regions Lagrangian drifter analysis undertaken with the BOLD grid simulation show a consistent westward transport in the Antarctic Slope Current towards the Weddell Sea during forward simulations in November to January (Figure 4 A,C,E) that is consistent with previous results (Figure 2). This supports the theory that Lazarev Sea krill is not persistent locally but is transported out of the area, mainly westward over time. However, when looking at the backtracking simulations (Figure 4 B,D,F) it can be seen that drifter actually show strong meandering around the release station itself with very little dispersal. This indicates that particles found at Station 92, were spawned with in a small region around the station and were retained there, before being transported towards the Weddell Sea the following year, pointing to a degree of retention in

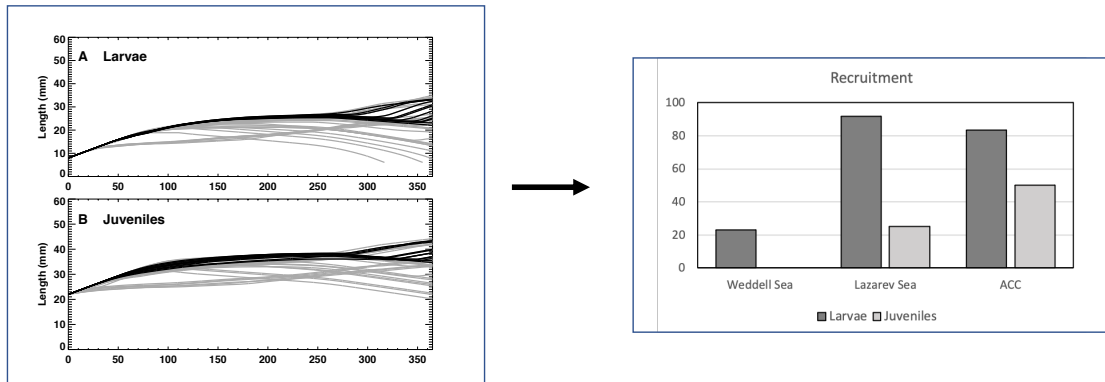


Figure 3: Left panel: Time series of Antarctic krill growth rates of (A) larval krill and (B) juvenile krill when feeding on food available along drifter paths using a biochemical krill IBM (Fach et al., 2008). Right lower panel: Recruitment of Antarctic krill into the Lazarev Sea population considering the three different main transport pathways of Figure 2.

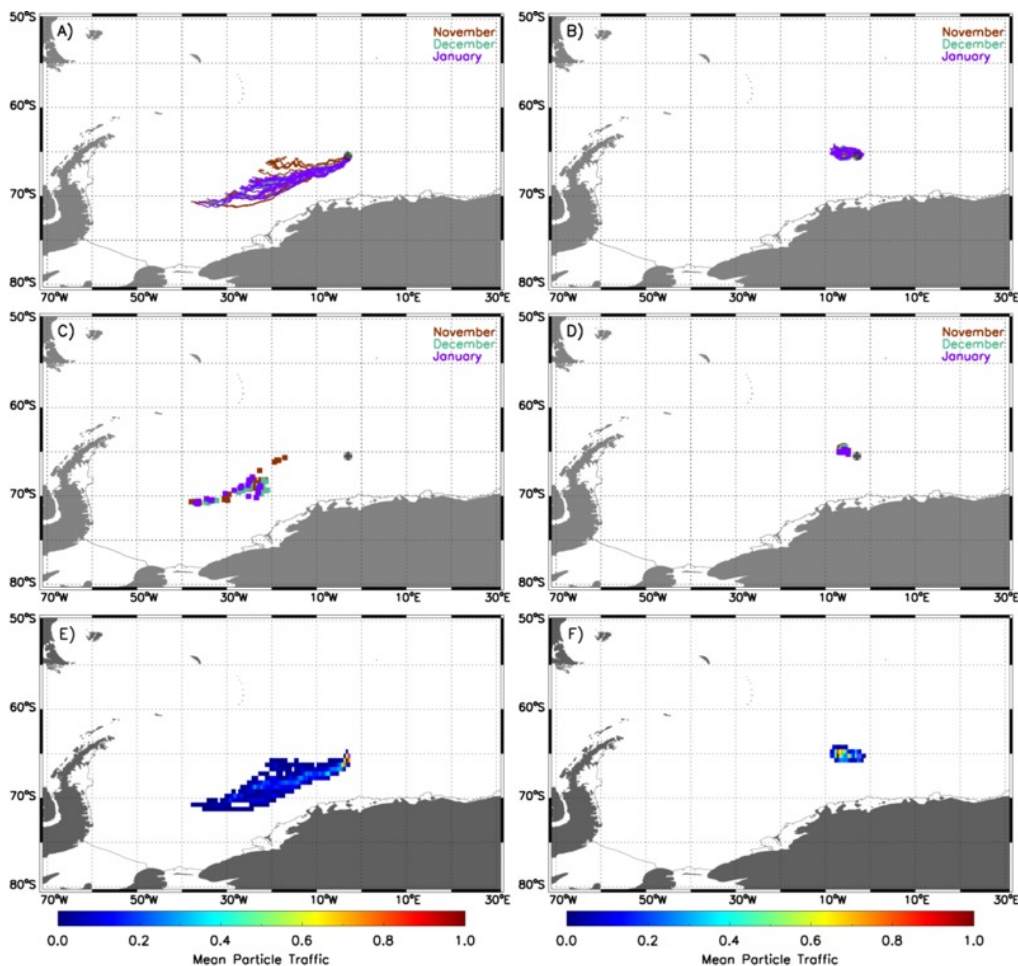


Figure 4. Lagrangian Particle tracking trajectories of station 92 released in austral summer 2005 drifting A) forward in time from 2005 to 2006, B) drifting backwards in time from 2005 to 2004, C) end points of particles tracked forwards in time from 2005 to 2006 (squares). D) End points of particles tracked backwards in time from 2005 to 2004 (squares), E) Mean particle traffic map of particles tracked forwards in time from 2005 to 2006 scaled between 0.0 and 1., F) Mean particle traffic map of particles tracked backwards in time from 2005 to 2004 scaled between 0.0 and 1.0. Black diamonds denote the release point of particles.

the area despite high westward transport potential. This is supported by calculations of the distance to the origin of the forwards vs backward tracked particles. The mean forward lies between the 1000-1200km range, compared to the smaller 150-620km station mean ranges for the backwards tracked particles.

Outlook

While the existing experiments with FESOM-REcoM2 provide a comprehensive overview over the connectivity in the Lazarev Sea and the role of grid spacing in modeling, it remains a question whether future climate change has a significant effect on this connectivity. To address this question, we are planning a future scenario simulation for the time frame 2030-2040 with this setup. It will allow us to investigate how changes in circulation and biological factors in that time frame impact on the connectivity and population dynamics of the Lazarev Sea krill population in comparison to present day.

References

- Atkinson A., Siegel V., Pakhomov E.A., Jessopp M.J., (2009) A re-appraisal of the total biomass and annual production of Antarctic krill. *Deep-Sea Research Part I: Oceanographic Research Papers* 56: 727–740.
- Atkinson A., Hill, S.L., Siegel V., Pakhomov E.A., Siegel, V., Reiss, C.S., Loeb V., Steinberg, D.K., Schmidt, K., Tarling, G.A., Gerrish, L., Sailley, S.F. (2019) *Nature Climate Change*. <https://doi.org/10.1038/s41558-018-0370-z>
- Cowen, R.K., Paris, C.B., Srinivasan, A. 2006. “Scaling of connectivity in marine populations,” *Science* 311:522-527. doi: 10.1126/science.1122039
- Fach, B. A., Hofmann, E. E., & Murphy, E. J. (2006). Transport of Antarctic krill (*Euphausia superba*) across the Scotia Sea. Part II: Krill growth and survival. *Deep-Sea Research Part I: Oceanographic Research Papers*, 53(6).
- Fach, B.A., Meyer, B., Wolf-Gladrow, D., Bathmann, U. (2008). A biochemically based model of the growth and development of Antarctic krill (*Euphausia superba*). *Marine Ecology Progress Series*, 360: 147-161.
- Hofmann, E.E., Klinck, J.M., Locarnini, R.A., Fach, B., Murphy, E., 1998. Krill transport in the Scotia Sea and environs. *Antarctic Science* 10 (4), 406–415.
- Lester, S., Halpern, B., Grorud-Colvert, K., Lubchenco, J., Ruttenberg, B., Gaines, S., Aíramé, S. and Warner, R.R. 2009. Biological effects within no take marine reserves: a global synthesis, *Mar. Ecol. Prog. Ser.*, 384: 33–46.
- Marr, J.W.S., 1962. The natural history and geography of the Antarctic krill *Euphausia superba* Dana. *Discovery Reports* 32, pp. 37-465.
- Pinones, A., and A. V. Fedorov (2016), Projected changes of Antarctic krill habitat by the end of the 21st century, *Geophys. Res. Lett.*, 43, 8580–8589.

Publications

Additional model experiments and the analysis of completed experiments are on-going, therefore there is no publications or presentation of the results yet.

Presentations

Fach B.A, Cagdas, B., Sadighrad E., Gurses, O., Hauck, J., Timmermann, R., Wekerle, C. Modeling the Connectivity of Antarctic Krill (*Euphausia Superba*) in the Lazarev Sea. 5th National Marine Science Conference 2022.

6.18 *hbk00079*: Tipping points in Antarctic Bottom Water formation and Southern Ocean carbon sequestration

HLRN Project ID:	hbk00079
Run time:	I/2022 – IV/2022
Project Leader:	Prof. Dr. Björn Rost ¹
Project Scientists:	Dr. Cara Nissen ² , Dr. Judith Hauck, Dr. Mario Hoppema, Dr. Ralph Timmermann
Affiliation:	Alfred Wegener Institute, Helmholtz Centre for Polar and Marine Research

¹principal investigator, also at the University of Bremen,
²project administrator

Overview

The Southern Ocean plays an essential role in oceanic carbon uptake, carbon sequestration, global ocean circulation, and hence global climate, but the ability of this ocean basin to draw down atmospheric CO₂ has varied in the past and is projected to be altered in the future due to on-going climate change (Hauck et al., 2015). In general, ocean circulation largely controls the oceanic uptake of CO₂ and the transfer of carbon to greater depths in the Southern Ocean. On the one hand, the upwelling of deep-water masses brings naturally carbon-rich waters to the surface layers, where the carbon can be released to the atmosphere (Fig. 1a). On the other hand, large amounts of carbon are locked away from the atmosphere by the sinking of water masses to the ocean floor at high-latitudes, i.e., the formation of Antarctic Bottom Water. In this context, the Antarctic Bottom Water formation regions have been suggested to dominantly set global atmospheric CO₂ levels (Marinov et al., 2006), as these can sequester carbon on time scales of centuries to millenia. Amongst all Antarctic Bottom Water formation regions, the Weddell Sea has been suggested to be the most important one (Orsi et al., 1999), making any change in Antarctic Bottom Water formation in this area especially critical for global carbon cycling and climate.

The formation of Antarctic Bottom Water is a result of an increase in the density of surface waters (Orsi et al. 1999), due to air-ocean and ice-ocean interactions, i.e., due to a cooling from the overlying atmosphere and due to the increase in salinity as a result of ice formation, respectively (Fig. 1a). Similarly, this suggests that any addition of freshwater to the Southern Ocean, which leads to a decrease in water density, directly impacts the formation rates of Antarctic Bottom Water and subsequently Southern Ocean carbon transfer to depth. In fact, as a consequence of the recent warming, the mass loss of Antarctic ice sheets has accelerated over the last decades (Rignot et al., 2019), discharging additional freshwater into the coastal areas of the Southern Ocean. While especially the melt rates of ice shelves in West Antarctica have accelerated, those in East Antarctica, including the Weddell Sea, have done so to a much lesser extent (Rignot et al., 2019). However, modeling experiments have demonstrated the possibility of accelerating melt rates of ice shelves in the Weddell Sea in the upcoming centuries as well (Timmermann & Hellmer 2013), with a possible complete shutdown of Antarctic Bottom Water formation within a few decades (Lago & England 2019). Yet, the possible response of Antarctic Bottom Water formation rates and Southern Ocean carbon cycling to the expected future changes in freshwater discharge remain surrounded by large uncertainties or largely unquantified altogether, as these have so far been hindered by model resolution and/or missing model complexity, e.g., by not accounting for changing freshwater discharge from ice shelves and associated feedbacks in their simulations.

In this project, our goal is to quantify changes in Antarctic Bottom Water formation and carbon sequestration over the 21st century by performing model experiments with FESOM1.4-REcoM2 (Wang et al., 2014; Danilov et al., 2015; Hauck et al., 2013; Karakus et al., 2021). The setup used here resolves ice shelf cavities and has an eddy-permitting grid resolution in the Weddell Sea, allowing for a realistic representation of processes inducing Antarctic Bottom Water formation in this area.

Results

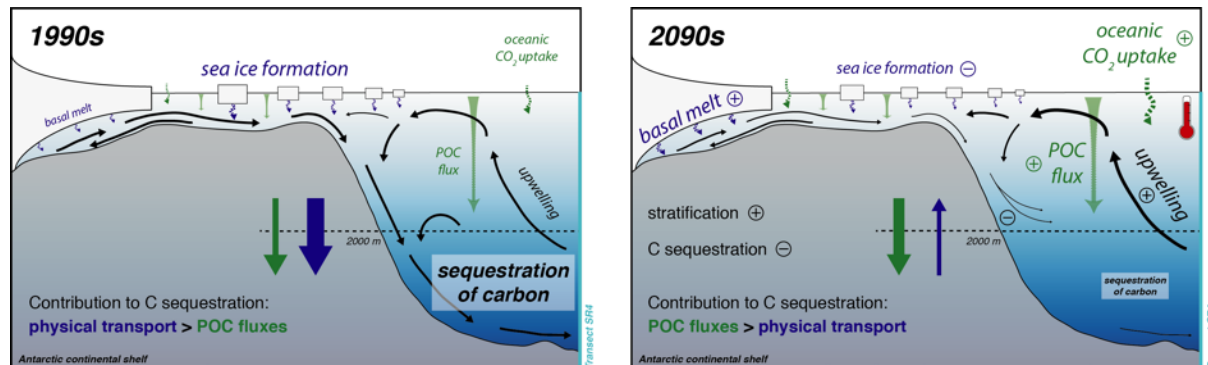


Figure 1: Sketch illustrating the main features of high-latitude Southern Ocean circulation (black arrows), of the air-ocean and ice-ocean interactions involved in water mass transformations (blue), and of high-latitude carbon cycling (green). POC = Particulate Organic Carbon. Panel a shows the 1990s, when carbon sequestration in the deep ocean with physical transport is stronger than with biological POC fluxes. Panel b shows the 2090s for the high-emission scenario SSP5-8.5, when newly formed dense waters leaving the continental shelf are too light to reach the deep ocean, resulting in a reduction in deep-ocean carbon sequestration. The Figure is taken from Nissen et al. (2022), see publication list below.

Over the past year, we have completed several additional model experiments with FESOM1.4-REcoM2. In addition to the high-emission scenario SSP5-8.5 completed earlier, we have performed simulations under three additional emission scenarios: SSP1-2.6, SSP2-4.5, and SSP3-7.0 (sorted from low to high emission). All simulations are forced with atmospheric output from the AWI Climate Model (Semmler et al., 2020). With this set of simulations, we assessed the sensitivity of 21st-century change in AABW formation and carbon sequestration to the chosen emission scenario.

Under historical and high-emission scenario forcing (SSP5-8.5), our analysis revealed an abrupt attenuation of carbon sequestration with Weddell Sea dense waters at the end of the 21st century (Nissen et al., 2022, Nature Communications). This was attributed to physical changes on the southern continental shelves, which resulted in newly formed dense waters that were too light to efficiently transfer carbon to the deep ocean (Fig. 1b). Follow-up analyses revealed that a tipping point has been crossed by 2100 for the high-emission scenario SSP5-8.5, but not (yet) for three lower-emission scenarios. After the crossing, a physical-biogeochemical tipping point cascade is set in motion. The cascade is characterized by a reversal of shelf-open ocean density gradients, the invasion of the shelf by relatively warm and oxygen-poor Warm Deep Water, which accelerates ice-shelf basal melt, the absence of newly formed dense waters that have the potential to reach the abyss, and the subsequent changes in deep-ocean carbon and oxygen transfer. This work is currently under review for publication in Journal of Climate (Nissen et al., 2023).

Outlook

The HLRN project hbk00079 came to an end in the fourth quarter of 2022. Over the course of this and next year, the analysis of the data resulting from this project will continue and additional publications are in preparation.

Publications

Nissen, C., R. Timmermann, M. Hoppema, Ö. Gürses, and J. Hauck. Abruptly attenuated carbon sequestration with Weddell Sea dense waters by 2100, *Nature Communications*, 13, 3402, <https://doi.org/10.1038/s41467-022-30671-3>, 2022.

Nissen, C., R. Timmermann, M. Hoppema, and J. Hauck (2023), A physical-biogeochemical tipping point cascade initiated on Weddell Sea continental shelves is avoidable in a 2°C scenario. In review in *Journal of Climate*.

Presentations

Ocean Sciences Meeting (virtual, March 2022)

C. Nissen et al.: Abruptly attenuated carbon sequestration with Weddell Sea dense waters towards the end of the 21st century (oral)

COMFORT Annual Project Meeting (Brussels, May 2022)

C. Nissen et al.: Weddell Sea shelf-open ocean coupling and deep-ocean carbon transfer across emission scenarios: Has a tipping point been crossed by 2100? (poster)

References

Danilov, S., Wang, Q., Timmermann, R., Iakovlev, N., Sidorenko, D., Kimmritz, M., Jung, T., & Schröter, J. (2015). Finite-Element Sea Ice Model (FESIM), version 2. *Geoscientific Model Development*, 8(6), 1747–1761. <https://doi.org/10.5194/gmd-8-1747-2015>

Hauck, J., Völker, C., Wang, T., Hoppema, M., Losch, M., & Wolf-Gladrow, D. A. (2013). Seasonally different carbon flux changes in the Southern Ocean in response to the southern annular mode. *Global Biogeochemical Cycles*, 27(4), 1236–1245. <https://doi.org/10.1002/2013GB004600>

Hauck, J., Völker, C., Wolf-Gladrow, D. A., Laufkötter, C., Vogt, M., Aumont, O., Bopp, L., Buitenhuis, E. T., Doney, S. C., Dunne, J., Gruber, N., Hashioka, T., John, J., Quéré, C. Le, Lima, I. D., Nakano, H., Séférian, R., & Totterdell, I. (2015). On the Southern Ocean CO₂ uptake and the role of the biological carbon pump in the 21st century. *Global Biogeochemical Cycles*, 29(9), 1451–1470. <https://doi.org/10.1002/2015GB005140>

Karakuş, O., Völker, C., Iversen, M., Hagen, W., Wolf-Gladrow, D., Fach, B., & Hauck, J. (2021). Modeling the Impact of Macrozooplankton on Carbon Export Production in the Southern Ocean. *Journal of Geophysical Research: Oceans*, 126(12), 1–22. <https://doi.org/10.1029/2021JC017315>

Lago, V., & England, M. H. (2019). Projected Slowdown of Antarctic Bottom Water Formation in Response to Amplified Meltwater Contributions. *Journal of Climate*, 32(19), 6319–6335. <https://doi.org/10.1175/JCLI-D-18-0622.1>

Marinov, I., Gnanadesikan, A., Toggweiler, J. R., & Sarmiento, J. L. (2006). The Southern Ocean biogeochemical divide. *Nature*, 441(7096), 964–967. <https://doi.org/10.1038/nature04883>

Nissen, C., Timmermann, R., Hoppema, M., Gürses, Ö., Hauck, J. (2021). Abruptly attenuated carbon sequestration with Weddell Sea dense waters towards the end of the 21st century. *Nature Communications*, in review. <https://doi.org/10.21203/rs.3.rs-934877/v1>

Orsi, A. H., Johnson, G. C., & Bullister, J. L. (1999). Circulation, mixing, and production of Antarctic Bottom Water. *Progress in Oceanography*, 43(1), 55–109. [https://doi.org/10.1016/S0079-6611\(99\)00004-X](https://doi.org/10.1016/S0079-6611(99)00004-X)

- Rignot, E., Mouginot, J., Scheuchl, B., van den Broeke, M., van Wessem, M. J., & Morlighem, M. (2019). Four decades of Antarctic Ice Sheet mass balance from 1979–2017. *Proceedings of the National Academy of Sciences*, 116(4), 1095–1103. <https://doi.org/10.1073/pnas.1812883116>
- Semmler, T., Danilov, S., Gierz, P., Goessling, H. F., Hegewald, J., Hinrichs, C., Koldunov, N., Khosravi, N., Mu, L., Rackow, T., Sein, D. V., Sidorenko, D., Wang, Q., & Jung, T. (2020). Simulations for CMIP6 With the AWI Climate Model AWI-CM-1-1. *Journal of Advances in Modeling Earth Systems*, 12(9), 1–34. <https://doi.org/10.1029/2019MS002009>
- Timmermann, R., Wang, Q., & Hellmer, H. H. (2012). Ice-shelf basal melting in a global finite-element sea-ice/ice-shelf/ocean model. *Annals of Glaciology*, 53(60), 303–314. <https://doi.org/10.3189/2012AoG60A156>
- Timmermann, R., & Hellmer, H. H. (2013). Southern Ocean warming and increased ice shelf basal melting in the twenty-first and twenty-second centuries based on coupled ice-ocean finite-element modelling. *Ocean Dynamics*, 63(9–10), 1011–1026. <https://doi.org/10.1007/s10236-013-0642-0>
- Wang, Q., Danilov, S., Sidorenko, D., Timmermann, R., Wekerle, C., Wang, X., Jung, T., & Schröter, J. (2014). The Finite Element Sea Ice-Ocean Model (FESOM) v.1.4: formulation of an ocean general circulation model. *Geoscientific Model Development*, 7(2), 663–693. <https://doi.org/10.5194/gmd-7-663-2014>

6.19 *hbk00083*: Tipping points in the ecosystem of the ‘new Arctic’ Ocean

HLRN Project ID:	hbk00083
Run time:	I/2021 – II/2023
Project Leader:	Prof. Dr. Björn Rost ¹
Project Scientists:	Dr. Laurent Oziel
Affiliation:	Alfred Wegener Institute, Helmholtz Centre for Polar and Marine Research
	¹ principal investigator, also at the University of Bremen

Overview

This projects aims at finding possible tipping points in the Arctic Ocean ecosystem.

The vanishing summer sea-ice allows more sun light to penetrate in the water columns and therefore stimulated primary production. More nutrient assimilation by phytoplankton during photosynthesis is therefore expected such as a shift from a light-limited to a nutrient-limited ecosystem. However, Climate Change does not only affect sea-ice but also induces an increase in river runoffs and coastal erosion made of permafrost, potentially releasing use amounts or carbon and nutrients. What will be the combined effects of climate change including increased Terrigenous inputs on primary production but also the Arctic Ocean to act as a carbon sink?

➔ To answer this timely question, a total of 10 experiments were conducted thanks to HLRN/BremHLR are summarized in the following table:

Table 1: Experimental set-up: AWI-CM forcings and CO₂ concentratrion, spinup = 50 years, during of 5 times the 1950-1960 period. EXP9 is still running, all other runs are finished.

Simulations #	Forcing	Terrigeneous inputs	Coastal erosion pool	Year span
EXP-1	historical + ssp370	No	DIN, DIC	1970-2100
EXP-2	historical + ssp370	constant	DIN, DIC	1970-2100
EXP-3	historical + ssp370	varying	DIN, DIC	1970-2100
EXP-4	historical + ssp585	varying	DIN, DIC	2015-2100
EXP-5	historical + ssp126	varying	DIN, DIC	2015-2100
EXP-6	historical + ssp245	varying	DIN, DIC	2015-2100
EXP-7	historical + ssp370	varying	DON, DOC	1970-2015
EXP-8	historical + ssp370	varying	PON, POC	1970-2015
EXP-9	historical + Cram et al. 2018 parametrization.	varying	DIN, DIC	1970-2015
EXP-10	Historical (no CDOM absorption)	varying	DIN, DIC	2010-2014

Results

Key points:

- Terrigenous inputs are responsible for a ~30% increase in NPP by 2090 (in high emission scenarios ssp-370). This effect is bigger than climate change sensitivity (~17%), for example a shift from a low emission (ssp-126) scenario to a high emission scenario (ssp-370).
- Future NPP levels (+41% compared to 1970) will be characterized by a shift from a light limited to a nutrient limited system (change in limiting factor, ratios of C:N increasing, Chl:C decreasing, towards smaller phytoplankton).
- Nevertheless, the combination of climate change induced warming and increased Terrigenous inputs will intensify biogeochemical cycles of nutrients, the bottleneck of Arctic Ocean biogeochemical cycles.
- The increased Arctic Ocean NPP did not translate into a same scale increased Export Production. On the contrary, Export Production increased until the 2030s and further stagnated due to a decreased Export Efficiency and increased in Remineralization Efficiency.
- Increased remineralization was attributed to both Terrigenous inputs (+18%) and Ocean warming (+44%).

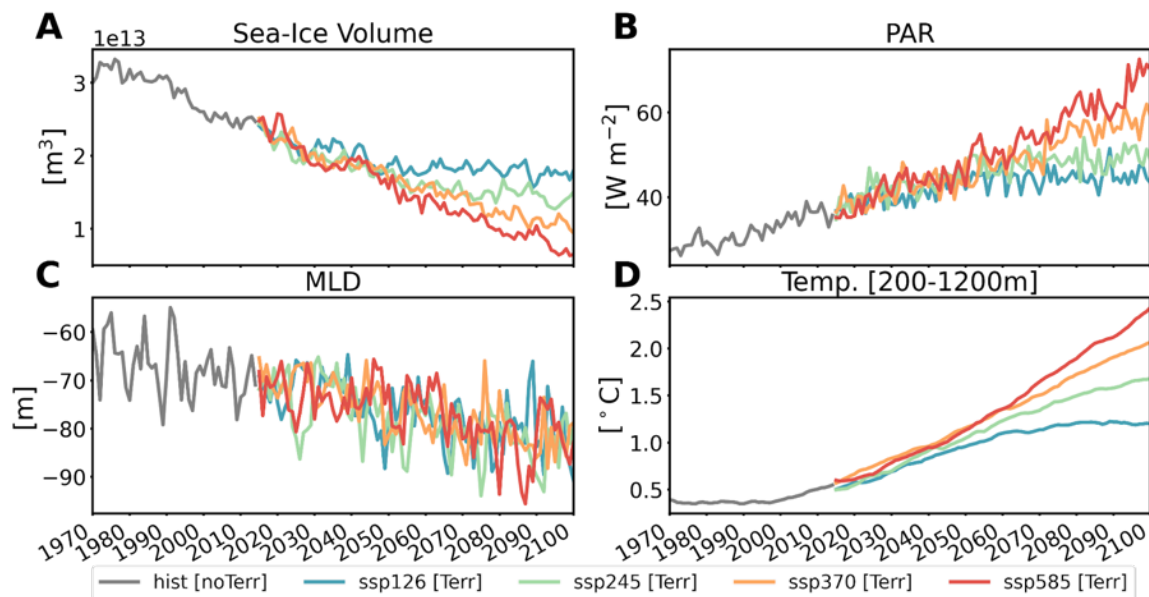


Figure 1: Time-series of environmental conditions over the Arctic Ocean during the historical [1970-2014] and forecast [2015-2100] periods with: A Sea-Ice Volume [m^3], B Photosynthetically Available Radiations [$W m^{-2}$], C Winter Mixed Layer Depth [m] and D mesopelagic (200-1200m) averaged temperature.

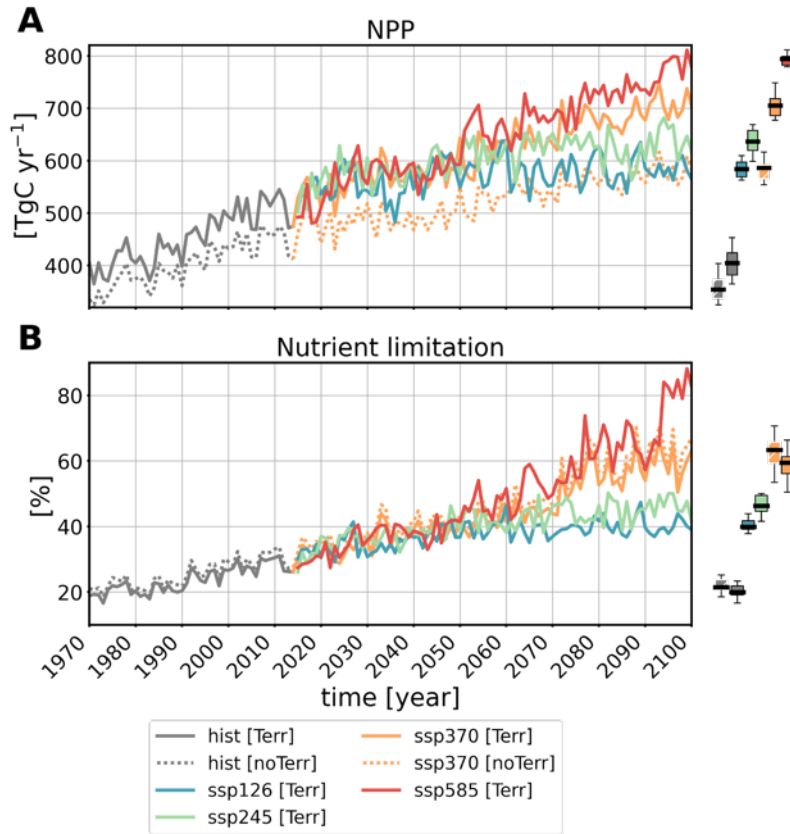


Figure 2: Time-series over the Arctic Ocean during the historical [1970-2014] and forecast [2015-2100] periods of: A Integrated Net Primary Production [Tg C year⁻¹] and B percentage of the Arctic Ocean area limited by nutrients [%]. Right hand side boxplots represent the distribution over the first historical decade (1970-1979) and the last forecast decade (

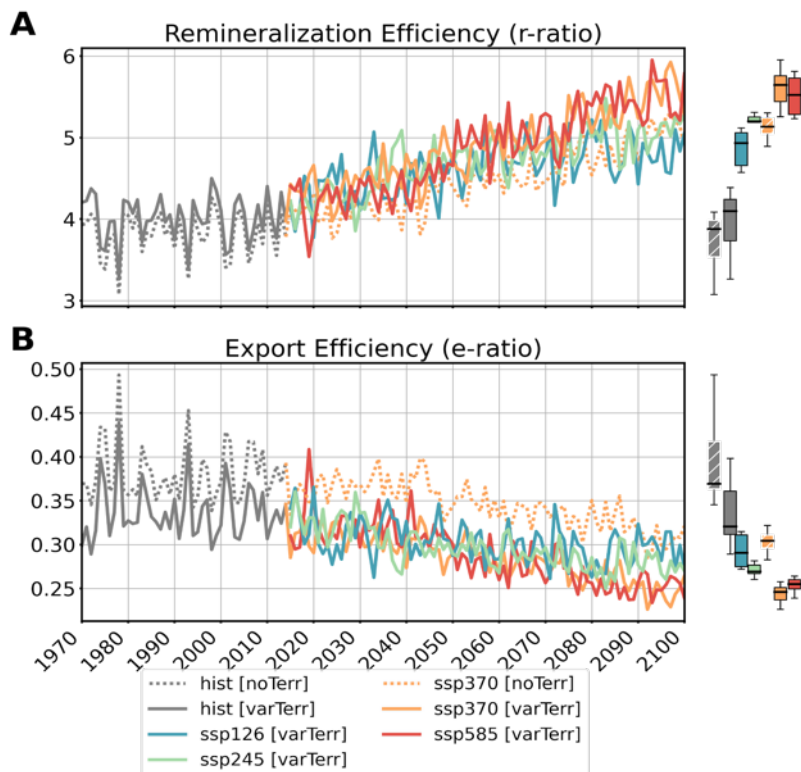


Figure 3: Time-series of metrics illustrating the evolution of the biogeochemical fluxes in the Nitrogen budget over the Arctic Ocean during the historical [1970-2014] and forecast [2015-2100] periods with: A Remineralization Efficiency (r-ratio = Remineralization / Exported Production), B Export Efficiency (e-ratio = Exported Production / Net Assimilation by phytoplankton). Right hand side boxplots represent the distribution over the first historical decade (1970-1979) and the last forecast decade (2090-2099).

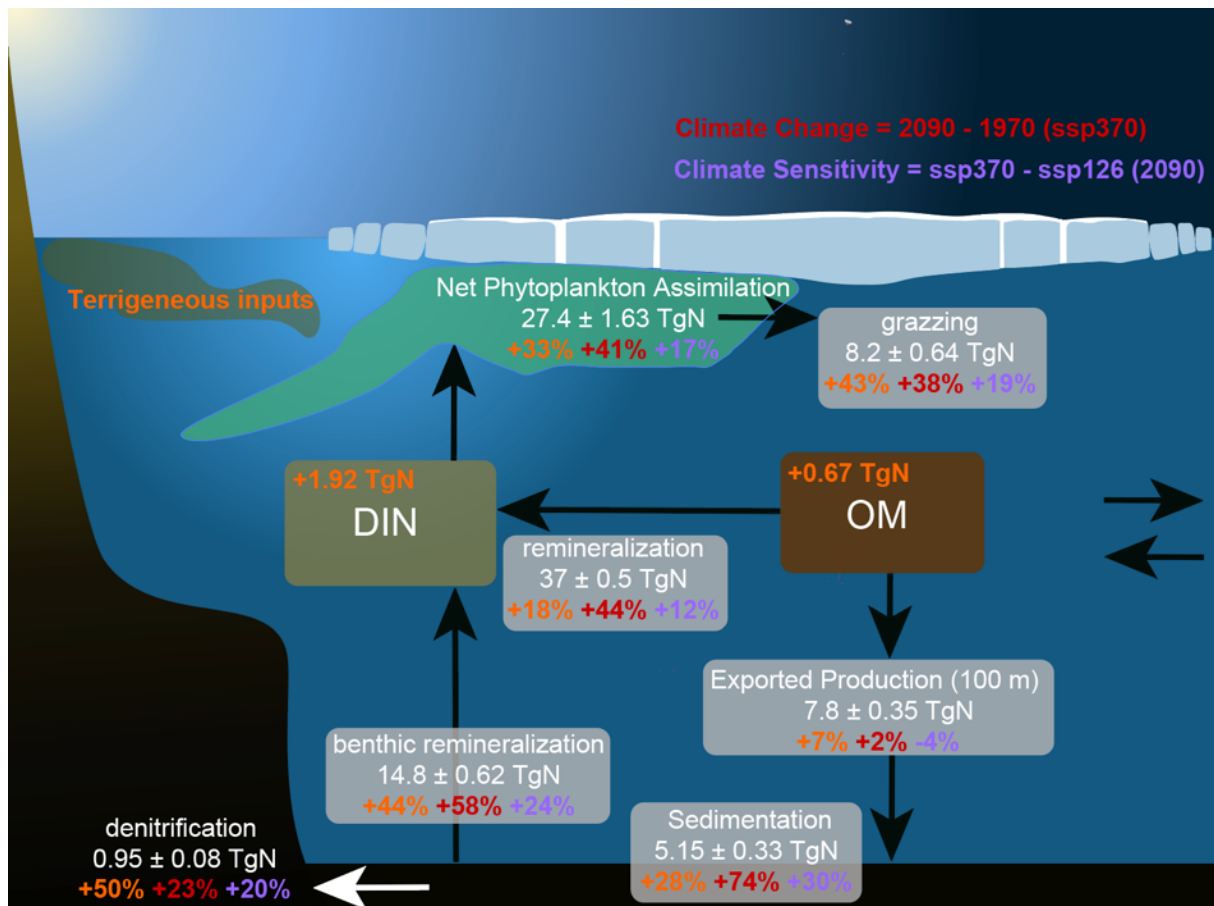


Figure 4: Simplified Arctic Ocean nitrogen budget for the decade 2090 with terrigenous inputs and ssp-270 emission scenario. All Units are in Tg N year-1. Relative Contribution of Terrigenous inputs (rivers plus coastal erosion), Climate sensitivity (ssp-370 minus ssp-126) and Climate change (2090 minus 1970, with ssp-370 emission scenario) are shown in percentage. Horizontal arrows on the right-hand side represent the physical transport with the adjacent seas.

Outlook

Finish writing manuscript to be submitted to Nature Climate Change, and supplementary analyses (EXP 7 to 10).

6.20 *hbk00084*: Marine biogenic aerosol precursors in the Arctic Ocean

HLRN Project ID:	hbk00084
Run time:	IV/2021 – III/2023
Project Leader:	Dr. Astrid Bracher
Project Scientists:	A. Bracher ¹ , M. Zeising, Ö. Gürses, J. Hauck, S. Loza, L. Oziel
Affiliation:	Alfred Wegener Institute, Helmholtz Centre for Polar and Marine Research, ¹ also at Institute of Environmental Physics, University of Bremen

Overview

Biogenic aerosols from phytoplankton production localized in leads or open water were shown to act as cloud condensation nuclei or ice nuclei in remote regions. As extensive measurements of biogenic aerosol precursors are still scarce, we conduct a modeling study and use acidic polysaccharides (PCHO) and transparent exopolymer particles (TEP) as tracers. In this project, we integrate processes of algal PCHO excretion during phytoplankton growth or under nutrient limitation and processes of TEP formation, aggregation and also remineralization into the ecosystem model REcoM2, which is coupled to the finite-volume sea ice ocean circulation model FESOM2 with a high resolution of up to 4.5 km in the Arctic. As such, we are interested in understanding the seasonal cycle as well as identifying regional hotspots of TEP production.

The results are evaluated by comparison to a set of in-situ and remote-sensing observations. Our findings will be considered to study further cloud formation processes in the Arctic realm by our collaborators within the DFG Transregional Collaborative Research Centre TR 172 Arctic Amplification: Climate Relevant Atmospheric and SurfaCe Processes and Feedback Mechanisms (AC)³.

Results

To study the seasonal cycle of biogenic aerosol precursors in the Arctic, its regional hotspots, and its impact to Arctic Amplification, we used the coupled setup of the biogeochemical Regulated Ecosystem Model version 2 (REcoM) and the general circulation and sea-ice Finite VolumE Sea-ice Ocean Model version 2.1 (FESOM). This model set-up has been optimized to provide a high resolution in the Arctic realm of state-of-the-art ocean circulation, sea ice physics and marine biogeochemistry.

The preceding efforts of the FESOM development team at AWI Climate Science division and of our developing REcoM team were of major advantage for this study. We could also profit from the project hbk00083 in the setup of the model on the HLRN HPC system and the tuning of initial model conditions. Simulations were carried out for the period 1958-2019, i.e., a total of 61 years of which the period until the year 2000 is considered as spin-up. The period of 2000-2019 was evaluated.

We focused our study on dissolved acidic polysaccharides (PCHO) and transparent exopolymer particles (TEP) as tracer for biogenic aerosol precursors. TEP production depends on the release of dissolved organic carbon (partly in form of PCHO) by phytoplankton during blooming conditions or nutrient stress, and its aggregation to particles.

Our model results suggest, so far, a clear seasonal succession of phytoplankton blooms (increased phytoplankton carbon, increased total Chlorophyll a), a release of PCHO, TEP

production and remineralization (exemplary seasonal cycle for Eastern Fram Strait in Fig. 1). Computed climatological data of total Chlorophyll a, PCHO, and TEP are in good comparison to observation data.

In early summer, TEP concentration rise first in regions with phytoplankton blooms (and subsequent aggregation of dissolved organic carbon to TEP), i.e., in Fram Strait and on the Siberian shelves. Under-ice phytoplankton blooms or release from ice-algae can result in high concentration of TEP, but these events are most likely not reproducible by FESOM2-REcoM2 because ice-algae are not explicitly simulated. During summer, elevated TEP concentrations are found in the entire Arctic Ocean, which fit in-situ observation data from several campaigns. Further, there is a gradient of TEP from the shelves towards the Arctic Ocean basins during summer. In autumn, TEP are remineralized and concentrations decline. A rise of concentration in summer and quick decline in autumn is in accordance with observation data.

A strong decrease of TEP concentration with depth is reported in the literature and observed in our simulation as well. The peak concentration values of TEP in FESOM2-REcoM2, especially regarding the surface values, might be too high. A reason could be the missing transfer of particles into the surface microlayer in our simulation. The surface microlayer is the very thin top layer of the ocean, which is not part of the model structure. TEP is positively bouyant, thus, the particles would ascend through the water column, get enriched enrichment in this layer, and probably get transferred to the atmosphere.

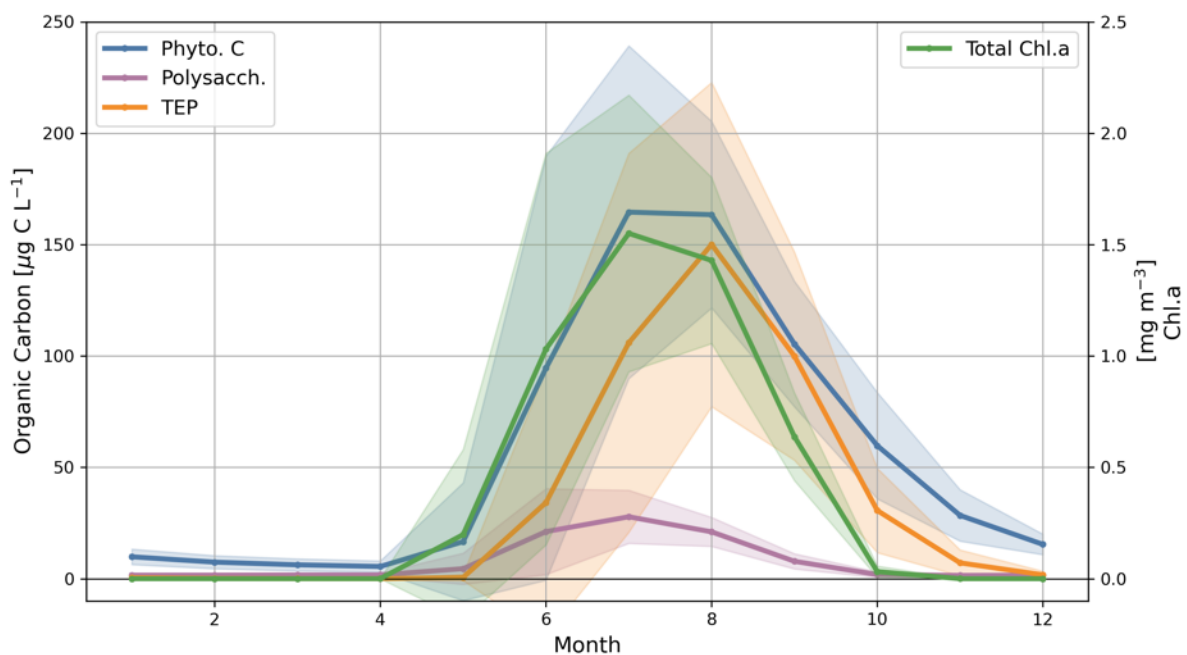


Figure 1: Seasonal cycle of organic carbon of phytoplankton (PhytoC, blue), PCHO (purple), TEP (orange), and total Chlorophyll a (TChl.a, green) of the period 2000-2019 as volume-weighted mean of the upper 30 m ocean depth, averaged over the Eastern Fram Strait. Standard deviation of the regional average is shown as shaded area in corresponding colors.

Outlook

In our research, we integrated processes of TEP formation, aggregation and also remineralization into an ocean general circulation biogeochemical model to study the production of biogenic aerosol precursors in the Arctic Ocean. Our simulation of TEP formation processes resulted in a first description of TEP on large spatial and temporal scales in the Arctic realm. A first evaluation of this description and its main drivers with in-situ and remote

sensing observation data confirmed the validity of our model approach. Still, the peak TEP concentration are high compared to observations. To test the robustness of our simulations, we want to conduct two sensitivity studies.

First, we will test the model sensitivity to TEP remineralization. We expect that a higher remineralization will reduce the maximum values of TEP concentration and be more in line with in-situ measurements. Second, we will test the sensitivity of parameter controlling the polysaccharide fraction of organic carbon released by phytoplankton. This step is important because we could estimate how much a changing phytoplankton community could alternate PCHO formation patterns, as a change in phytoplankton community is assumed to alter organic carbon release.

Publications

1. Zeising, M., Oziel, L., Guerses, O., Hauck, J., Heinold, B., Losa, S., Thoms, S., van Pinxteren, M., Völker, C., Zeppenfeld, S., and Bracher, A.: “Simulation of organic aerosol precursors from the Arctic Ocean using coupled ecosystem ocean modeling compared to in-situ and satellite observations”. In preparation for submission to JGR Biogeoscience

Presentations

2. Zeising, M., Losa, S., Hauck, J., Thoms, S., and Bracher, A. (2021). “High-Resolution Modelling of Seasonality and Spatial Distribution of Marine Organic Aerosol Precursors in the Arctic Ocean”. Poster at 3rd (AC)3 Science Conference. Potsdam, Germany.
3. Zeising, M., Oziel, L., Guerses, O., Hauck, J., Heinold, B., Losa, S., Thoms, S., and Bracher, A. (2022). “High-Resolution Modelling of Marine Biogenic Aerosol Precursors in the Arctic Realm”. Conference Talk, EGU General Assembly.

6.21 *hbk00085*: Modellierung des Einsetzens der letzten Eiszeit

HLRN-Projektkenung:	hbk00085
Laufzeit:	IV/2021 – I/2023
Projektleiter:	Prof. Dr. M. Schulz
Projektbearbeiter:	Dr. M. Prange, Dr. D. Latinovic
Institut / Einrichtung:	MARUM – Zentrum für Marine Umweltwissenschaften, Universität Bremen

Überblick

Das letzte Interglazial im Marinen Isotopenstadium (MIS) 5.5 stellt eines der wärmsten Phasen in der jüngeren Erdgeschichte dar. Für dieses Interglazial vor ca. 125 ka (tausend Jahren vor heute) wurde eine globale Mitteltemperatur von fast einem Grad Celsius über dem vorindustriellen Wert rekonstruiert. Aufgrund teilweise geschmolzener Eisschilde in Grönland und der Antarktis lag der globale Meeresspiegel mit hoher Wahrscheinlichkeit 6-9 Meter über dem heutigen Niveau. Gegen Ende des MIS 5.5, zwischen ca. 120 und 115 ka, führte Abkühlung in den hohen Breiten aufgrund veränderter Erdorbitalparameter schließlich zu einem Ende des Interglazials und dem ersten Anwachsen der Eisschilde. Dabei konnten mehrere Phasen des Einsetzens der Eiszeit rekonstruiert werden. Die sommerliche Sonneneinstrahlung nahm nach 127 ka kontinuierlich ab. Das Oberflächenwasser im subpolaren Nordatlantik begann um 122-120 ka abzukühlen, ebenso wie die Temperaturen über den Eisschilden Grönlands und der Antarktis. Die Vereisung der hohen Breiten intensivte sich zwischen 118 und 113 ka, während die atmosphärische Kohlendioxid-Konzentration erst verzögert ab ca. 115 ka abnahm. Ein deutliches Abfallen des Meeresspiegels zeigt in diesem Zeitraum signifikantes Eiswachstum über den Kontinenten an. Eisschild-Rekonstruktionen weisen dabei auf erste signifikante Vereisungen im Nordosten Kanadas und der Barents-Kara-See-Region hin.

Eine wesentliche Herausforderung für das Verständnis von Klimavariabilität auf langen Zeitskalen hängt mit Mechanismen und Rückkopplungsprozessen im Erdsystem während des Einsetzens vergangener Eiszeiten zusammen. Obgleich Klimamodelle in der Lage sind, eine Abkühlung der hohen Breiten gegen Ende des MIS 5.5 zu simulieren ist unklar, ob diese Abkühlungen hinsichtlich ihrer Stärke, räumlichen Verteilung und zeitlichen Entwicklung realistisch simuliert werden, und ob mit Eisschildmodellen gekoppelte Klimamodelle die rekonstruierten Vergletscherungen und die damit verbundenen Meeresspiegeländerungen simulieren können. Unser Ziel in diesem Projekt ist es, mit einem komplexen Klimamodell (CESM1.2; <https://www.cesm.ucar.edu>) gekoppelt an das Eisschildmodell PISM (<https://www.pism.io>) die Phase des Einsetzens der letzten Eiszeit zu simulieren und dabei wichtige Rückkopplungsprozesse zu identifizieren. Das Hauptaugenmerk soll auf dem Zeitintervall der stärksten Meeresspiegeländerung (120-110 ka) liegen.

Das Modell wird mit einer horizontalen Auflösung von ca. 2 Grad für das Atmosphären-Landmodellgitter betrieben, während das Ozean-Meereisgitter eine räumlich variable Gitterweite von ca. 1 Grad in zonaler und bis zu 0,3 Grad in meridionaler Richtung besitzt. Die vertikale Darstellung des Atmosphärenmodells umfasst 30 Schichten, der Ozean wird mit 60 Niveaus in der Vertikalen diskretisiert. Das Eisschildmodell verwendet ein 20-km-Gitter. Zur Untersuchung des raumzeitlichen Aufbauverhaltens der nordhemisphärischen Eisschilde und Wechselwirkungen mit dem Atmosphäre-Ozean-System werden transiente Simulationen durchgeführt. Mittels einer asynchronen Koppelungstechnik können rechenzeitsparende Modellläufe durchgeführt werden.

Das Projekt ist Teil der durch das BMBF-finanzierten nationalen Klimamodellierungsinitiative PalMod-II.

Ergebnisse

Eine Simulation des Intervalls 123-110 ka mit dem interaktiv gekoppelten Klima-Modell zeigt eine Vergletscherung der hohen nördlichen Breiten. Während die Eisverteilung bei 123 ka (mit grönländischem Eisschild) der heutigen recht ähnlich ist, nimmt das Eisvolumen anschließend allmählich zu, was zu einer entsprechenden Abnahme des globalen Meeresspiegels führt. Abbildung 1 zeigt die Zeitreihen einiger wichtiger integrierter Größen. Die kältesten Sommertemperaturen in den hohen Breiten zusammen mit einer maximalen Meereisausdehnung werden um 116 ka erreicht, während das maximale Eisschildvolumen bei 112 ka simuliert wird, bevor die zunehmende sommerliche Sonneneinstrahlung das Eisvolumen wieder reduziert. Bei 112 ka verteilen sich die Eismassen über den Kanadisch-Arktischen Archipel, die Baffin-Insel, die Kara-Barentssee-Region und die ostsibirischen Inseln (Abbildung 2). Aus geomorphologischen Rekonstruktionen abgeleitete Vergletscherungen in der Barents-Kara-See-Region, den Regionen Quebec-Labrador und Keewatin sowie in Skandinavien werden im Modell unterschätzt bzw. gar nicht simuliert. Verschiedene Modellparameter, die mit großen Unsicherheiten behaftet sind, werden daher zurzeit neu eingestellt, um die simulierten Vergletscherungen mit den Rekonstruktionen näher zusammenzubringen.

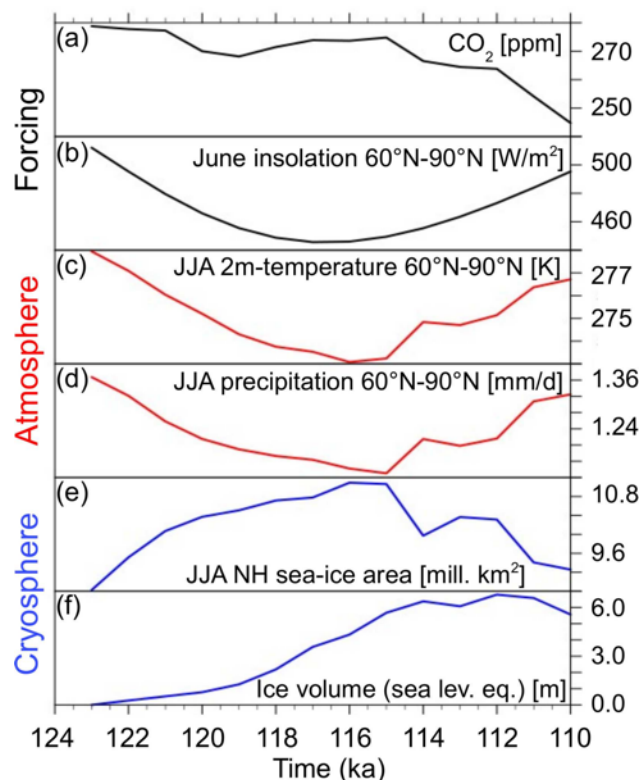


Abbildung 1: (a, b) Antriebsfaktoren der transienten Simulation zum Einsetzen der letzten Eiszeit (atmosphärische Kohlendioxid-Konzentration und Sommerinsolation). (c, d) Simulierte sommerliche Klimaänderung in hohen nördlichen Breiten (mittlere Oberflächenlufttemperatur und mittlerer Niederschlag). (e, f) Simulierte Eisänderungen (sommerliche Meereisfläche in der Nordhemisphäre und Eisvolumen als Meeresspiegeläquivalent).

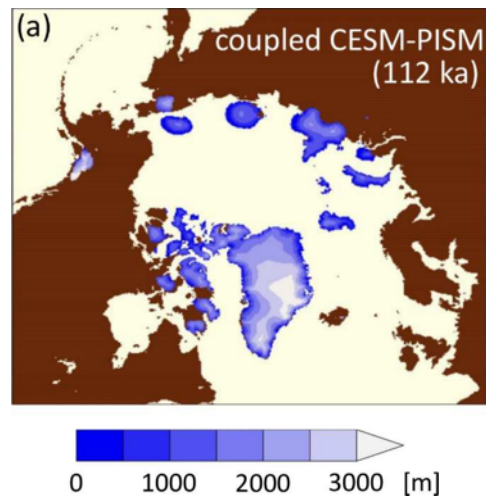


Abbildung 2: Simulierte Höhe der Eisoberfläche zum Zeitpunkt 112 ka.

Ausblick

Es konnte gezeigt werden, dass das gekoppelte Klima-Eisschild-Modell CESM-PISM prinzipiell in der Lage ist, ein hauptsächlich orbitalgetriebenes Einsetzen der letzten Eiszeit zu simulieren. Im Detail wurden jedoch Unterschiede zwischen der rekonstruierten und der simulierten Eisverteilung identifiziert. Eine Neukalibrierung bestimmter Modellparameter soll Diskrepanzen der Simulationen gegenüber Rekonstruktionen reduzieren.

Publikationen

I. Obrecht, D. De Vleeschouwer, L. Wörmer, M. Kucera, D. Varma, M. Prange, T. Laepple, J. Wendt, S. D. Nandini-Weiss, H. Schulz, K.-U. Hinrichs, *Last Interglacial decadal sea surface temperature variability in the eastern Mediterranean*, *Nature Geoscience*, 15, 812-818 (2022).

6.22 *hbk00087*: Arctic Amplification in the Barents Sea: Evaluation of an Ice-Ocean-Atmosphere Feedback in a Coupled Climate Model

HLRN Project ID: hbk00087
 Run time: Q4/2021 – Q4/2022
 Project Leader: Prof. Dr. Torsten Kanzow
 Project Scientists: M.Sc. Finn Heukamp, Dr. Claudia Wekerle, Dr. Qiang Wang
 Affiliation: Alfred-Wegener-Institute Helmholtz Centre for Polar and Marine Research

Overview

The ongoing warming of the Arctic during the last decades is unprecedented and approx. twice as strong as the global average, resulting in enormous changes in the ocean, atmo-/cryo-/ and biosphere. Despite the large efforts being made in the scientific community, the strong warming known as 'Arctic Amplification' is not yet fully understood. It is assumed that undiscovered local, positive feedback mechanisms contribute to the strong warming of the Arctic.

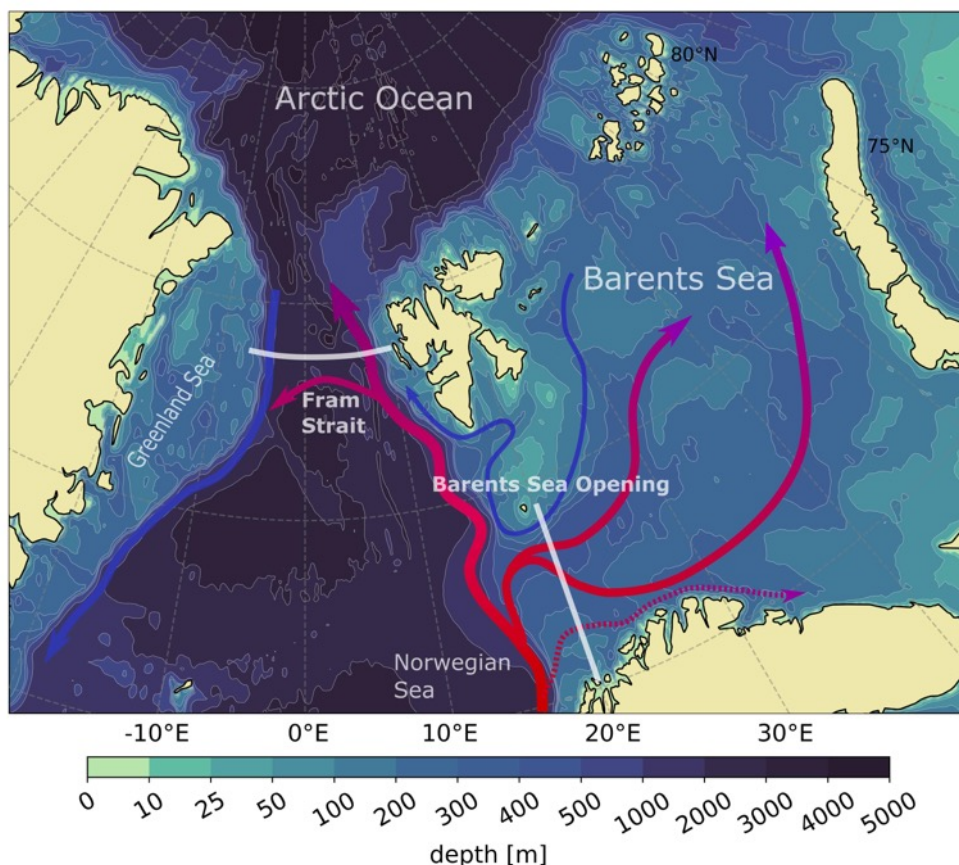


Figure 1: Atlantic Water flow into the Arctic via Fram Strait and the Barents Sea.

In this project we investigated a feedback mechanism in the coupled climate system of the Arctic, in particular the Barents Sea, that could act as a yet undiscovered but crucial driver of Arctic Amplification. In order to achieve this, we performed global simulations of ocean and sea ice with the latest release of the Finite Volume Sea Ice and Ocean Model (FESOM2.1), a

state-of-the-art ocean and sea ice model. The planned simulations included (I) spinup experiments to prepare the model configurations for the planned experiments, (II) reference simulations, and (III) perturbation experiments in which local anomalous cyclonic wind fields are added to assess the impact of local winds on the Barents Sea heat budget and Atlantic Water transport.

As the simulations were computationally extensive, they were heavily relying on computing resources from HLRN.

Results

The investigated feedback, possibly contributing to Arctic Amplification is visualized in Figure 2. An initial positive perturbation in the AW heat transport towards the BS leads to a warmer BS, which requires more cooling before it reaches the freezing point, such that less winter sea ice is formed, and there is a larger temperature contrast between the cold air and the warm ocean. As a consequence, there is increased net surface heat loss from the ocean to the atmosphere. The increased surface heat loss warms the lower atmosphere and leads to a local reduction in surface pressure. The resulting cyclonic circulation anomaly produces strong westerly winds over the BSO that fosters additional AW transport into the BS, closing the positive feedback loop.

Due to unexpected problems with porting the proposed model (AWICM3) onto the HLRN system, we conducted our experiments with the ocean and sea ice model FESOM2.1 instead of AWI-CM3. Instead of investigating the full feedback, we thus focused our work on the relation between changes in the local wind field as a consequence of winter sea ice loss in the Barents Sea and associated modifications of the Atlantic Water transport through the Barents Sea Opening (Figure 2d-e). We thus added cyclonic wind anomalies to the atmospheric forcing of our model and monitored modifications of the Atlantic Water transport through the Barents Sea Opening. All other components of the proposed feedback mechanism were further investigated and validated in reanalysis data.

The perturbation experiments revealed that in the current climate condition the proposed feedback is most likely not operating. We conducted several perturbation experiments with cyclonic wind anomalies added to the forcing of the model, based on various atmosphere reanalysis products (JRA55, ERA5, NCEP-CORE2, ERAinterim). The reanalysis products were investigated with a special focus on air pressure and wind changes as a result of local sea ice retreat in the Barents Sea prior to the experiments. All perturbation experiments, however, did not reveal changes in the Atlantic Water transport which could be attributed to the wind anomalies added. As all experiments were conducted with slightly different wind anomalies (magnitude and shape) but had a similar outcome, we consider our results as a robust proof to reject our initial feedback hypothesis. Our study further showed that the westward directed flow of cold Polar Water and modified Atlantic Water at the slope of Bear Island is sensitive to the wind anomalies which we added to the model forcing. Changes in the volume flux of this watermass do, however, hardly affect the heat budget of the Barents Sea as it is very cold (ca. -2°C) and does not contribute to the melting of sea ice.

While our experiments did not reveal any sensitivity of the Atlantic Water branch in the Barents Sea on local cyclonic wind anomalies, we observed modifications in the second Atlantic Water branch through Fram Strait as a consequence of the modified wind forcing. The changes included a downslope shift of the West Spitsbergen Current, a southward shift of the Atlantic Water recirculation in Fram Strait and a cooling of waters on the east Greenland shelf. We were thus able to propose a mechanism originating from atmosphere variability in the Barents Sea that contributes to controlling the location of the Atlantic Water recirculation in Fram Strait. This specific relation has not been described before.

Outlook

Especially the observed mechanism controlling the location of the Atlantic Water recirculation in Fram Strait and the dependence of the westwards directed current south of Bear Island are attractive for future research.

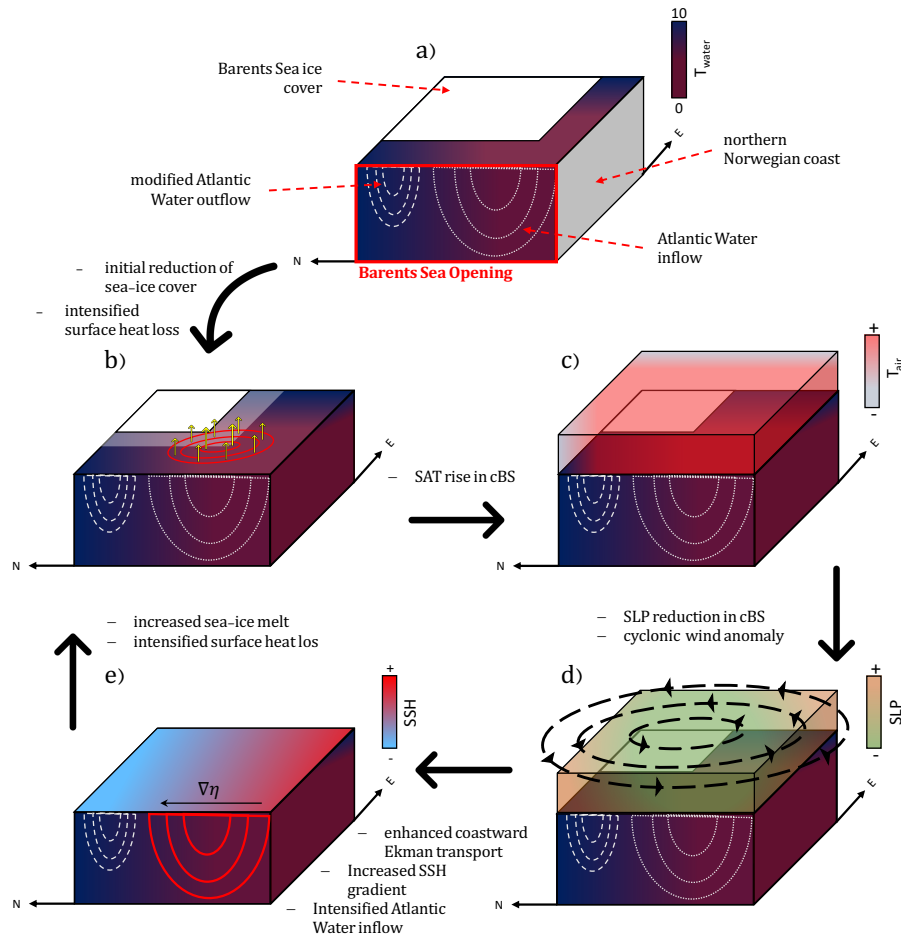


Figure 2: Schematic of the Barents Sea wind feedback. Abbreviations: sea level pressure (SLP), surface air temperature (SAT), central Barents Sea (cBS), sea surface height (SSH). In this study we rejected this previously hypothesized feedback using model simulations.

The results of the experiments propose that sea ice retreat and related wind changes in the northern Barents Sea - as a consequence of global warming - might be driving temperature changes on the Greenland shelf via impacting the Atlantic Water recirculation in Fram Strait. Temperatures on the Greenland shelf are further important for the melt rates of glaciers.

Publications

1. Heukamp et al. (accepted), Impact of Cyclonic Wind Anomalies Caused by Massive Winter Sea Ice Retreat in the Barents Sea on Atlantic Water Transport towards the Arctic: A Model Study, *JGR_Oceans*.

Presentations

1. Heukamp et al. (2022), Investigations on the coupling of the Barents Sea sea-ice retreat on the Atlantic Water inflow via an ocean-ice-wind feedback in the context of Arctic Amplification (EGU General Assembly 2022, <https://doi.org/10.5194/egusphere-egu22-10191>)

6.23 **hbk00090: Paleoclimate Applications of Mixing Parameterizations in an Earth System Model**

HLRN Project ID:	hbk00090
Run time:	III/2022 – I/2023
Project Leader:	Prof. Dr. Michael Schulz, Dr. André Paul
Project Scientists:	Heves Pilatin, Siva Kattamuri
Affiliation:	MARUM – Center for Marine Environmental Sciences, University of Bremen

Objective

Studying past climates provide insights into the Earth's history and the changes in the dynamics of climatic processes through time. This builds a bridge between the past and present-day, which helps to have a better understanding of the natural variations in the global climate system and to improve the climate projections for the future. In this project, we are interested in the impact of ocean circulation and biogeochemical processes on the climatic conditions of two different time intervals: The Last Glacial Maximum (~21 ka) and mid-Cretaceous (~90 Ma).

Scientific Background

The **Last Glacial Maximum** is the most recent glacial period when the ice sheet coverage was at its greatest extent (8% of Earth's surface), and the atmospheric carbon dioxide (pCO₂) level was ~190 ppm. During this period, even though the bathymetry was very similar to the present day, the continental shelves were exposed, and the global-mean sea level was lower by ~130 m compared to today due to the increase in ice volume [3]. This project hypothesizes that a decrease in sea level caused tidal-energy dissipation to shift from the shelves to the open ocean resulting in enhanced vertical mixing in the deep ocean.

The **mid-Cretaceous** (~90 Ma) is a geological period with warmer global temperatures compared to the present day due to higher atmospheric CO₂ concentration. The continental configuration was different and the global mean sea level was much higher compared to the present day. The locations of deep water formation and upwelling are also different thus changing the whole pattern of general circulation as we know it. The objective is to investigate the effect of boundary conditions and geographical configurations on the general ocean circulation by using state-of-the-art climate modelling.

Although the climatic conditions (e.g., temperature, GHG emissions, albedo), sea levels, continental configurations as well as vegetation are very different for the LGM and mid-Cretaceous, the paleo records from both periods demonstrate low oxygenation in the deep ocean (deoxygenation during the LGM [1], near anoxic conditions during the mid-Cretaceous). Our project aims to provide a much more realistic representation of the ocean circulation, the carbon and oxygen availability in the interior ocean, consistent with the proxy data, during LGM and mid-Cretaceous by using an energetically consistent vertical mixing scheme, Internal Wave Dissipation, Energy, and Mixing (IDEMIX), in the fully coupled isotope-enabled Earth System Model (iCESM1.2).

IDEMIX module is developed to estimate the diapycnal diffusivity induced by the breaking of internal gravity waves, and it is driven by two forcing factors: wind-driven near-inertial waves (NIWs) at the surface boundary and the baroclinic tides at the bottom boundary layer of the ocean interior [2]. However, this study focuses on only tidal-induced mixing. Hence, tides are

considered as the only source for generating internal waves in IDEMIX parameterisation. In our model setup, we use both the K-Profile (the default vertical parameterisation of the POP model) and the IDEMIX together, the "KPP+IDEMIX" approach. While the KPP scheme is activated only in the mixed layer (up to ~ 1 km), IDEMIX is applied only to the interior ocean (> 1 km), where dissipation is generated by the tidal forcing at the ocean floor.

We started our project by doing the sensitivity experiments of the IDEMIX in the LGM simulations. Since the modal bandwidth tuning parameter (j_\star) in IDEMIX determines the number of excited vertical modes, which affects how fast the energy propagates from the bottom to the upper ocean [2], we aim to investigate its impact on the vertical mixing and the ocean state and find the optimal j_\star value for the main simulations of LGM.

Results:

Evaluating the performance of j_\star on the LGM simulations

a) on the Tidal Dissipation Rate:

The preliminary results show that j_\star mainly influences energy levels and dissipation rates. As the j_\star value gets smaller, the vertical group velocity of the waves and the energy transferred to the upper ocean increases. The tidal dissipation rate maps in Figure 1 demonstrate this relation. The model with a lower j_\star value (5) vertically propagates more energy from deeper to upper depths than with a higher j_\star (10). The gap between these simulations is minimum at the surface and increases through the deep ocean due to the presence of IDEMIX under 1 km. Although both have the same spatial dissipation pattern on the global ocean, the change in j_\star value has a significant impact on the mixing strength at the deep convection regions. The tidal mixing at the subpolar North Atlantic (the Greenland Sea and the Labrador Sea) and near the Antarctic Peninsula in the Southern Hemisphere (> 1 km) is one to two orders of magnitude higher in the simulation with $j_\star = 5$ than $j_\star = 10$.

b) on the Potential Temperature and Salinity:

The potential temperature along 30.4W in Figure 2 represents a much colder and stratified ocean for the LGM than the PI (pre-industrial, 1850) run. Similar to temperature, the salinity gradient on the same longitude provides homogenous density over the depth for the PI. Yet, the stratification is strong, and the ocean is much denser (saltier) during LGM.

Even though j_\star is not directly considered for its impact on the seawater density, it could be an important parameter for the vertical transport of heat and salt flux due to the turbulent mixing. This impact can be seen in the cross-sectional plots of the salinity gradient of LGM simulations in Figure 2. The model with $j_\star = 5$ spreads denser water masses through the surrounding vertical levels. The saline water in the Southern Ocean (~ 36.6 g/kg) is carried from the deep to intermediate depths with strong tidal mixing at the same region.

Outlook

Currently, we continue our sensitivity experiments with two LGM and one control run (PI). So far, we achieved to complete 236 years. However, we still need 1500 years of simulation for the carbon isotopes to reach near equilibrium. Then, we will start doing our main simulations with the optimal j_\star value of LGM, based on the results of the sensitivity analyses, for an additional 2000 years. We expect to obtain a much more stable Meridional Overturning Circulation and realistic oxygen and carbon budget (consistent with the proxy data) at least after 2500 years.

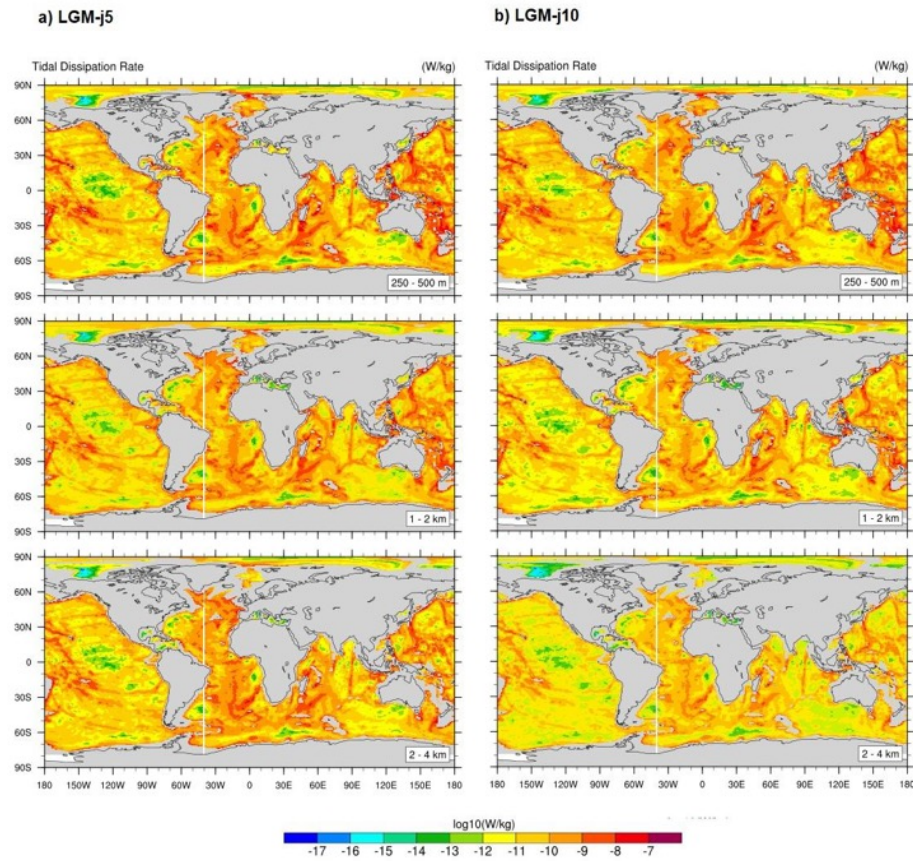


Figure 1: LGM Tidal Dissipation Rate (W/kg) over different depth ranges a) $j_{\star} = 5$, b) $j_{\star} = 10$.

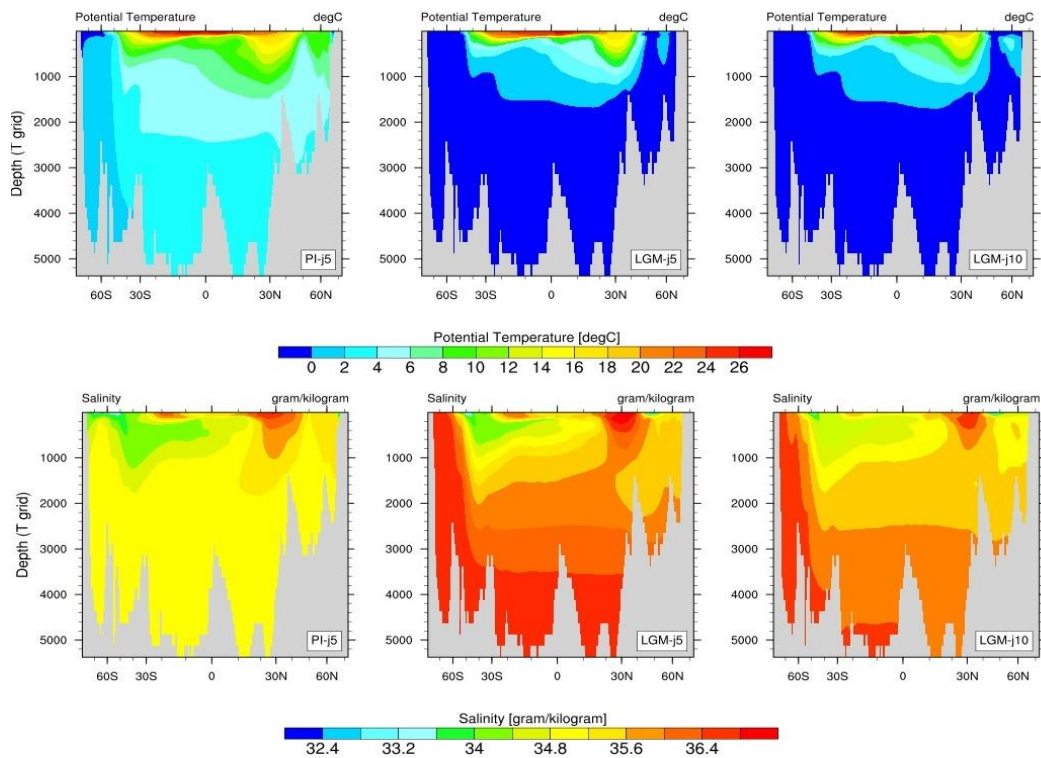


Figure 2: Cross section of potential temperature (degC) and salinity (g/kg) along 30.4W.

The compute project was granted in a limited capacity to study the applications of the IDEMIX scheme for the LGM subproject. Reflecting on the successful and interesting initial results we achieved, we want to extend the study to the other subproject with the mid-Cretaceous geological period. We hope to do that with an application to extend the compute project for the next year focusing on studying the mid-cretaceous natural greenhouse earth with the KPP+IDEMIX parameterisation.

References:

- [1] Jaccard, S. L. & Galbraith, E. D. (2012). Large climate-driven changes of oceanic oxygen concentrations during the last deglaciation. *Nat. Geosci.* 5(2), 151–156. doi:10.1038/ngeo1352
- [2] Olbers, D.J., Eden, C. (2013). A Global Model for the Diapycnal Diffusivity Induced by Internal Gravity Waves. *Journal of Physical Oceanography*, 43, 1759-1779. doi: <https://doi.org/10.1175/JPO-D-12-0207.1>
- [3] Tarasov, L., Dyke, A. S., Neal, R. M., and Peltier, W. R.: A data-calibrated distribution of deglacial chronologies for the North American ice complex from glaciological modelling, *EPSL*, 315–316, 30-40, <https://doi.org/10.1016/j.epsl.2011.09.010>, 2012

6.24 **hbk00094: The effects of Ocean Alkalinity Enhancement on the anthropogenic CO₂ concentrations in the 21st century**

HLRN Project ID:	hbk00094
Run time:	III/2022 – II/2023
Project Leader:	Prof. Dr. Björn Rost ¹
Project Scientists:	Tanvi Nagwekar ² , Dr. Cara Nissen, Dr. Judith Hauck
Affiliation:	Alfred Wegener Institute, Helmholtz Center for Polar and Marine Research, Bremerhaven, Germany.

¹principal investigator, also at the University of Bremen,

²project administrator

Overview

The rise in atmospheric CO₂ concentrations due to burning of fossil fuels and land use change leads to elevated global temperature causing detrimental changes in the climate. Without reduction and control in the carbon emissions, global temperature will exceed the Paris Agreement's 2°C limit (UNFCCC, 2015). Hence, to limit temperature increases and mitigate climate change, significant carbon emission reductions and exploration of various Carbon Dioxide Removal (CDR) methods are necessary (Friedlingstein et al., 2011). The oceans are a large carbon reservoir as CO₂ dissolves in and reacts with seawater (Zeebe and Wolf-Gladrow, 2001), and they act as a sink for anthropogenic CO₂ emissions (Gruber et al., 2019). The Southern Ocean and the North Atlantic are of critical importance as the formation of intermediate, deep and bottom waters occurs there, which is the bottle-neck of ocean carbon uptake. The subducting water masses in these regions can sequester carbon in the interior ocean on decadal to millennial timescales (Gruber et al., 2019; Sarmiento & Gruber, 2002).

Owing to the importance of the oceans in global carbon cycling, various marine CDR methods are being actively assessed. One such method is Ocean Alkalinity Enhancement (OAE; Hartmann et al., 2013). Alkalinity is the excess of proton donors, and higher alkalinity facilitates more oceanic CO₂ uptake (Wolf-Gladrow et al., 2007). The rate at which CO₂ is naturally drawn down by the oceans due to its buffer capacity as a result of silicate rock weathering is two orders of magnitude too slow to compensate the current emission rates (Bach et al., 2019). Hence, the idea behind OAE is to accelerate this natural CO₂ uptake of the oceans by enhancing alkalinity through dissolution of processed alkaline minerals e.g., olivine or calcium carbonate (Hauck et al., 2016; Keller et al., 2014; Köhler et al., 2013). In response to the OAE, the carbonate system's equilibria are shifted, promoting the conversion of dissolved CO₂ into bicarbonate ions, thereby reducing the partial pressure of CO₂ at the sea surface which increases the influx of CO₂ from the atmosphere into the ocean (Hauck et al., 2013; Wolf-Gladrow et al., 2007).

In this project, our goal is to assess the efficiency of OAE with olivine dissolution in deep and bottom water formation areas in the Southern Ocean, Labrador Sea and the Norwegian Sea in comparison to the efficiency of global OAE, using FESOM2.1-REcoM3 simulations (Hauck et al., 2020; Scholz et al., 2019) forced with atmospheric output from the AWI Climate Model under the high-emission scenario SSP3-7.0 (Semmler et al. 2020). We run the OAE simulations in a setup with high resolution ~10 km in deep and bottom water formation regions.

Results

Over the past year, we have completed all the changes in the model code which were necessary for implementing OAE. The usage of the high-resolution mesh aids us to better understand the ocean dynamics in the polar oceans, which are the focus of our regional OAE experiments. This helps to study the impact of small-scale processes on ocean carbon uptake compared to simulations already carried out on a coarse resolution mesh. First, we ran 104 years of physics-only spin-up on the high-resolution mesh. The drift in the circulation was assessed by quantifying the volume transport across e.g., the Drake Passage which reached a quasi-steady state within 100 years. We interpolated the biogeochemical fields from an existing spin-up of 150 years on a coarse resolution mesh to the high-resolution mesh. With these initial conditions, we started the historical run from 1950-2014 (still on-going, Figure 1a). Considering the first 40 years from the ongoing historical run as further spin-up time, physical and biogeochemical tracers will have experienced a total of 144 and 40 years of spin-up on the high-resolution mesh, respectively, for the upcoming future scenario simulation from 2015-2100. The OAE experiments will be branched off in 2030.

Global air-sea CO₂ fluxes are comparable between the two setups (high versus low resolution) except for the first decade due to initial adjustment to the high-resolution setup (Figure 1a). Both setups show similar spatial patterns (Figure 1b and c), but regional differences exist. For instance, the Southern Ocean CO₂ uptake is higher by 0.14 PgC yr⁻¹ in the coarse resolution than the high-resolution setup, but this seems to be partly compensated by stronger uptake (by 0.05 PgC yr⁻¹) in the North Atlantic for the high-resolution setup in the last decade of simulation.

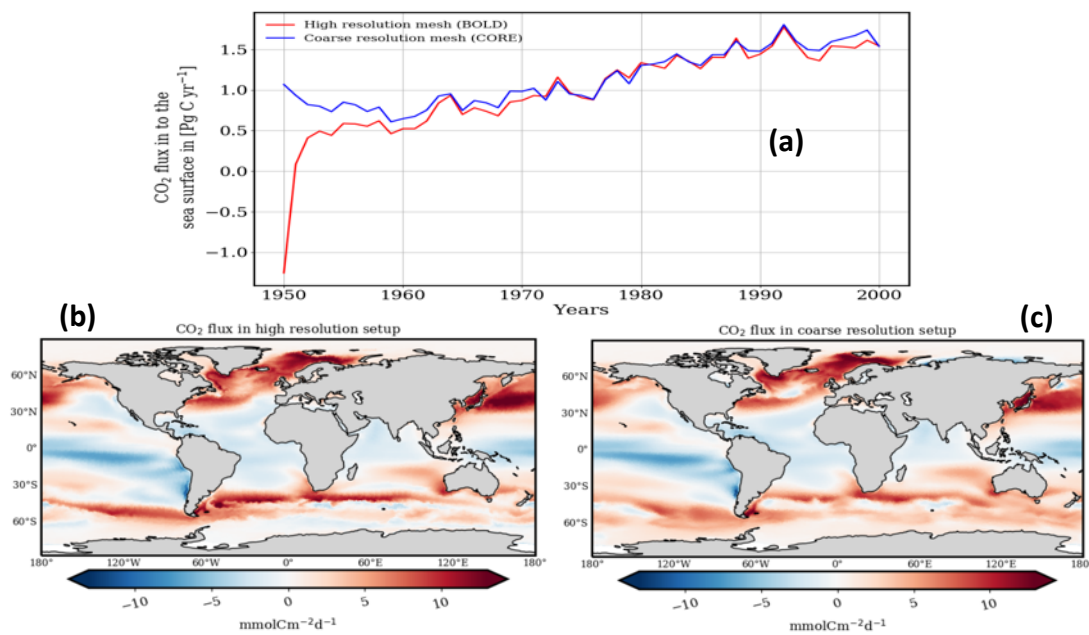


Figure 1: (a) Timeseries of the air-sea CO₂ flux (Pg C yr⁻¹) for the historical run carried out in a high resolution (red line) and coarse resolution (blue line) setup. (b and c) CO₂ flux (mmol C m⁻² d⁻¹) averaged over 1990-2000 of the historical runs in the high resolution (left) and the coarse resolution (right) setup. CO₂ flux into the sea surface (positive; red regions), CO₂ flux outgassing (negative; blue regions).

Next, in order to identify the subduction regions in the high-resolution simulation, we applied the Water Mass Transformation (WMT) Framework (Nissen et al., 2022; Pellichero et al., 2018) in the Southern Ocean, the Labrador Sea and the Norwegian Sea. We used surface buoyancy fluxes of heat and freshwater decomposed into the contribution from evaporation minus precipitation (e-p) and sea ice from the historical run (1970-1999). Figure 2a depicts the Water Mass Formation (WMF) rate as a function of surface density that results from the WMT analysis

for the Southern Ocean. Subduction (positive WMF) occurs in the density bins $< 36.2 \text{ kg m}^{-3}$ due to evaporation minus precipitation (e-p; dark blue bars) and in the density bins $> 36.8 \text{ kg m}^{-3}$ due to sea ice formation (light blue bars). Buoyancy-induced upwelling (negative WMF; blue region) occurs in the density bins $36.2\text{-}36.8 \text{ kg m}^{-3}$. These isopycnal outcrops are used to locate the subduction regions in the Southern Ocean (red in Figure 2b). Figure 2c shows the overall regional olivine deposition mask which results from applying the WMT framework to all focus regions and uniformly deposits 0.35 Pg olivine per year in subduction regions (red) for the regional OAE simulations.

Compared to the WMT analysis with the historical run on a coarse resolution setup (not presented here), the high-resolution set-up shows lower water mass subduction rate in the Southern Ocean by 1-2 Sv, while both setups have comparable rates ($1.5\text{-}2 \text{ Sv}$) in the North Atlantic. Isopycnal outcrops vary in both setups by $0.1\text{-}0.2 \text{ kg m}^{-3}$, resulting in differences in the areas of subduction regions due to their varied spatial locations. The high-resolution set-up has a 56% larger area of subduction regions for olivine deposition than the coarse resolution setup.

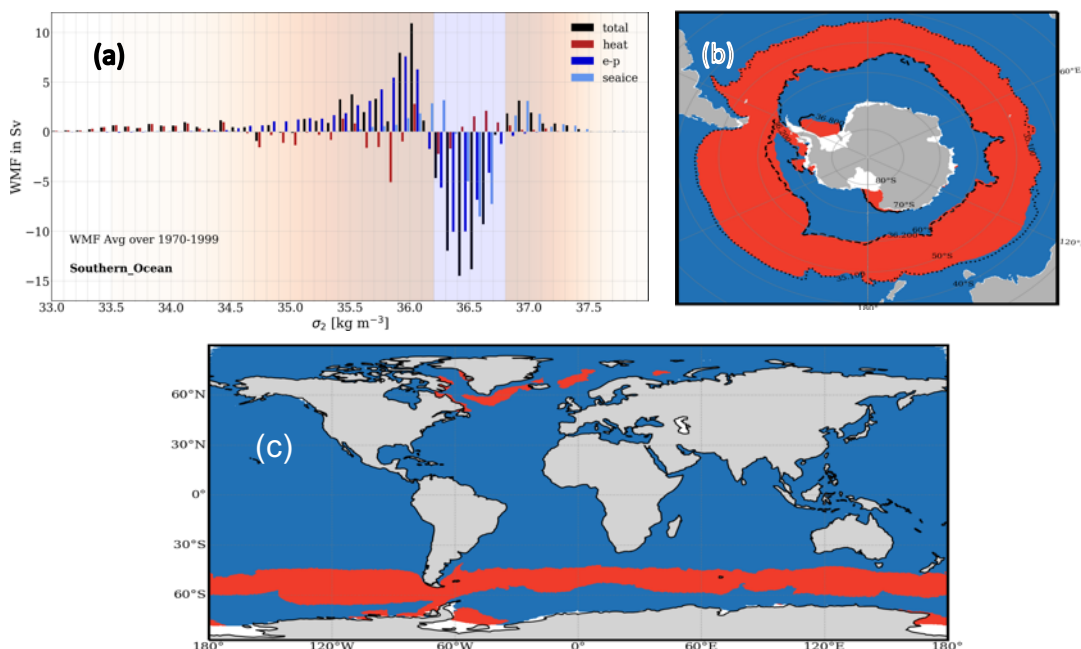


Figure 2: Water Mass Formation (WMF) rates for the Southern Ocean south of 40°S as derived from surface buoyancy fluxes for the period 1970-1999 from the historical run on the high-resolution mesh. **(a)** Annual mean WMF in Sv (black bars) integrated in 0.1 kg m^{-3} density bins and decomposed into the contribution from heat fluxes (red bars), evaporation minus precipitation (e-p, dark blue bars) and sea ice (light-blue bars). Density intervals with positive WMF correspond to regions of subduction and are shaded in red, and regions with negative WMF correspond to upwelling and are shaded in blue. **(b)** Outcrop of the isopycnals 36.8 kg m^{-3} (solid line), 36.2 kg m^{-3} (dashed line) and 35.1 kg m^{-3} (dotted line) that were identified to separate regions with subduction (red) from those with upwelling (blue) in the Southern Ocean. **(c)** Regional olivine deposition mask. Subduction/downwelling (red) regions are plotted using the isopycnal outcrops obtained from the WMF analysis carried out in the Southern Ocean, Labrador Sea and the Norwegian Sea. Overall, 0.35 Pg olivine per year is deposited using this regional mask.

Outlook

After completing the historical simulation, we will perform future scenario simulations under the high emission scenario SSP3-7.0 for the period 2015-2100. We will branch off the global and regional OAE experiments in 2030.

Publications and Presentations

Additional model experiments and the analysis of completed experiments are on-going, therefore there is no publication or presentation of the results yet.

References:

- Bach, L. T., Gill, S. J., Rickaby, R. E. M., Gore, S., & Renforth, P. (2019). CO₂ Removal With Enhanced Weathering and Ocean Alkalinity Enhancement: Potential Risks and Co-benefits for Marine Pelagic Ecosystems. *Frontiers in Climate*, 1. <https://www.frontiersin.org/articles/10.3389/fclim.2019.00007>
- Friedlingstein, P., Solomon, S., Plattner, G.-K., Knutti, R., Ciais, P., & Raupach, M. R. (2011). Long-term climate implications of twenty-first century options for carbon dioxide emission mitigation. *Nature Climate Change*, 1(9), Article 9. <https://doi.org/10.1038/nclimate1302>
- Gruber, N., Clement, D., Carter, B. R., Feely, R. A., van Heuven, S., Hoppema, M., Ishii, M., Key, R. M., Kozyr, A., Lauvset, S. K., Lo Monaco, C., Mathis, J. T., Murata, A., Olsen, A., Perez, F. F., Sabine, C. L., Tanhua, T., & Wanninkhof, R. (2019). The oceanic sink for anthropogenic CO₂ from 1994 to 2007. *Science*, 363(6432), 1193–1199. <https://doi.org/10.1126/science.aau5153>
- Hartmann, J., West, A. J., Renforth, P., Köhler, P., De La Rocha, C. L., Wolf-Gladrow, D. A., Dürr, H. H., & Scheffran, J. (2013). Enhanced chemical weathering as a geoengineering strategy to reduce atmospheric carbon dioxide, supply nutrients, and mitigate ocean acidification: ENHANCED WEATHERING. *Reviews of Geophysics*, 51(2), 113–149. <https://doi.org/10.1002/rog.20004>
- Hauck, J., Köhler, P., Wolf-Gladrow, D., & Völker, C. (2016). Iron fertilisation and century-scale effects of open ocean dissolution of olivine in a simulated CO₂ removal experiment. *Environmental Research Letters*, 11(2), 024007. <https://doi.org/10.1088/1748-9326/11/2/024007>
- Hauck, J., Völker, C., Wang, T., Hoppema, M., Losch, M., & Wolf-Gladrow, D. A. (2013). Seasonally different carbon flux changes in the Southern Ocean in response to the southern annular mode. *Global Biogeochemical Cycles*, 27(4), 1236–1245. <https://doi.org/10.1002/2013GB004600>
- Keller, D. P., Feng, E. Y., & Oeschler, A. (2014). Potential climate engineering effectiveness and side effects during a high carbon dioxide-emission scenario. *Nature Communications*, 5(1), 3304. <https://doi.org/10.1038/ncomms4304>
- Köhler, P., Abrams, J. F., Völker, C., Hauck, J., & Wolf-Gladrow, D. A. (2013). Geoengineering impact of open ocean dissolution of olivine on atmospheric CO₂, surface ocean pH and marine biology. *Environmental Research Letters*, 8(1), 014009. <https://doi.org/10.1088/1748-9326/8/1/014009>
- Nissen, C., Timmermann, R., Hoppema, M., Gürses, Ö., & Hauck, J. (2022). Abruptly attenuated carbon sequestration with Weddell Sea dense waters by 2100. *Nature Communications*, 13(1), Article 1. <https://doi.org/10.1038/s41467-022-30671-3>
- Pellichero, V., Sallée, J.-B., Chapman, C. C., & Downes, S. M. (2018). The southern ocean meridional overturning in the sea-ice sector is driven by freshwater fluxes. *Nature Communications*, 9(1), 1789. <https://doi.org/10.1038/s41467-018-04101-2>
- Sarmiento, J. L., & Gruber, N. (2002). Sinks for Anthropogenic Carbon. *Physics Today*, 55(8), 30–36. <https://doi.org/10.1063/1.1510279>
- Scholz, P., Sidorenko, D., Gurses, O., Danilov, S., Koldunov, N., Wang, Q., Sein, D., Smolentseva, M., Rakowsky, N., & Jung, T. (2019). Assessment of the Finite-volume Sea ice-Ocean Model (FESOM2.0) – Part 1: Description of selected key model elements and comparison to its predecessor version. *Geoscientific Model Development*, 12(11), 4875–4899. <https://doi.org/10.5194/gmd-12-4875-2019>
- UNFCCC. (2015). *United Nations Framework on Climate Change (UNFCCC): Adoption of the Paris Agreement, 21st Conference of the Parties*. <https://unfccc.int/resource/docs/2015/cop21/eng/l09r01.pdf>
- Wolf-Gladrow, D. A., Zeebe, R. E., Klaas, C., Körtzinger, A., & Dickson, A. G. (2007). Total alkalinity: The explicit conservative expression and its application to biogeochemical processes. *Marine Chemistry*, 106(1), 287–300. <https://doi.org/10.1016/j.marchem.2007.01.006>

6.25 **hbk00095: Application of ensemble data assimilation for improved prediction of ocean ecosystem indicators**

HLRN Project ID:	hbk00095
Run time:	III/2022 – III/2023
Project Leader:	Dr. Lars Nerger
Project Scientists:	Dr. Yuchen Sun
Affiliation:	Alfred-Wegener-Institut Helmholtz-Zentrum für Polar- und Meeresforschung, Bremerhaven

Overview

This project studies the effect of assimilating observations of ocean physics and biology onto the prediction of ecosystem indicators like particulate organic carbon, trophic efficiency, or dissolved oxygen. The ocean circulation model NEMO will be used in the NEMO-NORDIC configuration for the North- and Baltic Seas. The model is coupled to the ocean-biogeochemical model ERGOM. For the data assimilation, ensemble-based filters will be applied that are provided by the Parallel Data Assimilation Framework PDAF (Nerger and Hiller, 2013, <https://pdaf.awi.de>). The direct combination of NEMO-ERGOM with PDAF provides a highly-scalable data assimilation system that strongly benefits from the computational resources of the HLRN. Next to studying the influence of assimilating different ocean physics and biology observations onto the prediction of the ecological indicators, the effects of combined assimilation of physical and biological observations assimilation and of the application of linear ensemble Kalman filters and nonlinear particle-based filters will be assessed.

The work of this project is part Project SEAMLESS - Services based on Ecosystem data AssiMiLation: Essential Science and Solutions (<https://www.seamlessproject.org>) funded by the EU Horizon-2020 program. The aim of this project is to perform research to improve new and improved indicators of climate-change impacts and food security in marine ecosystems through the application of data assimilation. These developments will later be provided to the EU Copernicus Marine Service CMEMS (<http://marine.copernicus.eu>) which runs different operational marine forecasting centers. These developments will later be provided to the EU Copernicus Marine Service CMEMS (<http://marine.copernicus.eu>) which runs different operational marine forecasting centers.

Model System

In this project we use the ocean circulation model NEMO (Madec et al. 2008). NEMO is a widely used model for research but it is also used operationally at CMEMS. The particular variant of NEMO we use here is NEMO-NORDIC (Hordoir et al. 2019) in an upgraded version, which is based on NEMO 4.0 and uses a resolution of 1 nautical mile and 56 model layers. The Baltic Monitoring and Forecasting Center (BAL-MFC) performs operational services with this model. The configuration covers the full North Sea and Baltic Sea. The high resolution for the large regional domain provides a large potential for scaling by using domain-decomposition. In addition, the model setup uses the IO-Server XIOS to allow for efficient parallel IO. The biogeochemistry model is ERGOM (Neumann 2000, Maar 2011). The model simulates biogeochemical progresses and includes bacteria, two phytoplankton groups as well nutrients, zooplankton and detritus. In addition, a carbonate cycle allows to simulate the partial pressure of CO₂, pH, and particulate carbon.

In preparation of the project, we have already coupled PDAF directly into NEMO using the approach discussed by Nerger and Hiller (2013). By inserting subroutine calls that modify the model to become an ensemble model and by including an assimilation step this approach allows for the best scalability and less disk output. In particular, by keeping the ensemble information in memory the complete ensemble only needs to be written into files for model restarts. The dynamic ensemble integrations will be important for accurate error variance and covariance estimations for the data assimilation. At this stage of the project satellite observations of total surface chlorophyll-a provided by CMEMS are assimilated. The assimilation is performed daily using an ensemble of 30 model state realizations. The system runs fully parallel. Thus, the data assimilative model is configured to run 30 instances of NEMO-ERGOM, each using 2 compute nodes of the HLRN.

Results

The data assimilation is started at March 1, 2015 and run until May 31, 2015. Figure 1 shows the observed and modeled surface chlorophyll (CHL) concentration on March 3, thus at the third day of the data assimilation process. At the beginning of March, the satellite data is still quite limited due to the presence of clouds. As Fig. 1A shows, on March 3, data is nearly only available in the far southern part of the Baltic Sea. Figure 1B shows the concentration without data assimilation (free run) with increased concentrations in the southern Baltic and close to the coast further north. The data assimilation forecast (Fig. 1C), shows the influence of the first two analysis steps of the data assimilation process. Here, the CHL concentration is reduced compared to the free run in the Baltic proper each of 18°E showing that the free run overestimates the concentrations. The analysis update now reduced also the concentrations further west, due to the availability of observations.

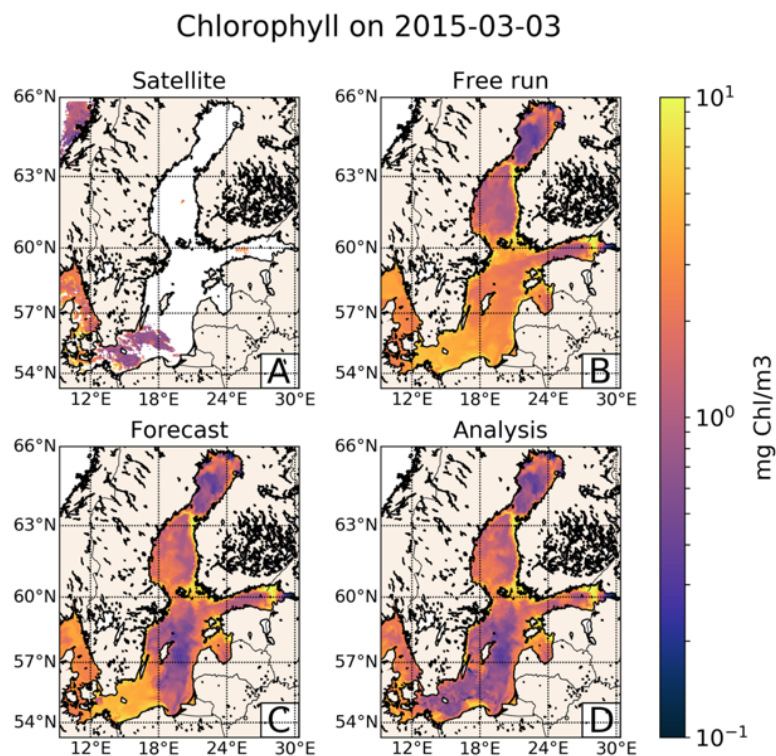


Figure 1: Surface chlorophyll on March 3, 2015 (the third assimilation day). Shown are the (A) satellite data, (B) free ensemble run, (C) 24-h forecast from the assimilation update on March 2, (D) analysis state after incorporating the information from the satellite data.

A particular focus of the project is on the station 'Arkona Basin' which is located at (13.87°E, 54.88°N) in the Southern Baltic just north of the island of Rügen. Figure 2 shows the

development of the surface chlorophyll concentration at this station for the period January to May 2015. Both the concentration resulting from the application of the ensemble Kalman filter (left) and the hybrid nonlinear-Kalman filter (right) are shown. The free run shows an onset of a phytoplankton bloom already at the beginning of February. Apparently, the increasing duration of daylight and a sufficient availability of nutrient and not too cold water, provide good enough growth conditions. Compared to the observations shown from March, the concentrations in the free running model are too high. The data assimilation leads initially to a strong reduction of the concentrations. Overall, both the analysis and the 24-h forecasts are consistent with the available observations.

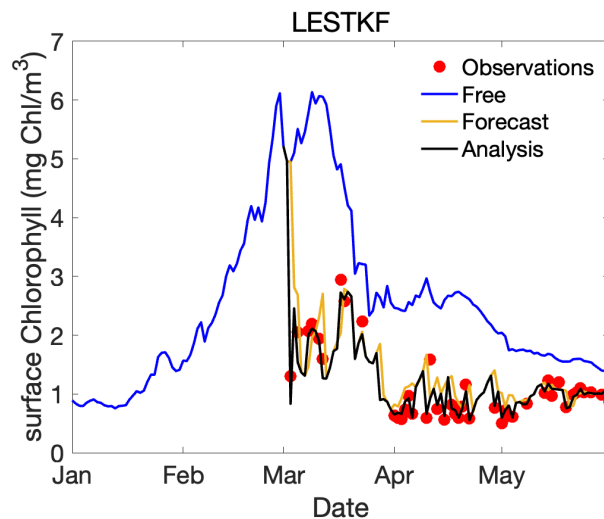


Figure 1: Concentration of surface chlorophyll at the station Arkona over time. The blue line shows the free running ensemble. The observations, when available, are shown as red dots. The assimilation is started on March 1, 2015. Shown are the 24-hour forecasts (orange) and the analysis (black).

References

- Nerger, L., Hiller, W. (2013). Software for Ensemble-based Data Assimilation Systems - Implementation Strategies and Scalability. *Computers and Geosciences*, 55, 110-118. <https://doi.org/10.1016/j.cageo.2012.03.026>
- Madec, G., 2012: NEMO ocean engine, Version 3.3. Note du P^ole de modélisation, Institut Pierre-Simon Laplace (IPSL), 27.
- Hordoir, R., et al., 2019, Nemo-Nordic 1.0: a NEMO-based ocean model for the Baltic and North seas – research and operational applications, *Geoscientific Model Development*, 12, 363-386, <https://doi.org/10.5194/gmd-12-363-2019>
- Neumann T (2000) Towards a 3D-ecosystem model in the Baltic Sea. *J Mar Syst* 25:405–419
- Maar, M., E. F. Moller, J. Larsen, K. S. Madsen, Z. Wan, J. She, L. Jonasson, and T. Neumann, 2011: Ecosystem modelling across a salinity gradient from the North Sea to the Baltic Sea. *Ecological Modelling*, 222, 1696–1711.



The SEAMLESS project has received funding from the European Union's Horizon 2020 research and innovation programme under grant agreement No. 101004032.

6.26 *hbp00041*: Multi-Messenger Signals from Compact Objects

HLRN Project ID:	hbp00041
Run time:	I/2018 – II/2023
Project Leader:	Dr. Claus Lämmerzahl
Project Scientists:	Prof. Stephan Rosswog
Affiliation:	Universität Bremen, Centre for Applied Space Technology and Microgravity, Am Fallturm, 28359 Bremen

Overview

The first detection of a binary black hole merger in 2015 has heralded the long-awaited era of gravitational wave (GW) astronomy. This watershed event confirmed a 100-year-old prediction of Einstein's General Theory of Relativity. Even more importantly, it opened up a completely new channel to observe the Universe. GW astronomy allows to probe how the strongest gravitational fields warp space-time, how ultra-gravity binary stars contribute to the heaviest elements in the cosmos, how such binary systems form and, eventually, how their mergers can be used to probe of the expansion history of the Universe. All these exciting prospects, however, hinge on detecting electromagnetic counterparts of gravitational wave sources. A coincident detection of both gravitational and electromagnetic waves had been a scientific dream for decades.

This dream came true on August 17, 2017: the LIGO/Virgo detectors recorded for the first time the gravitational waves from a binary neutron star merger and subsequently telescopes around the world detected the event all across the electromagnetic spectrum (Abbott et al. 2017). This observation proved that neutron star mergers are indeed strong sources of gravitational waves, that they produce short gamma ray bursts and are a major cosmic factory for the heaviest elements as theoretically predicted (Rosswog et al. 1999, Freiburghaus et al. 1999). Moreover, the subtle tidal imprint on the gravitational wave signal constrained the behaviour of nuclear matter at high densities and the arrival time differences of gravitational waves and photons demonstrated that both propagate at the same speed with a relative precision of 10^{-15} . The combined detection also allowed for an entirely new approach to probe the expansion of the Universe. For all these reasons, this first "multi-messenger" detection of a binary neutron star merger was celebrated by *Science* Magazine as "2017 Breakthrough of the Year"

The main topic of this HLRN project is the theoretical prediction of observable signatures from encounters between compact objects. In the last few years, we have developed a worldwide unique tool, namely a *Lagrangian* hydrodynamics code that solves the equations of relativistic hydrodynamics together with the full set of Einstein's field equations. This code, called SPHINCS_BSSN, is on par with state-of-the-art Eulerian Numerical Relativity codes in terms of the prediction of gravitational waves, but is highly superior when it comes to the long-term evolution of the ejecta and to the prediction of electromagnetic signatures.

Abbott et al., ApJL 848, L12 (2017)

Rosswog et al., A&A 341, 499 (1999)

Freiburghaus, Rosswog, Thielemann, ApJ 525, L121 (1999)

Results

One of our major goals is the physically accurate simulation of neutron star mergers. All of the electromagnetic emission from a neutron star merger is caused by only ~1% of the initial binary

mass that is ejected into space. The properties of this small amount of material are of paramount importance for the modelling and the understanding of observed merger events. All of today's Numerical Relativity codes are Eulerian, i.e. they solve the relativistic hydrodynamic equations on computational meshes. While these codes have delivered many important results, they are very severely challenged in following the small amounts of ejecta.

For this reason, we have developed the worldwide first (and so far only) Lagrangian Numerical Relativity code [Rosswog & Diener 2021]. This code solves the full set of Einstein field equations to evolve the spacetime on a refined mesh, similarly to more conventional Eulerian Numerical Relativity codes. The part that is completely different from existing methods is that we evolve matter by freely moving, Lagrangian particles. This approach is “on par” with established Eulerian Numerical Relativity approaches when it comes to evolving dynamical spacetimes, but has major advantages in evolving the small amounts of matter that are ejected into space during the merger of a neutron star.

Our new code is named SPHINCS_BSSN which stands for *Smoothed Particle Hydrodynamics In Curved Spacetime* and the “BSSN” in the code name stands for the method with which the spacetime is evolved (due to Baumgarte, Shapiro, Shibata, Nakamura). This is the world-wide first and only code that is both Lagrangian and fully general relativistic in its spacetime evolution. SPHINCS_BSSN has passed a large number of test cases with excellent precision [Rosswog & Diener 2021; Diener, Rosswog, Torsello 2022]. In the last year we have also made major progress in simulating merging neutron star binaries. An example of one of our first neutron star merger simulations with SPHINCS_BSSN, performed with the help of HLRN resources, is shown in Figure 1.

Outlook

We have recently developed a unique simulation tool, the only *Lagrangian* Numerical Relativity code that solves the full set of Einstein equations. Our first simulations were dedicated to a large set of benchmarks that demonstrated the excellent accuracy of our new tool. Subsequently, we have performed the first fully relativistic Lagrangian neutron star mergers, see e.g. Fig.1, and in the near future we aim at harvesting the full potential of our new methodology and explore the detailed ejecta evolution and the resulting electromagnetic emission.

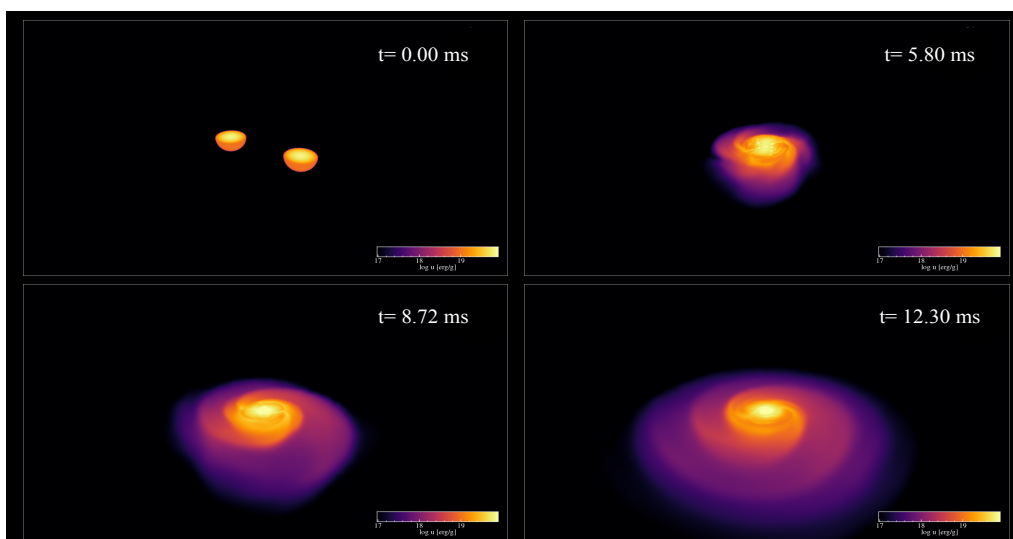


Figure 1: Simulation of two merging neutron stars using the world-wide unique Lagrangian Numerical Relativity code SPHINCS_BSSN. (Simulation from Rosswog, Diener, Torsello, *Thinking outside the box: Numerical Relativity with Particles*; *Symmetry*, 14, 6, 1280 (2022).)

Rosswog & Diener, *SPHINCS_BSSN: a general-relativistic smooth particle hydrodynamics code for dynamical space times*; Classical and Quantum Gravity, 38, 11, 115002 (2021)

Diener, Rosswog, Torsello, *Simulating neutron star mergers with the Lagrangian Numerical Relativity code SPHINCS_BSSN*; European Physical Journal A; 58, 4, 74 (2022)

Rosswog, Diener, Torsello, *Thinking outside the box: Numerical Relativity with particles*; Symmetry, 14, 6, 1280 (2022)

Publications

1. *Correlations of r-Process Elements in Very Metal Poor Stars as Clues to their Nucleosynthesis Sites* Farouqi, K., Thielemann, F.K., Rosswog, S., Kratz, K.L., Astronomy & Astrophysics, Volume 663, id. A70, 43 pp (2022)
2. *Fundamental Physics in the Gravitational-Wave Era* Bernitt, S. et al.; Nuclear Physics News, vol. 32, issue 1, pp. 16-19 (2022)
3. *Are interactions with neutron star merger winds shaping the jets?* Nativi, L. Lamb, G. P., Rosswog, S., Lundman, C., Kowal, G., MNRAS 509, 903 (2022)
4. *Long-Term Simulations of Dynamical Ejecta: Homologous Expansion and Kilonova Properties* Neuweiler, A., Dietrich, T., Bulla, M., Chaurasia, V., Rosswog, S. Ujevic, M., Phys. Rev. D., Vol. 107, issue 2, articleid 023016 (2022)
5. *Modelling Populations of Kilonovae* Setzer, C. N.; Peiris, H. V.; Korobkin, O.; Rosswog, S.; MNRAS 520, 2829 (2023)
6. *Inhomogeneous Jets from Neutron Star Mergers: One Jet to Rule them all* Lamb, G., Nativi, L., Rosswog, S., Kann, A., Levan, A., Lundman, C., Tanvir, N; Universe, vol. 8, issue 12, p. 612 (2022)
7. *Spitzer mid-infrared detections of neutron star merger GW170817 suggests synthesis of the heaviest elements* Kasliwal, M., Kasen, D., Lau, R., Perley, D., Rosswog, S., Ofek, E., Hotokezaka, K., Chary, R., Sollerman, J.; Goobar, A.; Kaplan, D. MNRAS 510, L7 (2022)
8. *Simulating neutron star mergers with the Lagrangian Numerical Relativity code SPHINCS_BSSN* Diener, P., Rosswog, S., Torsello, F.; 25 pages, The European Physical Journal A, Volume 58, Issue 4, article id.74 (2022)
9. *Thinking Outside the Box: Numerical Relativity with Particles* Rosswog, S., Diener, P., Torsello, F., Symmetry, vol. 14, issue 6, p. 1280 (2022)
10. *Heavy Elements and Electromagnetic Transients from Neutron Star Mergers* S. Rosswog & O. Korobkin, Annalen der Physik, Nov. 2022, <https://doi.org/10.1002/andp.202200306>
11. *Astrophysics with the Laser Interferometer Space Antenna* Amaro-Seoane, P. et al., submitted to Living Reviews in Relativity, eprint arXiv:2203.06016 (2022)
12. *Modelling astrophysical fluids with particles* Rosswog, S.; The Predictive Power of Computational Astrophysics as a Discovery Tool Proceedings IAU Symposium No. 362, 2023 D. Bisikalo, D. Wiebe & C. Boily, eds.; doi:10.1017/S1743921322001600 (2023)
13. *Hierarchical triples as Early Sources of r-process Enrichments* Bartos, Rosswog, Gayathri, Miller, Veske, Marka; submitted (2023)

Presentations (based on HLRN results)

1. *Modelling the multi-messenger signals of gravitational wave sources* Invited keynote talk at the Spring Meeting of the German Physical Society (“Fachverbands Gravitation und Relativitätstheorie”), Dresden, March 2023
2. *Neutron star merger simulations with the Lagrangian numerical relativity code SPHINCS BSSN* Invited talk at the Heraeus Seminar 774, “Kilonova: Multimessenger and Multiphysics”, Bad Honef, Nov 28 - Dec 01, 2022

3. *Multi-messenger astrophysics with neutron star mergers*
Colloquium of the Excellence Cluster “Quantum Universe”, DESY Campus Hamburg, Nov 22, 2022
4. *The ejecta of neutron star mergers*
Invited review Weizmann Institute, Rehovot, Israel, June 20, 2022
5. *Thinking outside the box: neutron star mergers with the Lagrangian Numerical Relativity code SPHINCS BSSN*
Talk at Institute for Nuclear Theory Seattle, USA, May 23, 2022
6. *Thinking outside the box: Numerical Relativity with particles as a new tool for multi-messenger astrophysics*
Conference of the COST Action PHAROS in Rome, Italy, May 19, 2022
7. *Simulating neutron star mergers as sources of gravitational waves and heavy elements*
Lecture at winterschool “Waves in Astrophysics” at the Nordic Institute of Theoretical Physics (NORDITA), January 13, 2022

6.27 *hbp00058*: Exploring the mechanistic process of vitamin B₁₂ acquisition by human gut bacteria

HLRN Project ID:	hbp00058
Run time:	III/2022 – II/2023
Project Leader:	Professor Dr. Ulrich Kleinekathöfer
Project Scientists:	Kalyanashis Jana, PhD
Affiliation:	School of Science, Constructor University

Overview

Vitamin B₁₂ (cobalamin) is one of the most complex organometallic cofactors and vitamins as well as one of the most essential nutrients for many Gram-negative bacteria, such as *E. coli*, *B. thetaiotaomicron*, etc. *E. coli* uptakes vitamin B₁₂ by outer membrane (OM) protein BtuB, whereas the B₁₂ procurement process of the Gram-negative bacterium *B. thetaiotaomicron* is quite complicated and depends upon several vitamin B₁₂ binding proteins, e.g., BtuB, BtuG, BtuH. The OM protein BtuB transports the vitamin B₁₂ in association with surface-exposed lipoprotein BtuG in a competing manner with intrinsic factor (IF), which transports B₁₂ to the cell in the human body.^{1,2} It has recently been reported the lipoprotein BtuG directly binds vitamin B₁₂ with femtomolar affinity, thereby facilitating vitamin B₁₂ intake and competing with IF in association with OM protein BtuB. Newly crystalized BtuBG crystal structure and cyanocobalamin bound BtuG protein of *B. thetaiotaomicron* were considered for the computational study to explore the CNCbl acquisition by BtuG in BtuBG protein, and transport of the CNCbl across from BtuG active site to BtuB active site.³

Cyanocobalamin (CNCbl) and Hydroxocobalamin (HOCbl) are commonly used for supplementation along with the methylcobalamin (MeCbl) and adenosylcobalamin (AdoCbl) in case of a vitamin B₁₂ deficiency in the human body.⁴ The experimental binding constants of CNCbl or HOCbl (both containing small axial ligands CN or OH) with the transporters are comparable to that of AdoCbl (containing a relatively large axial group of adenosyl). Most of the reports available in the literature show a CNCbl binding and translocation through a protein of the Gram-negative bacteria outer membrane. In this context, the binding affinity of all the cyanocobalamin (Me, Ado, HO, or CN) toward the surface-exposed BtuG protein as well as the BtuG lid closing and translocation of the cyanocobalamin through the BtuBG molecule was explored extensively for the first time.

Furthermore, the human gut *Bacteroidetes* depend upon several proteins to acquire vitamin B₁₂ and BtuH is one of them, which helps to obtain vitamin B₁₂ in gut *Bacteroidetes*.⁵ This opens the exciting option to explore the structural dynamics of the newly resolved CNCbl bound-BtuH protein using unbiased MD simulations as well as to determine the binding free energy of CNCbl towards BtuH using well-tempered metadynamics (WTMtD) simulations. Furthermore, we plan to explore how the BtuH protein captures CNCbl from an arbitrary position by placing the CNCbl 10-15 Å away from the binding site. To this end, the BtuBGH cryo-EM structure will be considered for unbiased MD simulation to examine the structural dynamics of the BtuBGH complex. The total system is made of the outer-membrane protein BtuB and the surface-exposed lipoproteins BtuG and BtuH. Herein, we have employed unbiased molecular dynamics (MD) simulation, enhanced sampling techniques, applied field simulations and umbrella sampling to demonstrate the above-mentioned objectives.⁶

We would like to mention that a small portion of the assigned compute time was used for a study concerning the assembly of transmembrane pores from mirror-image peptides which was published recently.⁷

Results

The MD simulation studies revealed that the BtuG molecule could pull vitamin CNCbl from rather arbitrary close by positions to its active site by strong electrostatic and noncovalent interactions (Figure 1). An electrostatic potential map analysis revealed that the negatively charged binding pocket of the BtuG can clearly attract the highly dipolar CNCbl molecule. Using multiple-walker WTMD binding free energies were calculated and corroborated the experimental dissociation constant of about 10^{-14} M. Furthermore, the BtuG lid opening process using biased and unbiased MD simulations revealed that the BtuG moves away from BtuB via a hinge loop and could open up to 40° to facilitate the acquisition of CNCbl from the bulk. In the next step, unbiased simulations were performed with a starting structure of 40° open structure with CNCbl being outside of the BtuG protein. The BtuG lid started closing very quickly, where the BtuG lid angle was around 20° , and the CNCbl molecule reached the BtuG active site cavity after $1\mu\text{s}$. Finally, the CNCbl bound BtuBG was considered to reveal the conformational dynamics of BtuBG protein and the translocation process of the CNCbl from the active site cavity of BtuG to BtuB. In the close state of CNCbl bound-BtuBG, BtuG binds CNCbl weakly compared to that of the CNCbl-BtuG due to several loop rearrangements, which further enables CNCbl molecules to move toward BtuG cavity.

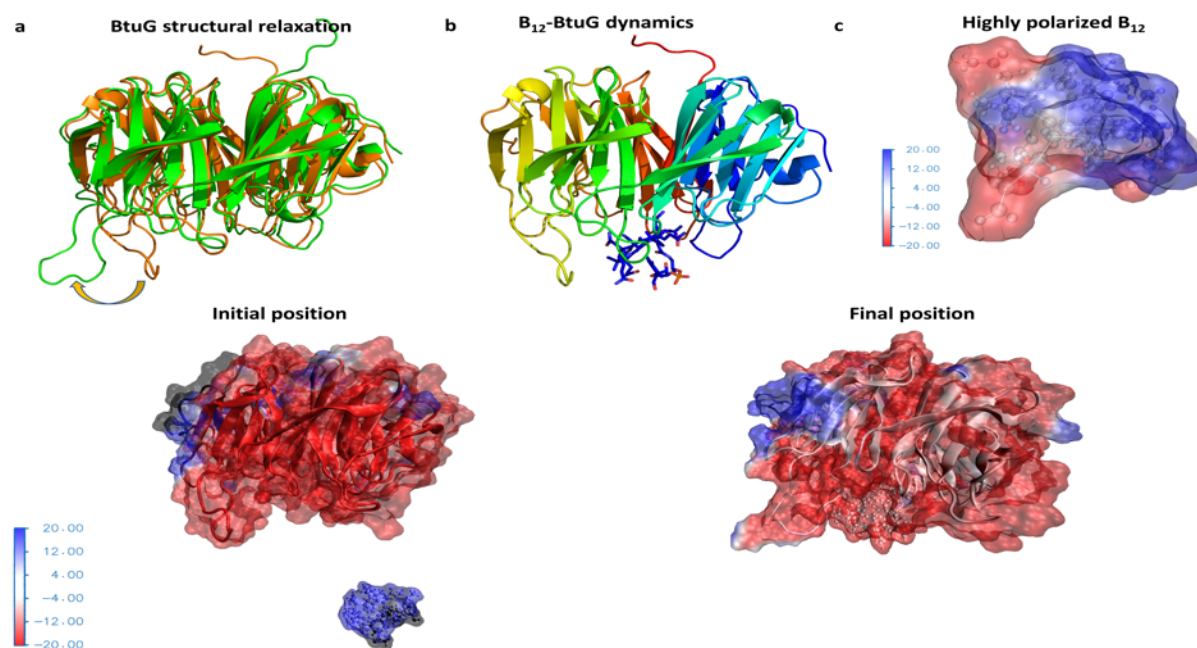


Figure 1: **a.** Crystal (brown) and representative MD structure (green) of the BtuG protein extracted from the $1\mu\text{s}$ run (starting structure from the CNCbl-BtuG2 crystal structure but without the CNCbl molecule). **b.** CNCbl-BtuG2 crystal structure after the end of $1\mu\text{s}$ run demonstrated remarkable stability of the CNCbl-BtuG2 complex. **c.** Electrostatic potential map of the CNCbl molecule with a large dipole moment. The “upper part” of CNCbl, i.e., the cobalt (III) is partially positive, whereas the phosphate part of the molecule is negatively charged. **d-e.** In the protein-ligand system, CNCbl is positively charged, whereas the protein system has a negative charge. Therefore, BtuG can easily attract CNCbl via electrostatic interactions.

MeCbl and AdoCbl bound BtuBG simulations:

Initially, MeCbl and AdoCbl affinity toward BtuG was explored using multiple walker WTMtD simulations. The ligands unbinding from the BtuG active site using WTMtD simulations revealed that the binding affinity of the Me-Cbl and AdoCbl are very similar to that of the binding affinity of CN-Cbl. The MeCbl bound BtuBG protein simulation in POPE bilayer membrane was carried out to explore the translocation of Me-Cbl through the BtuBG protein. The free energy associated with the translocation process is very similar to that of the translocation process of CNCbl through the BtuBG channel. The WTMtD simulations showed that MeCbl moves toward the BtuB cavity in a tilted manner and reorients itself in the BtuBG channel during this low-energy translocation process.

The translocation process of the AdoCbl was carried out extensively using multiple walker WTMtD simulations. The unbiased and WTMtD simulation of AdoCbl bound BtuBG simulations suggests that the translocation process was pretty difficult because of the large size having a similar binding affinity toward the BtuG protein. A mutation study revealed the importance of the acidic amino acid residues in the binding of CNCbl. Therefore, further exploration of the binding affinity of AdoCbl, and MeCbl with the E55A and Q336A mutated-BtuG were performed for a detailed molecular-level understanding.

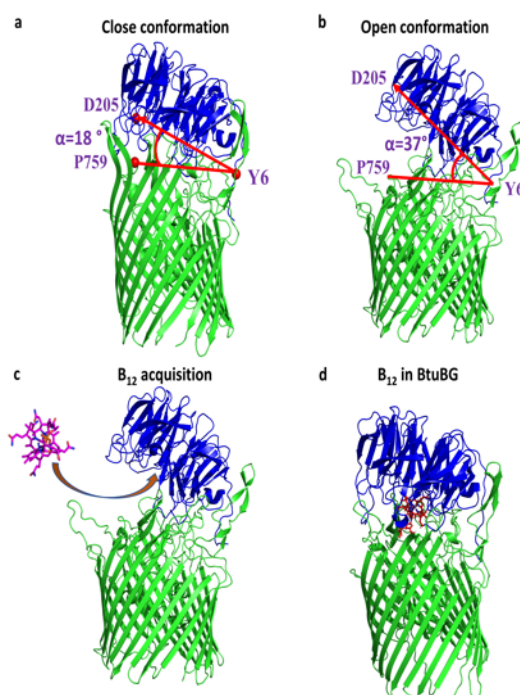


Figure 2: **a.** Cartoon structure of the BtuBG protein: green cartoon structure represents BtuB OM protein, where the blue cartoon structure corresponds to the lipoprotein BtuG. The initial angle between the BtuB and BtuG was 18° in the crystal structure. **b.** An open-state conformation obtained from the high temperature simulation at 400 K. **c.** A schematic representation of the vitamin B₁₂ acquisition process. **d.** Vitamin B₁₂ in the binding cavity of the BtuBG.

Outlook

A new CNCbl binding protein, BtuH, crystal structure has been structurally resolved and provides us with an opportunity to explore the binding affinity to CNCbl, the stability and the role of the BtuGH and the BtuBGH complexes in the CNCbl transport process. A previous report revealed that Ca^{2+} and Na^+ ions play a significant role in the binding of the CNCbl in the binding cavity of BtuH and the orientation of the CNCbl at the binding site cavity of BtuH is opposite to that of the orientation in the BtuG protein.⁵ In this context, we would like to explore

the stability of the CNCbl-bound BtuH in the presence of Ca^{2+} and Na^+ ions, and subsequently, with two Ca^{2+} , two Na^+ , only one Ca^{2+} , only one Na^+ , and without any ion using unbiased MD simulations. The binding affinity of CNCbl with BtuH will be calculated and compared with the binding affinity of CNCbl-BtuG as well as the experimentally determined dissociation constant. The experimental study suggests that the binding affinity with BtuH is lower than that to BtuG. Since the binding affinity with BtuH is lower than that of BtuG, it is expected that CNCbl can be transported from BtuH binding site to the BtuG binding site. Calculating the free energy required for the CNCbl transport process would also be noteworthy.

References

- 1 S. J. Hickman, R. E. M. Cooper, L. Bellucci, E. Paci and D. J. Brockwell, Gating of TonB-dependent transporters by substrate-specific forced remodelling, *Nat. Commun.*, 2017, **8**, 14804.
- 2 A. G. Wexler, W. B. Schofield, P. H. Degnan, E. Folta-Stogniew, N. A. Barry and A. L. Goodman, Human gut *Bacteroides* capture vitamin B_{12} via cell surface-exposed lipoproteins, *Elife*, 2018, **18**, 7.
- 3 J. Abellón-Ruiz, K. Jana, A. Silale, A. M. Frey, A. Baslé, M. Trost, B. van den Berg and U. Kleinekathöfer, BtuB TonB-dependent transporters and BtuG surface lipoproteins form stable complexes for vitamin B_{12} uptake in gut *Bacteroides*, *bioRxiv*, DOI: 10.1101/2022.11.17.516869.
- 4 R. Obeid, S. N. Fedosov and E. Nexø, Cobalamin coenzyme forms are not likely to be superior to cyano- and hydroxyl-cobalamin in prevention or treatment of cobalamin deficiency, *Mol. Nutr. Food Res.*, 2015, **59**, 1364–1372.
- 5 E. E. Putnam, J. Abellon-Ruiz, B. J. Killinger, J. J. Rosnow, A. G. Wexler, E. Folta-Stogniew, A. T. Wright, B. van den Berg and A. L. Goodman, Gut Commensal *Bacteroidetes* Encode a Novel Class of Vitamin B_{12} -Binding Proteins, *MBio*, 2022, **13**, e02845-21.
- 6 J. D. Prajapati, U. Kleinekathöfer and M. Winterhalter, How to Enter a Bacterium: Bacterial Porins and the Permeation of Antibiotics, *Chem. Rev.*, 2021, **121**, 5158–5192.
- 7 S. Krishnan R, K. Jana, A. H. Shaji, K. S. Nair, A. D. Das, D. Vikraman, H. Bajaj, U. Kleinekathöfer and K. R. Mahendran, Assembly of transmembrane pores from mirror-image peptides, *Nat. Commun.*, 2022, **13**, 5377.

6.28 *hbp00067*: Carrier Multiplication in Monolayer Transition Metal Dichalcogenides

HLRN Project ID:	hbp00067
Run time:	III/2020 – III/2023
Project Leader:	Prof. Thomas Frauenheim
Project Scientists:	Yuxiang Liu
Affiliation:	BCCMS University of Bremen

Overview

Photo-excitation of semiconductors with photon energies exceeding their bandgap E_g creates electron-hole pairs that can be collected to produce an electric current. When the excess energy of photoexcited carriers is higher than E_g , carriers obtain sufficient energy to excite another electron-hole pair, a process which is known as carrier multiplication (CM). Beard et al. predicted that CM could overcome the Schokley-Queisser limit and raise solar cell efficiency to ~46% [1]. For maximal use of energy, with energy conservation limit and competition from phonon-assisted relaxations, the threshold energy of CM should be closed to around $2E_g \sim 2.5E_g$ [2]. However, in bulk semiconductors, the threshold energy can reach as high as $\sim 6E_g$ [3], and renders its application impractical. In contrast, CM performance can be enhanced in nanostructures, where quantum confinement relaxes the strict momentum conservation requirement and phonon bottleneck inhibits phonon emission [4].

Recently, CM phenomenon is observed in two-dimensional transition metal dichalcogenides (TMDCs) films of 2H-MoTe₂ and 2H-WSe₂ with threshold energy as low as $2E_g$, and conversion efficiency can reach nearly 99% [5-6]

Results

Real-time time-dependent density functional theory (rt-TDDFT) method, we investigate CM phenomenon in six monolayer TMDCs MX₂ (M = Mo, W; X = S, Se, Te). For the case of monolayer MoTe₂, electron-hole pairs are created with energy of $\sim 2E_g$, where the hole and electron excess energy ΔE_h and ΔE_e equal to $0.86E_g$ and $0.14E_g$, respectively. In principle, ΔE_h ($0.86E_g$) and ΔE_e ($0.14E_g$) are insufficient to excite another electron from valence bands across the bandgap. Surprisingly, Figure1 (a) shows that the amount of carriers keeps increasing upon photo excitation and carrier generation quantum yield reaches ~ 1.07 at 500fs. To reveal the mechanism of CM in monolayer MoTe₂, time-evolution of bandgap is plotted in Figure1(c). Upon excitation, the bandgap of MoTe₂ oscillate periodically owing to the nuclear vibrations. Overall, the bandgap becomes narrower along the whole trajectory and even drops to 60% of its initial value, which enables excited holes have sufficient energy to excite additional electron-hole pair across the bandgap. Obviously, the inset of Figure1(c) shows that ΔE_e surpasses the bandgap at ~ 50 fs, triggering CM. In other words, besides energy dissipation, nuclear vibrations can also cause significant changes in electronic structures and carrier relaxation dynamics. To further investigate the influence of phonons on the bandgap, FTs of $E_g(t)$ is plotted in the inset of Figure1(c). FTs displays a characteristic frequency at ~ 163.7 cm⁻¹ which is associated to the out-of-plane vibrational mode of tellurium atoms (A'). Therefore, it is expected that A'-mode of MoTe₂ has impressive effect on the bandgap. Thus, the resulting bandgap reduction favors CM process, especially when the excess energy of carriers $\Delta E_{e/h}$ is below the threshold limit.

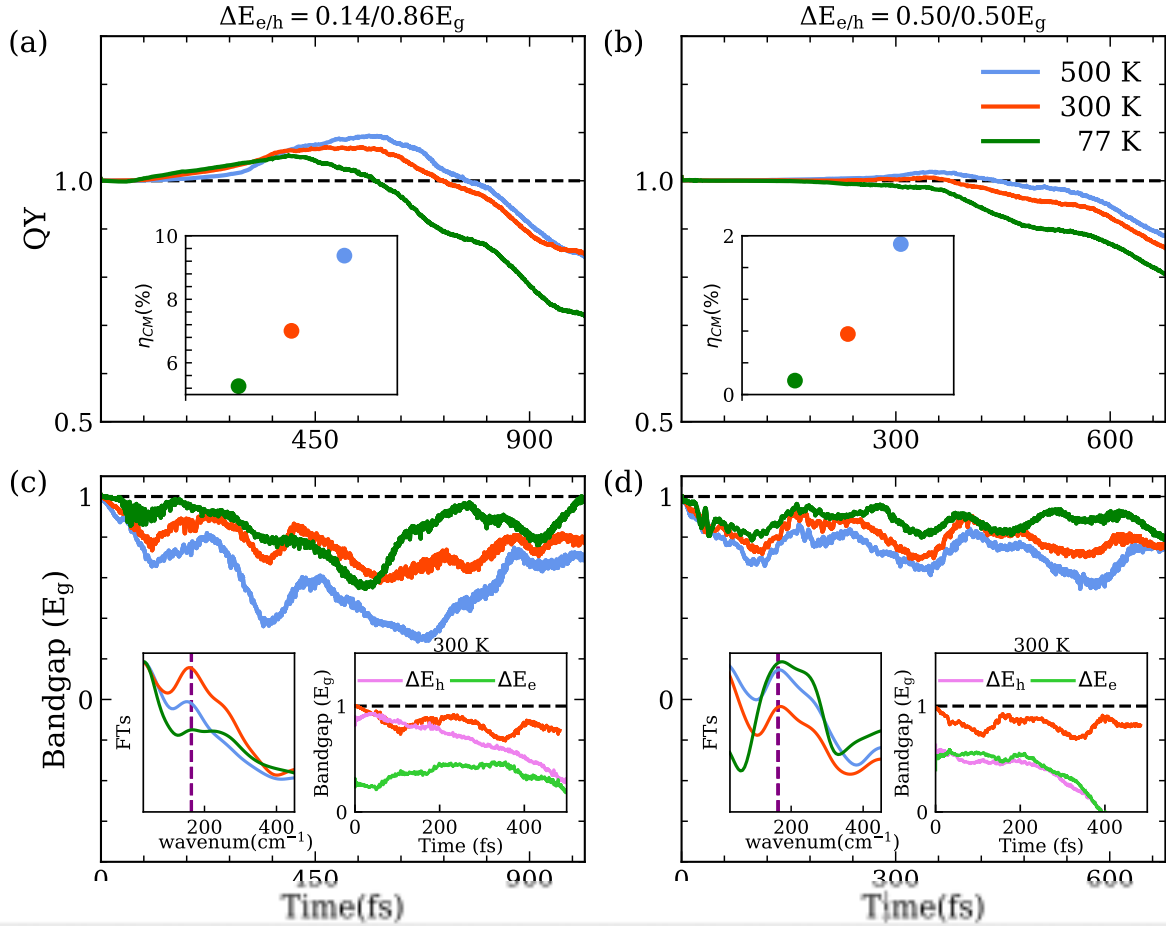


Figure 1: Excitation dynamics of monolayer MoTe₂ with different carrier excess energies at different temperatures. Electron-hole pairs are generated by photon with energy of $2E_g$ at temperature 77 K, 300 K and 500 K. The excess energies of carrier are $\Delta E_{e/h}=0.14/0.86E_g$ (left panel) and $\Delta E_{e/h}=0.5E_g/0.5E_g$ (right panel). (A)-(B) Carrier generation QY of CM in MoTe₂ as a function of time upon excitation. Inset: CM conversion efficiency at the three temperatures. (C)-(D) $E_g(t)$ 77 K, 300 K and 500 K. Inset: $E_g(t)$ at 300 K is compared with the excess energy of hole ΔE_h and electron ΔE_e , and the dashed line represents the bandgap at $t=0$ fs. Inset: FTs of time-dependent bandgap $E_g(t)$. Vertical dashed line represents phonon mode A' with vibrational frequency of 163.7 cm^{-1} .

We further study the scenario where MoTe₂ is excited at different temperatures to identify the positive effect of EPC on CM process (Figure1). Electron-hole pairs with energy of $2E_g$ are created at 77 K, 300 K and 500 K, respectively. Here, we take account for two type of excitation: (1) asymmetric electron-hole pairs with $\Delta E_e=0.14E_g/\Delta E_h=0.86E_g$ and (2) symmetric electron-hole pairs with $\Delta E_e=\Delta E_h=0.50E_g$. To facilitate our analysis, we quantify the CM conversion efficiency as follows

$$\eta_{CM} = \frac{\phi_{max} - 1}{\frac{h\nu}{E_g} - 1} \times 100\%$$

where ϕ_{max} is the maximum QY in the time evolution process, and $h\nu$ is the energy of phonons. Generally, it is anticipated that weakening EPC is a straightforward method to enhance η_{CM} . However, this viewpoint ignores the influence of nuclear motions. As shown in Figure1(A), with phonon-induced narrow bandgap, CM phenomenon is observed even when the excess energy ΔE_h is only $0.86E_g$. With a higher temperature, the vibration excursions of atoms are larger. Consequently, a higher carrier generation QY in MoTe₂ is achieved via a narrower bandgap. The CM conversion efficiency η_{CM} is promoted from 5.26% to 9.37% when then temperature

rising from 77 K to 500 K. Similarly, increasing temperature has the same effect on improving η_{CM} for the symmetric electron-hole pair excitation, as shown in Figure1(B). Especially, at 77 K and 300 K, CM is not observed, and nonradiative recombination and Auger recombination dominate the carrier relaxation process. This can be explained by the fact that $\Delta E_h(t)$ and $\Delta E_e(t)$ are both below $E_g(t)$ along the whole trajectory (Figure1(D)). As discussed above, the oscillation of $E_g(t)$ is caused by A'-mode. However, at 77 K, only a few phonons are excited and $E_g(t)$ keeps much larger than the excess energy of carriers. In contrast, at 500 K, intensive vibrations shrink the bandgap by $\sim 50\%$ and trigger the onset of CM. In this way, we present the possibility to reduce the threshold energy for CM in monolayer TMDCs.

To examine the above mechanism, we excite MoTe₂ with energy of $1.75E_g$ at 300K. Precisely, ΔE_e and ΔE_h are $0.58E_g$ and $0.17E_g$, respectively. As shown in Figure2, CM is indeed observed after excitation, and CM conversion efficiency η_{CM} is $\sim 4\%$ at 500 fs. Figure2(B) shows that phonon-induced reduction of bandgap is about $0.45E_g$, thus excited electrons have sufficient energy to scatter extra electrons across bandgap at ~ 150 fs, resulting in CM. It is the first time that CM process occurs with excitation energy lower than $2E_g$, which implies that phonons have positive effect on CM process in monolayer TMDCs.

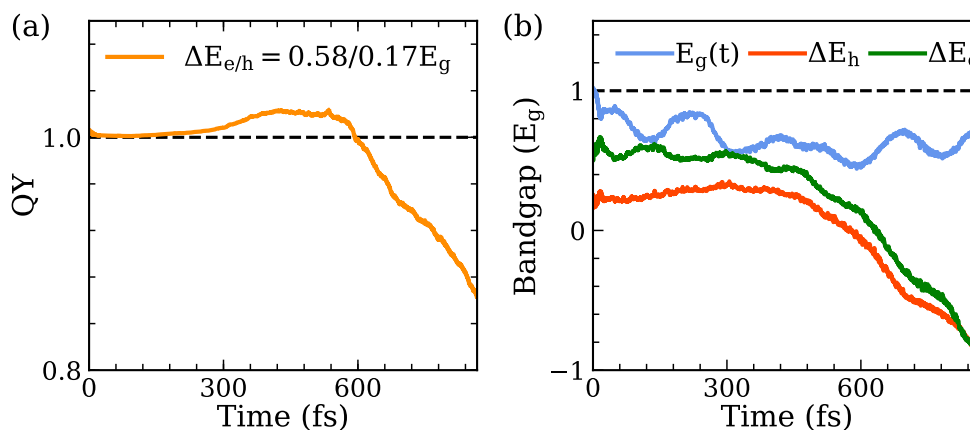


Figure 2: Excitation dynamics of monolayer MoTe₂ with excitation energy of $1.75E_g$. The hole and electron excess energies are $\Delta E_{e/h} = 0.58/0.17E_g$. (A) Carrier generation QY as a function of time. (B) Time-evolution of bandgap $E_g(t)$, hole excess energy $\Delta E_h(t)$ and electron excess energy $\Delta E_e(t)$.

In summary, CM phenomenon can be observed in monolayer TMDCs. Specially, phonon-induced narrower bandgap lower the CM threshold beyond limit.

Outlook

In following project phase, we plan to investigate the Bi-doping effect on the carrier multiplication in graphene.

Publications

1. Y. Liu, T. Frauenheim, C.Y. Yam. Carrier Multiplication in Transition Metal Dichalcogenides Beyond Threshold Limit[J]. Advanced Science, 2022, 9(31): 2203400.
2. Q. Liu, X. Lu, Y. Liu, et al. Carrier Relaxation and Multiplication in Bi Doped Graphene[J]. Small, 2023: 2206218.

References

1. E. A Beard., C. Matthew, Accounts of Chemical Research 2013, 46, 6 1252.

2. M. C. Beard, A. G. Midgett, M. C. Hanna, J. M. Luther, B. K. Hughes, A. J. Nozik, Nano Letters 2010, 10, 8 3019.
3. J. A. McGuire, J. Joo, J. M. Pietryga, R. D. Schaller, V. I. Klimov, Accounts of Chemical Research 2008, 41, 12 1810.
4. L.-W. Wang, M. Califano, A. Zunger, A. Franceschetti, Physical Review Letters 2003, 91, 5 056404.
5. J.-H. Kim, M. R. Bergren, J. C. Park, S. Adhikari, M. Lorke, T. Frauenheim, D.-H. Choe, B. Kim, H. Choi, T. Gregorkiewicz, et al., Nature Communications 2019, 10, 1 1.
6. W. Zheng, M. Bonn, H. I. Wang, Nano Letters 2020, 20, 8 5807.

6.29 *hbp00068*: Enhanced sampling methods for constructing free energy surfaces of antibiotic permeation through porins

HLRN Project ID: hbp00068
 Run time: IV/2020 – IV/2023
 Project Leader: Professor Dr. Ulrich Kleinekathöfer
 Project Scientists: Abhishek Acharya
 Affiliation: School of Science, Constructor University

Overview

Antibiotic resistance in bacteria is a growing threat expected to reach pandemic proportions in the coming decades. The development of novel and effective antibacterials are critical to ensuring the general health and well-being, and safety in hospital setting. General diffusion channels called porins have been implicated in the influx of several antibiotics such as chloramphenicol, fluoroquinones, and the β -lactam class of antibiotics into Gram-negative

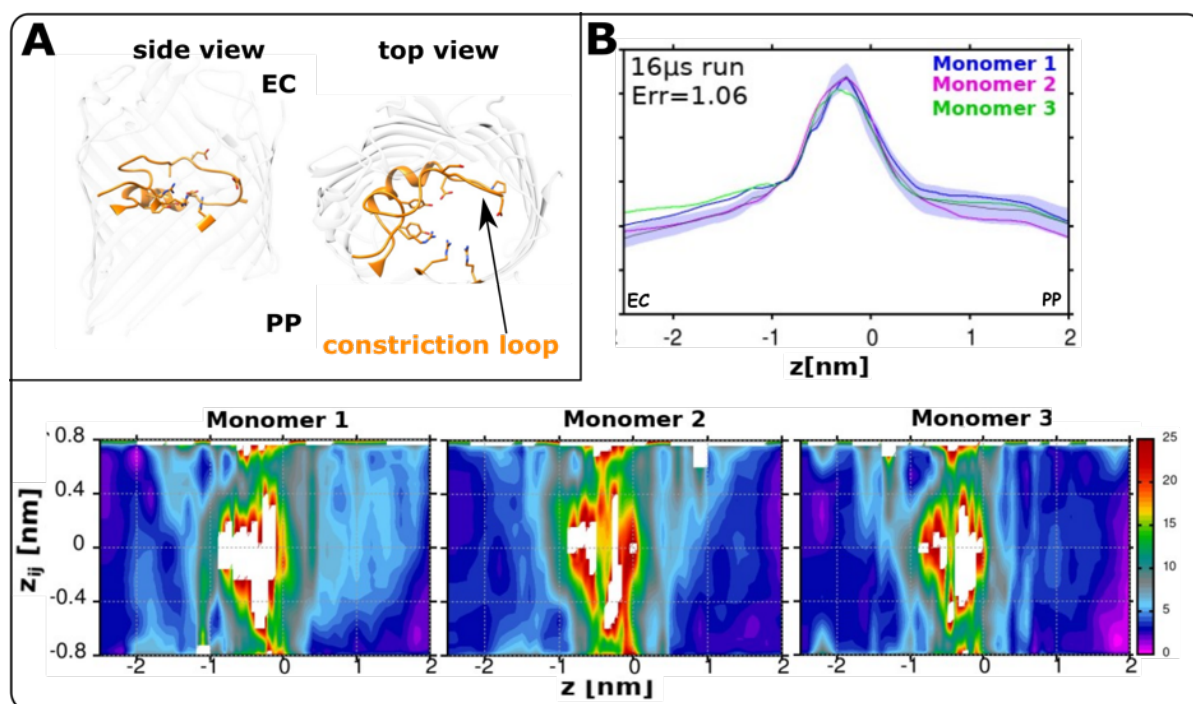


Figure 1: **A.** A cartoon representation of the OmpF channel with the constriction loop at the center of the channel (in orange). This loop forms a narrow constriction region at the center that poses a large entropic barrier. **B.** Results obtained with the initial temperature accelerated sliced sampling (TASS) simulations of ciprofloxacin permeation through OmpF. The upper panel shows the one-dimensional free energy estimates obtained from three independent TASS runs in the three OmpF monomers. The error is shaded in light blue. The lower panels show for each TASS run the two-dimensional free energy surface along the z -vs- z_{ij} space, where z describes the translation of the antibiotic along the z -axis and z_{ij} the orientation of the antibiotic with respect to the z -axis. The white region in the center denotes the restricted rotation of the antibiotic at the constriction region. Reproduced with permission from Ref. 1 Copyright 2021 American Chemical Society

bacterial cells. In this project, we are interested in studying the process of antibiotic permeation into Gram-negative pathogens, with the aim of understanding the molecular mechanisms and associated factors that influence the permeation process. The key objective is to employ enhanced sampling methods for exhaustive sampling of the antibiotic permeation pathways and the accurate estimation of free energy for the permeation of antibiotics through the OmpF

The TASS simulations enabled the accumulation of a large amount of sampling data that was subsequently analysed to obtain biologically important insights. Briefly, the analysis of the ciprofloxacin permeation pathways through OmpF enabled the uncovering of the possible role of loop conformational dynamics of OmpF in the permeation of antibiotics.

Results

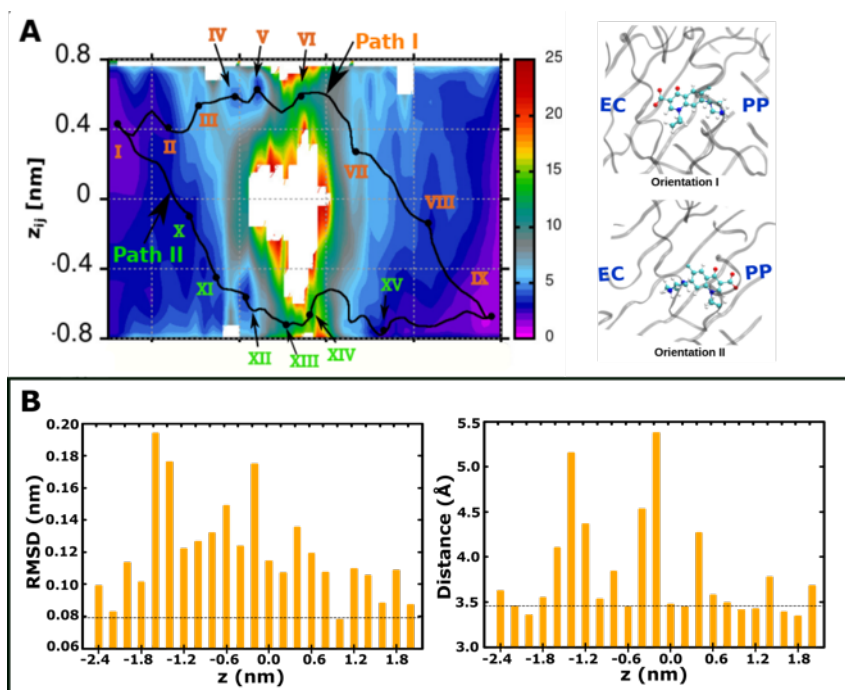


Figure 2: **A.** The two-dimensional average free energy surface obtained from TASS simulations of ciprofloxacin permeation through OmpF depicts two possible permeation pathways, Path I and Path II, with the different metastable states marked in roman numerals. Right panels: Ciprofloxacin assumes two different orientations in the constriction region due to its restricted rotation. **B.** Conformational fluctuation in the L3-FS segment calculated from TASS simulations. Left panel shows the RMSD plot for L3-FS as the antibiotic samples different z -positions along the channel. Larger fluctuations are observed in the central region of the channel. Right panel: The D121-Y32 distance plot as the antibiotic samples different z -positions along the channel. In both plots, the horizontal line marks the baseline values obtained from unbiased MD runs in absence of the antibiotic. Reproduced with permission from Ref. 3 Copyright 2023 American Chemical Society.

The two-dimensional free energy surface for ciprofloxacin permeation suggests two possible pathways for translocation (Fig. 2A). These pathways differ in terms of the orientation of ciprofloxacin as it passes through the narrow constriction region of OmpF (shown on the right, Fig. 2A). Analysis of the pathway configurations suggested that both the antibiotic permeation is associated with conformational fluctuations in the loop L3, specifically the segment F118-S125, noted by the greater average RMSD for the segment (Fig. 2B, left panel). We also noted large fluctuations in the hydrogen bond D121-Y32 (Fig. 2B, right panel). Additional applied field simulations were performed on OmpF mutants with the hydrogen bond interactions abrogated. The simulations suggested that the hydrogen bonds network associated with the L3-FS is critical for the stabilization of the loop conformation (Fig.3). The results of the applied field

simulations were verified with experimental electrophysiology studies that confirmed the destabilization of L3 loop in case of the mutants (data not shown; see Ref. 3). The results of the applied field simulations also enables uncovering the conformational transitions involved in the voltage gating fluctuations that lead to intermittent closure of the OmpF channel. The right panels in Fig. 3 depicts the open-close transition involved in the voltage gating process.

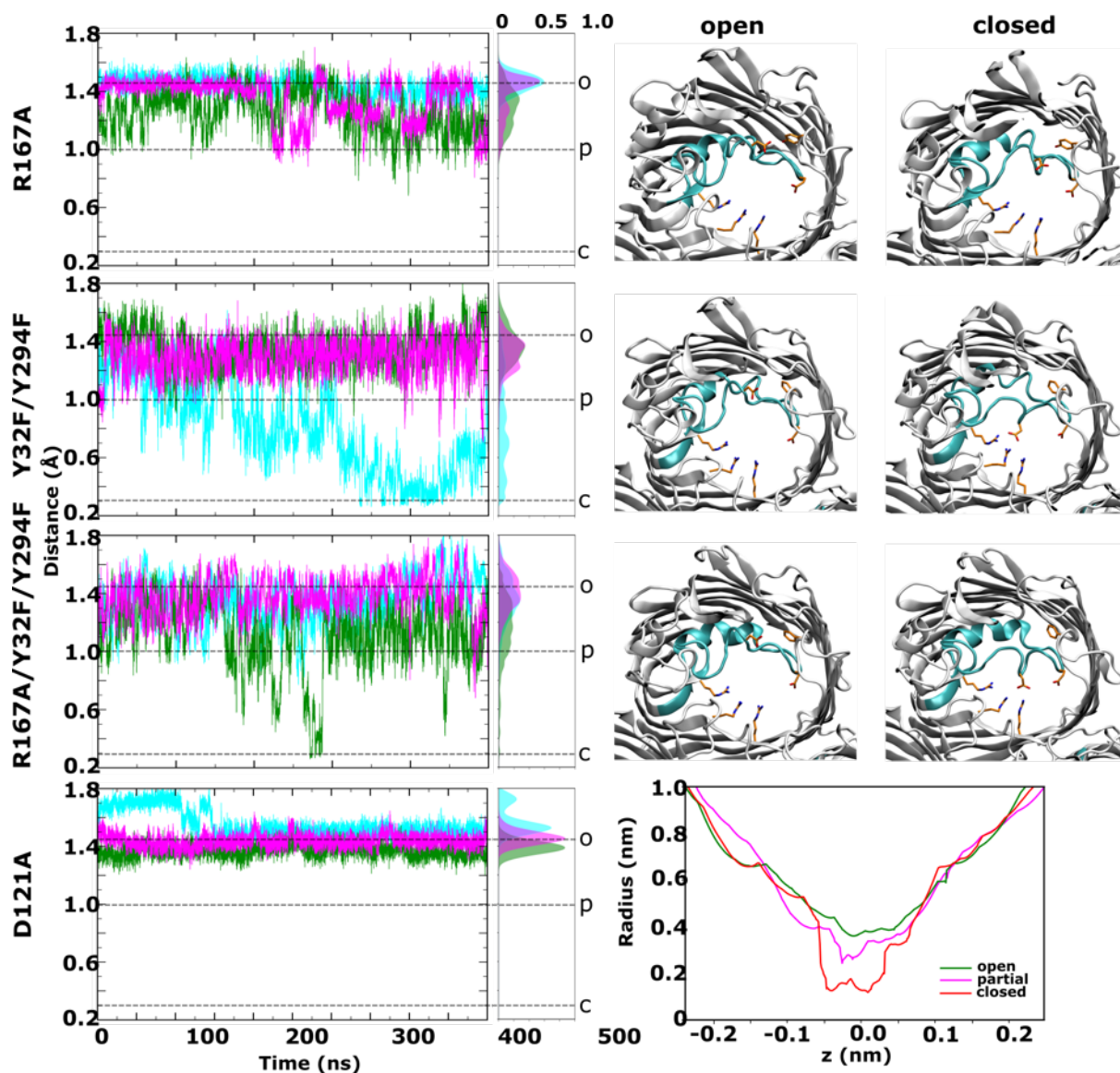


Figure 3: Applied-field simulations performed on the OmpF mutants R167A, Y32F/Y294F, R167A/Y32F/Y294F and D121A at +0.5 V (left panels). For the R167A, Y32F/Y294F and R167A/Y32F/Y294F mutants, open and closed states are also shown on the right. The simulations sampled fully closed (in case of Y32F/Y294F and R167A/Y32F/Y294F) and partially closed states (in case of R167A). Pore radius for representative open, closed and partially closed states observed in applied-field simulations are shown in the bottom right plot. Reproduced with permission from Ref. 3 Copyright 2023 American Chemical Society.

Outlook

The results reported herein suggests that a zwitterionic ciprofloxacin molecule is able to induce conformational fluctuations in the L3-FS and likely aid the permeation process. Since, charges on the antibiotic molecule appear to play a dominant role in the process, it would be interesting

to examine the loop conformational dynamics in case of molecules with different charge distributions. Additional lines of work include examining the permeation pathways for different antibiotics through OmpF orthologs. Preliminary analysis suggests interesting variations in the loop stabilization and structure in the orthologs, that are expected to influence the loop dynamics and antibiotic permeation. Work is underway in this direction.

Publications

1. Acharya, A.; Prajapati, J. D.; Kleinekathöfer, U. Improved Sampling and Free Energy Estimates for Antibiotic Permeation through Bacterial Porins. *J. Chem. Theory Comput.* 2021, 17, 4564–4577.
2. Acharya, A.; Prajapati, J. D.; Kleinekathöfer, U. Atomistic Simulation of Molecules Interacting with Biological Nanopores: From Current Understanding to Future Directions. *J. Phys. Chem. B* 2022, 126, 3995–4008.
3. Acharya, A., I. Ghai, C. Piselli, J. D. Prajapati, R. Benz, M. Winterhalter, and U. Kleinekathöfer, 2023. Conformational Dynamics of Loop L3 in OmpF: Implications toward Antibiotic Translocation and Voltage Gating. *J. Chem. Inf. Model.* 2023, 63, 910–927.

6.30 *hbp00072*: Ozone Profile Retrieval from TROPOMI measurements in the UV spectral range

HLRN Project ID:	hbp00072
Run time:	I/2022 – I/2023
Project Leader:	Dr. Alexei Rozanov
Project Scientists:	Dr. Nora Mettig, Dr. Carlo Arosio
Affiliation:	Institute of Environmental Physics, University of Bremen

Overview

Ozone is one of the most important trace gases in the Earth's atmosphere. The stratospheric ozone layer is crucial for the radiative balance and dynamics of the atmosphere and of particular importance for humans because it protects the biosphere from biologically damaging ultraviolet radiation (UV). On the other hand, ozone near the surface is a biologically harmful gas and a strong oxidant. Consequently, it impacts negatively on human health, ecosystem services and agriculture. Furthermore, tropospheric ozone is a potent greenhouse gas.

Ozone received much public attention after its enormous reduction during Antarctic spring was observed in the 1980s. This so-called ozone hole is the result of human-made chlorofluorocarbon compounds and is still a topic of scientific research today. The recovery of the stratospheric ozone expected after implementation of the Montreal Protocol and its Amendments is monitored continuously.

In order to separate dynamical and chemical effects on ozone that are varying with altitude, it is not sufficient to measure total ozone column amounts only. The key for ozone monitoring is precise measurements of its vertical distribution at high spatial and temporal resolution. Two common and accurate methods to measure ozone profiles are ozonesondes and lidars. However, neither technique can provide sufficient spatial and temporal coverage. For this reason, global ozone monitoring is only possible by using satellite observations. With the launch of Sentinel 5 Precursor (S5P) in October 2017, the TROPOMI nadir-viewing spectrometer measuring the back-scattered solar radiance in the UV/VIS and SWIR spectral range was put in operation. It is a follow-up of OMI and SCIAMACHY instruments. Using TROPOMI data, it is possible to continue time series of past instruments into the future. The particular advantage of TROPOMI is its unprecedented spatial resolution of $28.8 \times 5.6 \text{ km}^2$.

The main objective of this study is to produce and evaluate the first continuous data set of ozone vertical profiles retrieved from TROPOMI measurements with the TOPAS (Tikhonov regularized Ozone Profile retrieval with SCIATRAN) approach. A generation of a dataset covering a period of about 1.5 years enables us to verify the stability of the retrieval and suitability of the static vicarious radiometric calibration used within the algorithm. Furthermore, an extensive validation using measurements from ozonesondes, lidars and other satellite instruments is to be performed before the dataset can be provided to the scientific community to be used for an analysis of the stratospheric ozone evolution.

Results

Major efforts in the project were put to setting up the processing chain, optimization of the retrieval parameters and finally generation of the dataset. Due to several reasons such as multiple repeating of several runs to eliminate bugs in the controlling scripts and to further optimize the retrieval parameters, increasing the accuracy of the radiative transfer as well as higher density of the valid data in the operational level 1 product in comparison with the test

data used in the project preparation stage, only a subset of the envisaged data could be processed. To cover the maximum possible period within the available computing time it was decided to process one day per month between July 2021 and December 2022. It should be noted that no level 1 data in the version ≥ 2.0 , which are needed for the ozone profile retrieval from TROPOMI, are available before July 2021 so far. Thus, the maximum possible period was covered by the retrievals.

The obtained data were compared to measurements from the limb-viewing microwave instrument MLS to assess the overall quality of the data and temporal stability of the retrievals.

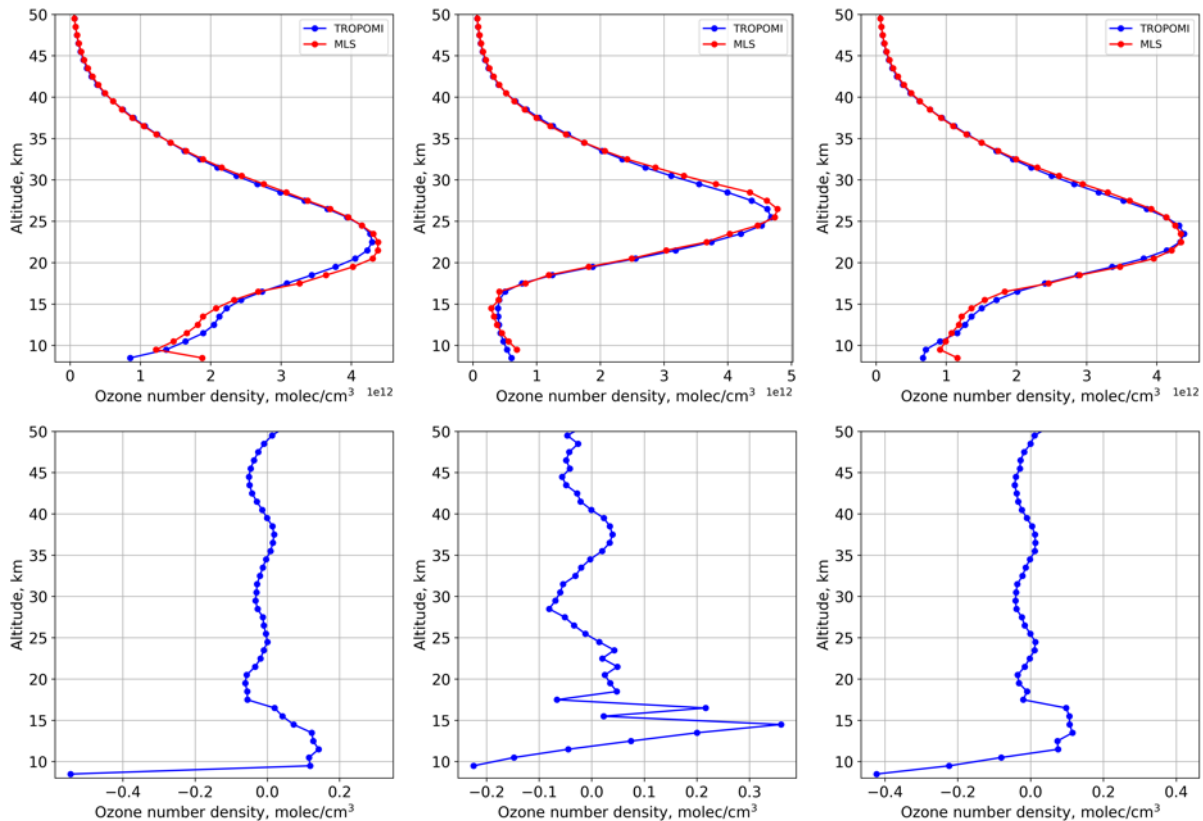


Figure 1: Comparison of the ozone profiles retrieved from MLS and TROPOMI. Top row: retrieved profiles from MLS (red) and TROPOMI (blue) averaged between July 2021 and December 2022 for different latitude ranges, from left to right: northern mid-latitudes (25N – 65N), tropics (15S – 15N), southern mid-latitudes (65S – 25S). Bottom row: relative differences between the profiles shown in the top row.

A comparison between the ozone profiles retrieved from TROPOMI and MLS measurements is shown in Figure . Both data sets were temporary and spatially gridded in the same way and then averaged to obtain zonal monthly mean values for three latitude ranges, northern mid-latitudes (25N – 65N), tropics (15S – 15N) and southern mid-latitudes (65S – 25S). For the northern mid-latitudes (left column of the plot), the relative differences between the mean profiles are well below 10% down to 14 km increasing then to about 15% below. It should be noted however that the quality of MLS data is known to degrade with decreasing altitude below 15 km. At the lowermost level, the difference reaches 40%, which is most probably caused by an unrealistic increase in the MLS profile seen at this altitude. For the tropics (middle column of the plot), the relative difference is below 10% down to 17 km and increases to 20 - 30% below. The latter increase is explained by an extremely low amount of ozone in the tropical troposphere. The agreement at southern mid-latitudes (right column of the plot) is similar to that observed at northern mid-latitudes with differences around 5% down to 17 km and increasing below.

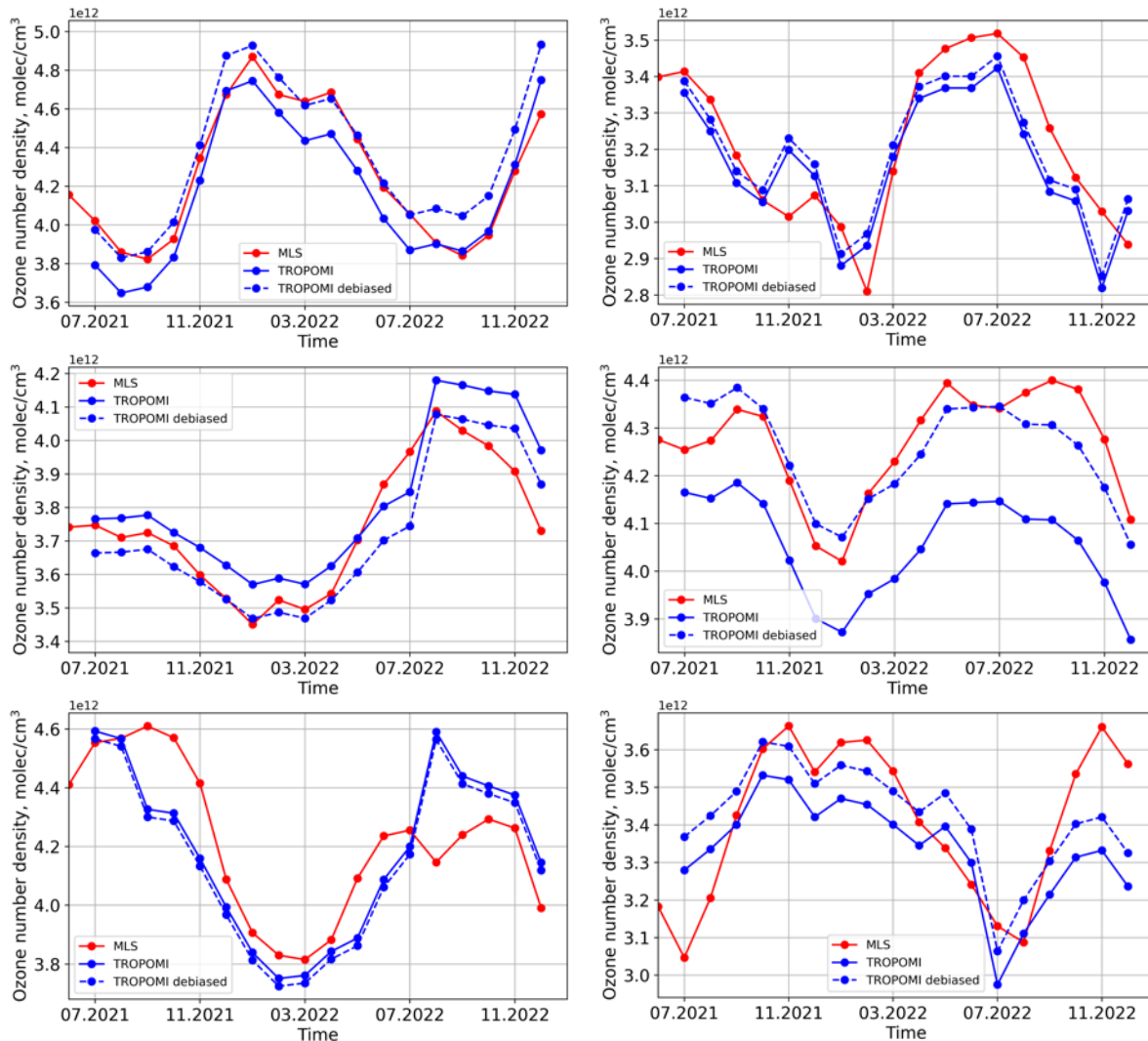


Figure 2: Comparison of partial column time series from MLS (red) and TROPOMI (blue). The dashed blue line shows debiased TROPOMI results (see text). Left column: partial columns between 20 – 25 km. Right column: partial columns between 25 – 30 km. Rows from top to bottom: northern mid-latitudes (25N – 65N), tropics (15S – 15N), southern mid-latitudes (65S – 25S).

Figure shows a comparison of partial ozone column time series from July 2021 to December 2022 retrieved from measurements of TROPOMI and MLS. The monthly zonal mean data for different latitude ranges are shown in different rows of the plot, from top to bottom: northern mid-latitudes (25N – 65N), tropics (15S – 15N), southern mid-latitudes (65S – 25S). The left column shows the partial columns from 20 to 25 km while the columns from 25 to 30 km are shown in the right column of the plot. The dashed blue line shows the debiased TROPOMI data, which are obtained as:

$$\text{TROPOMI}_{\text{debiased}} = \text{TROPOMI} - \text{mean}(\text{TROPOMI}) + \text{mean}(\text{MLS})$$

In general, a good agreement between the time series from the two instruments is observed. However, some remarkable features, which need further investigations can be identified. First, there are discrepancies near the end of time series in the northern and southern mid-latitudes as seen in the upper and lower right plots. Furthermore, a jump seems to be present in the 20 – 25 km time series in the tropics and southern mid-latitudes (middle and bottom left panels) and less pronounced at northern mid-latitudes (top left panel) between July and August 2022. This jump might be related to the change in the level 1 version of the TROPOMI data from 2.00

to 2.01 in late July 2022. Additional investigations are needed to check if the vicarious calibration developed using level 1 V2.00 data is still applicable to level 1 V2.01 data.

In conclusion, first comparison of the ozone vertical profiles retrieved from the operational TROPOMI data show a good agreement with MLS data on the level of 5-10% down to 14 – 17 km. The overall behaviour of the time series is similar although some features were identified which need an additional investigation.

Outlook

As a next step all available data need to be retrieved to check if the identified disagreement is eventually caused by a sparse temporal sampling of the used data. In parallel, it should be checked if a new vicarious calibration needs to be done to work with V2.01 of TROPOMI level 1 data. Furthermore, the measurements between the start of the TROPOMI mission in November 2017 and July 2021 need to be processed as soon as the corresponding level 1 data of version ≥ 2.00 become available.

Dissertation

1. N. Mettig, *Ozonprofilretrieval aus satellitengestützten Messungen von TROPOMI und CrIS im ultravioletten und infraroten Spektralbereich*, Universität Bremen, Bremen, 2022, <https://doi.org/10.26092/elib/1664>

Presentations

2. N. Mettig, Weber, M. Rozanov, A., J.P. Burrows, and Veeffkind, P., *TOPAS ozone profile retrieval from TROPOMI ultraviolet spectral range in combination with CrIS infrared spectral range*, ESA Living Planet Symposium, Bonn, May 23-27.

6.31 *nak0001*: Seamless sea ice prediction with AWI Climate Model

HLRN Project ID:	nak00001
Run time:	III/2021 – II/2022
Project Leader:	Dr. H. Goessling
Project Scientists:	M. Athanase, S. Losa, L. Mu, L. Nerger
Affiliation:	Alfred-Wegener-Institut Helmholtz Zentrum für Polar- und Meeresforschung, Bremerhaven

Overview

The Young Investigator Group “Seamless Sea-Ice Prediction” (SSIP) funded by BMBF aims at advancing sea-ice prediction capacity on timescales from hours to years and beyond. A core activity of the group is to develop a seamless sea ice prediction system based on a state-of-the-art climate model. The latter is combined with a sophisticated data assimilation (DA) system for the estimation of forecast initial conditions. The system also allows for new approaches to model error diagnosis and parameter optimization.

The seamless coupled sea-ice - ocean prediction system (SSIP and later AWI coupled prediction system, AWI-CPS) has been developed based on the AWI climate model (originally AWI-CM v1.1). The current version of the system is based on AWI-CM v3.0 (Streffing et al. 2022) that includes FESOM2.0 (Danilov et al., 2016) as a sea-ice ocean component and the Integrated Forecasting System (OpenIFS) developed at the European Centre for Medium-Range Weather Forecasts (ECMWF 2017a, b, c) as an atmospheric component. The sea ice concentration, sea ice thickness, sea ice drift, sea surface temperature, sea surface height, and temperature/salinity profiles are assimilated into the system with an Ensemble Kalman-type filter (EnKF) within the Parallel Data Assimilation Framework (PDAF; Nerger and Hiller, 2013). The HLRN project allowed to continue the successful development of the AWI-CPS, which required running extensive sets of sensitivity experiments and re-forecasts for testing, evaluation, and optimization.

A comprehensive evaluation of the developed SSIP and AWI-CPS2.0 systems has been summarized in the studies by Mu et al. (2020, 2022), which documented strong improvement of the predicted ocean and sea ice states by observational data assimilation. Our most recent developments were targeted at a further improvement of seasonal sea-ice prediction skills by complementing the EnKF-based data assimilation in the ocean/sea-ice component with relaxation (nudging) of the large-scale atmospheric dynamics towards atmospheric re-analysis data. In particular, following Sánchez-Benítez et al. (2022), we nudge spectrally the large-scale atmospheric circulation to ERA5 data to additionally constrain the otherwise chaotic atmosphere.

Results

Current results show benefits of constraining the atmosphere additionally to the assimilation of the sea ice and ocean observational data. In particular, nudging the atmosphere to observed/re-analysed large-scale circulation improved the simulated sea ice drift (SID). The ensemble-mean of the 24-hour sea ice drift forecast obtained by AWI-CPS with the atmospheric spectral nudging (Fig. 1 upper middle panel) reveals a spatial distribution similar to the observed SID distribution on 27 September 2018 (Fig.1, upper left panel) in contrast to the SID ensemble mean 24-hour forecast without nudging (Fig. 1, upper right panel). The system's skills in predicting SID components over the entire year 2018 are presented in the lower panels of Figure 1. Depicted are the correlations of the predicted SID components with

those observed. The correlation coefficient (r) is significant and exceeds 0.7 all over the Arctic Ocean (except for Baffin Bay and western part of the Fram Strait and Greenland Sea, where r is less than 0.4 locally). In the experiment without nudging the large-scale winds, the correlation between predicted and observed SID components is very low and hardly statistically significant (Fig. 1, lower right panel).

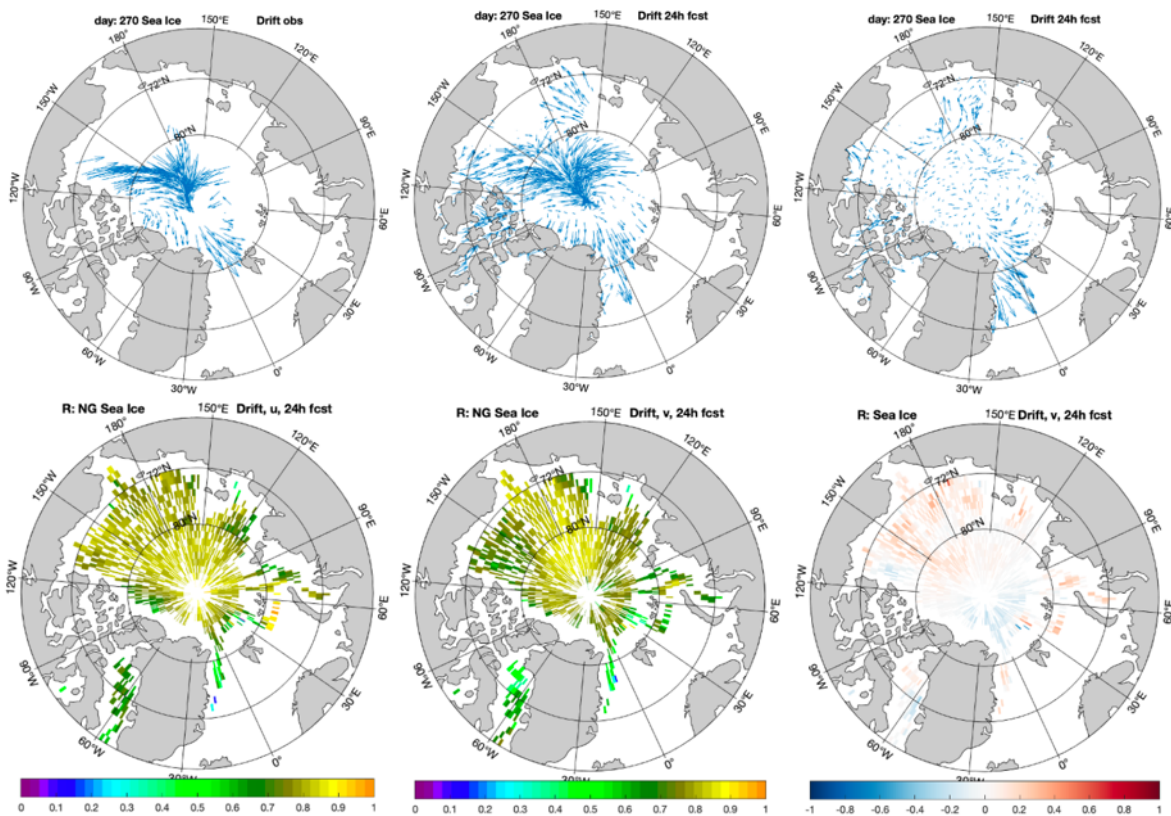


Figure 1: Top: Sea Ice Drift as observed (upper left) and predicted with and without nudging (upper middle and upper right, respectively) on one exemplary day. Bottom: Coefficients of correlation for u and v components of the sea-ice drift with wind nudging (lower left and middle) and for the v component without nudging (lower right).

This additional constraint of the ensemble-based coupled prediction system allows to reduce possible biases originating from the atmospheric states diverging because of the chaoticity of the atmospheric system. As a result, the DA analysis increments are also reduced as the sea ice and ocean forecast states obtained with the less biased system deviated from the observations to a lesser extent. For example, Figure 2 presents the mean absolute estimates of the DA increment for the sea ice concentration (SIC) and sea ice thickness (SIT) obtained with and without nudging the large-scale winds, averaged over the year 2018. The decreased divergence of the atmosphere state in case of atmospheric spectral nudging enables an improved AWI-CPS performance over longer than 24 hour forecast periods. The good prediction skill of the sea ice drift remains at least on synoptic scales when initialising the system with the state obtained after the filter analysis in the experiment with nudging and integrating further without any data assimilation and atmospheric constraint.

Outlook

We continue to carry out and evaluate experiments generally targeted at the improvement of seasonal sea-ice prediction skills (re-forecasts starting in different seasons, as in Mu et al., 2022).

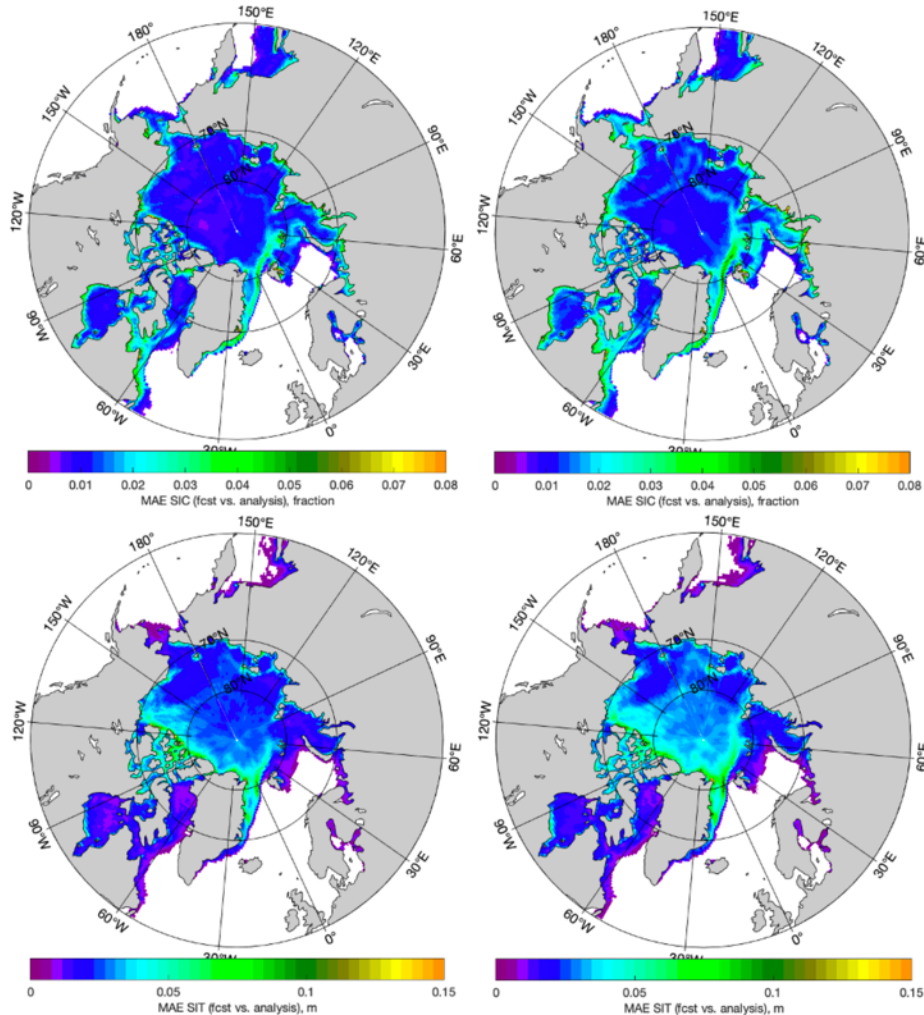


Figure 2: MAE of the DA increment obtained for sea ice concentration (SIC, upper) and sea ice thickness (SIT, bottom) the experiments with and without nudging (left and right, respectively).

Publications

1. L. Mu, L. Nerger, J. Streffing, Q. Tang, B. Niraula, L. Zampieri, S. N. Loza, H.F. Goessling, Sea-ice forecasts with an upgraded AWI Coupled Prediction System. *Journal of Advances in Modeling Earth Systems*, 14, e2022MS003176. <https://doi.org/10.1029/2022MS003176>

Presentations

2. M. Athanase et al., Progress on nudging approaches with the AWI-CM3 system for polar predictions". YOPP Final Summit, Montreal (QC), Canada, 29 August–1 September, 2022.

References

1. Danilov, Sergey, Dmitry Sidorenko, Qiang Wang, and Thomas Jung. "The finite-volume sea ice–ocean model (fesom2)." *Geoscientific Model Development* 10, no. 2 (2017): 765-789.
2. *ECMWF: IFS Documentation CY43R3 – Part III: Dynamics and numerical procedures, no. 3 in IFS Documentation, ECMWF, <https://doi.org/10.21957/8l7miod5m>, 2017a*
3. *ECMWF: IFS Documentation CY43R3 – Part IV: Physical processes, no. 4 in IFS Documentation, ECMWF, <https://doi.org/10.21957/efyk72kl>, 2017b*
4. *ECMWF: IFS Documentation CY43R3 – Part VII: ECMWF wave model, no. 7 in IFS Documentation, ECMWF, <https://doi.org/10.21957/mxz9z1gb>, 2017c*
5. L. Mu, L. Nerger, Q. Tang, S.N. Losa, D. Sidorenko, Q. Wang, T. Semmler, L. Zampieri, M. Losch, H. F. Goessling, Towards a data assimilation system for seamless sea ice prediction based on the AWI Climate Model. *Journal of Advances in Modeling Earth Systems*, p.e 2019MS001937, <https://doi.org/10.1029/2019MS001937>
6. L. Nerger and W. Hiller, 2013. Software for ensemble-based data assimilation systems – Implementation strategies and scalability. *Computers & Geosciences*, 55, pp.110-118.
7. Sánchez-Benítez, A., Goessling, H., Pithan, F., Semmler, T. and Jung, T. (2022): The July 2019 European Heat Wave in a Warmer Climate: Storyline Scenarios with a Coupled Model Using Spectral Nudging, *Journal of Climate*, 35 (8), pp. 2373-2390. doi: 10.1175/JCLI-D-21-0573.1
8. Streffing, J., Sidorenko, D., Semmler, T., Zampieri, L., Scholz, P., Andrés-Martínez, M., Koldunov, N., Rackow, T., Kjellsson, J., Goessling, H., Athanase, M., Wang, Q., Sein, D., Mu, L., Fladrich, U., Barbi, D., Gierz, P., Danilov, S., Juricke, S., Lohmann, G. and Jung, T. (2022) AWI-CM3 coupled climate model: Description and evaluation experiments for a prototype post-CMIP6 model, *EGUsphere*, 2022, 1–37, doi: 10.5194/egusphere-2022-32